Positioning in Geophysics: Applications to GPS Seismology, Airborne Gravimetry, and the Dawn Spacecraft at Vesta

by

Frank Joseph Centinello III
M.S., Aerospace Engineering, University at Buffalo (2007)

Submitted to the Department of Earth, Atmospheric and Planetary Sciences
in partial fulfillment of the requirements for the degree of
Doctor of Philosophy
in Geophysics
at the
MASSACHUSETTS INSTITUTE OF TECHNOLOGY
February 2015

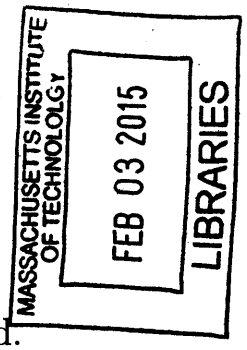

Author ..... Signature redacted .....
Department of Earth, Atmospheric and Planetary Sciences
December 20, 2014

Certified by ..... Signature redacted .....
Thomas Herring
Professor of Geophysics
Massachusetts Institute of Technology
Thesis Supervisor

Certified by ..... Signature redacted
Maria T. Zuber
E.A. Griswold Professor of Geophysics
Massachusetts Institute of Technology
Thesis Supervisor

Accepted by ..... Signature redacted .....
Robert van der Hilst
Schlumberger Professor of Earth and Planetary Sciences
Head, Department of Earth, Atmospheric and Planetary Sciences

Positioning in Geophysics: Applications to GPS Seismology, Airborne Gravimetry, and the Dawn Spacecraft at Vesta

by

Frank J. Centinello III

Submitted to the Department of Earth, Atmospheric and Planetary Sciences
on December 20, 2014, in partial fulfillment of the
requirements for the degree of
Doctor of Philosophy
in Geophysics

Abstract

This dissertation presents improvements made on position estimation techniques applied to seismology, airborne gravimetry and planetary gravity recovery. In Chapters 2 and 3, a smoothed ionospheric model computed using GPS phase observations was applied to seismology and airborne gravimetry. The seismic investigation observed the 2010 El Mayor-Cucapah earthquake near Baja, California. The application of the ionospheric model resulted in an overall 4 mm RMS reduction in the measurements of GPS heights. The same ionospheric technique was applied to GPS data collected during an airborne gravity survey. In this study the model improved the RMS spread of four repeat gravity profiles by 0.6 mGal.

Chapters 4 and 5 focus on the Dawn mission to the asteroid 4 Vesta. Chapter 4 details the use of spacecraft image constraints in the orbit determination software GEODYN, which is used by NASA/GSFC for trajectory reconstruction and geophysical analyses of planets. Image constraints are shown to converge an orbit solution that differs from that computed by the Dawn Science Team at JPL by less than 13 m. Chapter 5 describes the application of the new technique in the estimation of the orientation parameters and low-degree gravity field of Vesta. The pole orientation and low-degree gravity field estimated agree with that presented by the Dawn Science Team through the use of an independent software and estimation algorithm.

Thesis Supervisor: Thomas Herring
Title: Professor of Geophysics
Massachusetts Institute of Technology

Thesis Supervisor: Maria T. Zuber
Title: E.A. Griswold Professor of Geophysics
Massachusetts Institute of Technology

Dedication

This work is dedicated to all of the fierce explorers who I know about and those who I have yet to learn about, who have been my inspiration as long as I can remember.

To Mom and Dad

You inspired me, let me get lost, and kept pushing me to find my way.

and to Phil

I love you like the day is long, on Mercury.

(the Mercurian rotational period lasts 1407.5 hrs)

Acknowledgments

I would like to thank my advisors, Professors Tom Herring and Maria Zuber, for the opportunity they've provided me. I thought I knew a lot about GPS when I arrived here, but navigation and simulation are much different fields from geophysics and geodesy, and using real data. Through much patience, Tom has taught me some of the nuance it takes to do science with GPS measurements, and in the process has opened my eyes to the many possible scientific uses of the technology. He also taught me a great many tools with which to scrutinize data, which I know I will put to work in the future. Maria taught me planetary science, and how to do geophysics off-world (first, find yourself a rocket...). I have benefitted greatly from her support, knowledge and patience while I struggled with learning an entirely new field, and software set. In addition, she introduced me to so many people who have generously shared their knowledge in helping me with the work presented here. Both Maria and Tom have supported my development inside and out of academia. They encouraged me to visit Greenland to get hands-on experience observing the ionosphere (for which I left the day *after* my general exam), and supported my endeavors to complement my academic work with flight training and science outreach for the general public.

This dissertation committee has also provided a great deal of support. My defense will be the fourth time we've met to discuss my work. They've put a great deal of time into my research, and for that I'm extremely grateful. Professor Alison Malcom introduced me to the field of seismology. Professor Kerri Cahoy has provided a great deal of professional and scientific advisement, and was very helpful in putting me in touch with others in the field of space physics. Starting in 2009, Dr. Erwan Mazarico taught me how to do orbit determination. Now we've estimated the gravity field of an asteroid together.

I would like to thank Profs. Brad Hagar and Taylor Perron for being on my generals committee and teaching me geodynamics and geomorphology. Prof. Kang Hyeun Ji helped me get my footing when I landed at MIT. I hope to be friends with Drs. Noah Bechor, Bob King, Mike Floyd, and Sarah Stamps for a long time to come.

Dr. Despina Pavlis and Dr. Jack McCarthy, and Dr. Jesse Wimert are on the GEODYN development staff and first taught me how to use the software, and were always there for me when I went into the weeds. Dr. David Smith, Dr. Frank Lemoine, Dr. Greg Neumann and Dr. David Rowlands provided conversational and technical guidance in implementing the new image capability in GEODYN throughout my time working on orbit determination. Dr. Jason Sonderblom, Dr. Katarina Milijkovic, and Dr. Brandon Johnson have provided valuable insight into the work presented here.

The Dawn Science Team, and JPL navigation team have also provided a great deal of assistance and conversation helpful to enabling the image capability in GEODYN and conducting the geophysical investigation of the body. I would like to thank Prof. Chris Russell and Dr. Carol Raymond for the privilege of working on a mission to the asteroid belt. I would also like to thank Drs. Sami Asmar, Alex Konopliv, Ryan Park, and Robert Gaskell, who provided me with radiometric and image data and valuable information about the Dawn spacecraft operations, and insight into orbit determination and gravity estimation.

I would like to thank Dr. Vicki Childers, Dr. Theresa Damiani, Sandra Preaux and Carly Weil at the NOAA/NGS for providing GPS and airborne gravimeter data, as well as access to NOAA/NGS software and technical reports. They introduced me to airborne gravimetry, and provided extremely helpful conversation and support with this work.

Roberta Allard, Margaret Lankow, Brenda Carbone, and Kerin Willis have been rooting for me from the start. I will miss the support, conversation & laughs. This crew is the science underground in EAPS without which none of the work in this thesis would have come together, because I would probably be stuck on a layover someplace. They also reminded me to eat well and shave, my mother will be happy to know.

I am grateful to El Patrón Prof. Mark Robinson, El Jeffe Ernest Bowman-Cisneros, Capo di Capi Kristen Paris, Joe "the Skipper" Barnett, and the Most Evil Nick Estes and Ken Bowley on the LROC team for the privilege working on

LROC, teaching me ISIS software, and helping me to study the use of image data from LRO to help the orbit determination on that mission. And for helping to unlock my accounts every four weeks, and answering questions about the Moon and life. *Live long, and prosper.*

I would like to thank three-time Oscar winner, four-time nominee Dame Yodit Tewelde for her care package of toy planes, and Time Keeper/Diehard Buffalo Bills Fan, loyal subject of the British Empire, Ruel Jerry for counting down the days to my defense, without which I am sure I would have showed up on the wrong day. I mark the passage of time with the Mayan Calendar and I have not known the date for what must be quite some time now. Black Belt Alejandra Quintanilla is my body guard. *Citoyen* Jean-Arthur Olive taught me how to pick out a tweed blazer. Commodore Matthieu Talpe is a very supportive friend, and I am not sure where Helmsman Zhenliang Tian is at the moment. He was *just* here. I hope to one day share an office again with Lead Obo, Aaron Scheinberg, but that we need a team of sled dogs to get to that office, and that there is a radar dish nearby. Lead Bass Gabi Melo makes a mean pea soup and pairs it ingeniously with !!METAL!!. Also a METAL HEAD, Dive Master Ben Corbin has provided a place to crash in the last months of this effort, because he is exploring Italy at the moment. He and Nate Dixon, ESQ., are *Patriots* fans. ...

The Master Brewer for this work was Mike Andrle, who made the official beer, dubbed "JP8" after the jet fuel. It has a subtle nutty aftertaste, and an improved burn temperature which is useful in pinch situations with three or more bogeys. He also helped me proof some of these chapters. This work will be translated, in its entirety, into *Breizh* by Anne-Fleur Stephane. Conflicts between the chapters were mediated by Elizabeth Wright, who reached an agreement with Chapters 7-15, which will be part of an independent volume with full autonomy. Chief of Ergonomics, Will Lubelski donated a pair of awesome flat screen monitors. *Chef Pâtissier* Daria Van Tyne, who is awaiting trial in The Hague for her devastatingly good tiramisu, and the Honorable Mike Gunnuscio are dear friends, and were extremely supportive through my time here.

The "Tiger Team" has been a tradition since the founding of NASA. It is "a team of undomesticated and uninhibited technical specialists, selected for their experience, energy, and imagination, and assigned to track down relentlessly every possible source of failure in a spacecraft subsystem" (see Dempsey [1]). The members of the Tiger Team for this dissertation are Ben Mandler *Sensei*, Brig. Gen. Roger Fu, USA Ret., His Holiness the 16th Anton Ermakov, Alex Evans, Chief Medical Officer, U.S.S. *Enterprise*, the Rev. Michael Sori, and shortstop, No. 24, Jared Atkinson, all of whom helped me troubleshoot a mission-critical anomaly in the assembly and testing phase, mere weeks before the launch of this work.

I also have a dream-team of encouragement in my corner. My personal trainer is my uncle Lou. He, Preston Wells and Dr. Moriba Jah, stepped in often to remind me of the big picture. Sometimes, walking up a steep staircase 20 times will give you all the new perspective you need.

My Mom and Dad have relentlessly supported my endeavors no matter where they've taken me, and against the judgement of many, many others. They are why I went to grade school at a zoo and learned to fly. But what I love most are Sunday dinners and watching the Bills. I love you always.

In the toughest times of this work, Phil Zegelbone has been a most loving and reliable companion. He made sure that there were pancake Saturdays and trips to the small towns around New England, which were at one time the launching points for many nautical vessels trading around our world. We will have many far-flung explorations, babe.

Contents

List of Figures

List of Tables

Chapter 1

Introduction

Geophysical investigations yield science results that our equipment and processing capabilities allow. Sometimes measurement noise limits the degree to which we can observe a given phenomenon. In other scenarios, a derived data type can enable an entirely new capability. We have a great many tools available to us as geophysicists, and making optimal use of them will maximize our science results. The theme of this dissertation can be thought of as offering improvements and new capabilities in geophysics, which can result in greater scientific capability. The techniques presented here have a strong focus on seismology and gravity science, but, when applied, they can benefit a wide range of other fields.

In the work presented on the following pages, the "positions" of various measurement devices are precisely calculated. In Chapter 2, we study the positions of ground-based GPS receivers. In Chapter 3, we reconstruct the position of an aircraft. In Chapters 4 and 5, the position of a spacecraft across the solar system is computed. But this thesis is about much more than knowing the precise location of GPS stations, aircraft or spacecraft. The techniques studied here have the potential to improve results obtained from seismology, airborne gravimetry, and planetary radio science. Knowing "where things are" has always been important in science. We *have* to know where measurements were made and where samples were collected. In the most extreme sense, sometimes the calculated position itself is the sought-after piece of information which enables us to study a phenomenon, such as a planetary gravity

field.

This thesis first addresses the effect of ionospheric delays on GPS positioning. A smoothed ionospheric model is applied to GPS measurements in two applications detailed in Chapters 2 and 3. Chapter 2 applies the technique to ground-based, high-rate GPS receivers. The data studied span the interval of the 2010 El Mayor-Cucapah earthquake near Baja California. High rate receivers have been increasingly used in recent years, and any positioning improvements that can be made will benefit science as GPS equipment becomes more prevalent. In Chapter 3, the ionospheric model is applied to compute the trajectory of an aircraft used for airborne gravimetry. In the scenarios in Chapters 2 and 3, the network of GPS receivers is spread out over hundreds of kilometers, which means each receiver possibly senses much different portions of the ionosphere, which further illustrates the need for the application of an accurate ionospheric model in computing the positions of GPS receivers.

The GPS constellation was designed to operate on more than two frequencies for the purpose of combining the phase observables on different frequencies to compute and subract the first-order ionospheric effects on the positionining calculation (see Leick, [2]). Modeling the ionosphere in this way, however, introduces the noise of the GPS observables in a root sum of squares (RSS) sense, and can increase the ultimate RMS of the noise of the position solution by a factor of 3 (see Herring et al., [3]). In this work, the ionospheric contribution to the phase observables is computed using a combination of the L1 and L2 observations, but I attempt filter the noise contributed by the phase observables. This technique, when applied correctly, leaves only the contribution of and dynamics of the actual ionosphere to the phase observables.

The vertical component of positions calculated from GPS observables has in previous work carried a a larger noise root mean square (RMS) than the horizontal components (see Bilich, et al., [4] and Bock, et al., [5]). This is due in part to delays and noise caused by the atmosphere and ionosphere (see Wanniger [6], and Langley, [7]). One major result of applying an ionospheric model with reduced noise RMS was the improved observation of GPS vertical positions, for both the seismology and airborne gravimetry investigation. For the seismology work, the application of the

ionospheric model was shown to improve position RMS magnitude by 2 mm horizontally and 4 mm vertically. Application of the model in the gravimetry investigation adjusted GPS heights by up to 20 cm, and resulted in an improved repeatability of observed gravity profiles by 0.6 mGal in an RMS sense.

The increased vertical noise component means it is more difficult to detect wave forms which manifest in the vertical direction. These include the initial pressure wave arrivals, as well as the surface waves which express in the vertical component such as the Rayleigh waveforms (see Geng et al., [8]). The application of the ionospheric model enhanced the observation of of surface dynamics and Rayleigh waves, well past the major earthquake dynamics. It did not allow observation of the P-wave arrivals since their amplitude is at least an order of magnitude smaller than the Rayleigh wave arrivals. This work shows that more work in improving ionospheric and atmospheric modeling could further enhance vertical resolution.

In the case of airborne gravimetry, vertical positioning is most important because the gravity gradient is strongest in the vertical direction (see Baumann et al., [9]). Noise reduction in position knowledge in this component is one of the most important improvements to be made in this field, since a 1 m position improvement can result in 0.3 mGal change in gravity, with the standard free-air correction. This means that improvements of 0.6 mGal shown in this work can effect the computed geoid on the order of $\sim 1 - 2$ meters.

In Chapter 4, image data are applied in the calculation of the orbit of the Dawn spacecraft at the protoplanet 4 Vesta. This work represents the first time images were included as a constraint using GEODYN software, which is the orbit determination and geophysical parameter estimation software of NASA Goddard Spaceflight Center (GSFC) (see Pavlis, et al., [10]). In this work, our eventual aim is to improve the spacecraft positioning for the purpose of inverting the orbit trajectory to compute the planetary orientation, spin rate, and gravity field. This effort is presented in Chapter 5. From the orientation and gravity field we can begin to infer the internal structure, chemical composition and formation history of Vesta.

The technique of using images for orbit determination has been applied by others

(see Owen et al., [11]), but this is the first instance with GEODYN software. There are several advantages to complementing traditional radiometric range and Doppler measurements with other orbit constraints. First, constraints from images taken by the spacecraft will likely cover time periods when radiometric tracking of the spacecraft from Earth is impossible due to geometry or scheduling constraints. In addition, image constraints can reduce orbit uncertainty in the along- and cross-track orbit components, which have typically carried higher position uncertainty (see Mazarico, et al., [12]). The use of the image constraints substantially aids in the gravity recovery effort at Vesta as they aid in the estimation and stabilization of the spin axis orientation, as well as GM and J_2.

Chapter 4 describes the calculation of image constraints using the pixel locations of landmarks observed in images in the estimation of the shape of Vesta by Gaskell et al., [13], and shows the improvement in agreement of the GEODYN orbit reconstruction with that of the Dawn Science Team of the NASA Jet Propulsion Laboratory. Chapter 5 describes the calculation of the Vesta spin axis orientation and gravity field using radiometric and image data. Performance is quantified partly through agreement with the results of the Dawn Science Team (see Konopliv et al., [14]). This work represents an important opportunity to both study Vesta as well as independently validate the software and methodology of the Dawn Science Team and NASA GSFC. GEODYN makes use of a Cowell integrator and batch least squares algorithm (see Cowell [15], and Pavlis et al., [10]), while JPLs analysis was completed using the MIRAGE orbit determination software, which is a Kalman filter (see [16]). Agreement between the two softwares in orbit reconstruction and gravity recovery validates the effort presented here as well as that of the Dawn Science Team.

Chapters 3, 4 and 5 have the goal of enhancing the capability of modeling local and planetary gravity fields. Gravity has been a source of curiosity, intrigue, and scientific investigation for much of human history. It holds us to our home world, the Moon in its orbit, and has inspired us to ask questions about its fundamental nature, the planet we live on, and the formation of our solar system. The attraction of gravity is caused by the mass within the worlds we study. Studying it provides insight into

the processes that create them and are active within them. Analysis of the gravity fields of planets provides a method of observing phenomena from the deep interiors of differentiated planetessimals to the movement of water on the surface of Earth.

This thesis presents the analysis of improvements to modern techniques of conducting gravity science and geodesy. It covers two investigations: one which examines possible improvements in computing regional gravity fields on Earth, and another seeking to answer questions about the formation of entire planets. Near-surface gravimetry on Earth has been a very useful tool that has provided us with the ability to study the forces which shape the landscape we live on. Its applications include the study of seasonal variations of Earth's water cycle, the investigation of the crust for natural resources, and mapping flood plains. Modeling planetary-scale gravity fields can tell us about the nature of the core, mantle and crust of a planetary body, and its general formation history. Investigations of planetary gravity fields have allowed us to observe the fluid motions of Earth's core [17] as well as detect large dikes beneath the lunar lithosphere [18].

Of practical motivation, the establishment of an accurate gravity model allows precise definition of a reference frame to the region or planetary body being studied. The definition of a vertical datum on Earth is tightly linked to the establishment of the local gravity field. On planetary bodies, the accurate knowledge of the position of the rotation axes, and its movements allow the establishment of a reference frame. Terrestrial and planetary reference frames, in addition to being used for navigation, are used to register datasets to the surface of the body. In this way, gravity science can assist other scientific investigations which, while not directly dependent on gravity, are dependent on accurate knowledge of reference frames to which subsequent datasets are registered.

The work presented in this dissertation starts with the accurate computations of the positions of GPS receivers, aircraft, and spacecraft. The benefits of the techniques presented here can reach far past simply knowing where things are. They can enhance knowledge gained from seismology, airborne gravimetry, and planetary gravity modeling. In addition, establishing accurate position measurements allows the definition

of a frame of reference with which other data sets (that may have nothing to do with gravity) can be registered. In that sense, this dissertation presents techniques which, when applied, can open scientific capabilities to us where they were not previously available.

Chapter 2

High-Rate GPS Observations of the 2010 El Mayor-Cucapah Earthquake Utilizing a Smoothed Ionospheric Model

2.1 Abstract

To mitigate ionospheric induced noise in GPS phase observables, a new processing technique is applied to improve the fidelity of GPS observations for scientific applications. To assess the capability of this technique, an ionospheric model was applied to ground-based 5-Hz GPS phase measurements from 36 stations during the 2010 El Mayor-Cucapah earthquake in Baja, California and GPS data were processed in a double difference method. In double differencing it is typical to compute the ionosphere's impact on GPS measurements using a linear combination of the phase data. Because this is a linear combination of the phase data, however, it carries with it a $\sim 3\times$ magnification of the phase noise. To reduce the induced noise, I apply a Kalman filter and smoother to the ionospheric delay computed using the phase data, resulting in a 4 mm reduction in the height position moving RMS in the receiver position time

histories. The east and north RMS components are subsequently improved by 1.9 mm and 2.3 mm, respectively, enabling enhanced observation of the surface arrival dynamics, and the coda after the main set of arrivals. As GPS networks become more prevalent, this technique has future applications in GPS-based geophysical investigations due to the ease of installation and decreasing cost of receivers. In addition, as we depart from the maximum activity period of the current solar cycle, any improvements in modeling and removing the ionospheric effects on GPS signals will further enhance the subsequent science results as the noise contributions from the GPS phase observables will be easier to isolate without filtering real ionospheric signal.

2.2 Introduction

The increasing prevalence of GPS stations used for geodesy and seismology (e.g. [19], [20]) is due to the low cost of GPS receivers and simpler installation requirements when compared with seismometers. As a result of this, improvements to GPS processing techniques have the potential to improve a vast array of GPS-based scientific capabilities.

The observability of earthquake dynamics decreases considerably with distance from the source, and with time after the initial event. Thus, the error sources of the instrumentation are a limiting factor in seismology. Error sources in GPS observations are receiver and satellite clock biases, multipath reflection, cycle slips, and atmospheric and ionospheric delays [21]. There are several processing methods used to mitigate the effects of the aforementioned error sources such as precise point positioning and double differencing [22]. However, errors arising from ionosphere-induced noise remain an impediment for improved quality and improved scientific analysis.

Global ionospheric maps computed from phase observations are provided daily by the International GPS Service (IGS) (see, e.g., Schaer et al., [23], and Hernández-Pajares, et al., [24]). With a spatial resolution of 2.5 degrees longitude every two hours, the maps are thin-sheet models of the ionosphere with vertically tallied total electron content (TEC) values at 450-km altitude. While the maps are useful to

provide a general constraint on the effects of the ionosphere, the maps do not provide spatial and temporal high-resolution variation (<1 km, and <1 minute, respectively) needed to accurately estimate centimeter-level GPS errors for high-rate data.

While previous workers have attempted to model ionospheric effects on GPS observations, these estimates are based on global models and poorly account for high frequency variations [25], [26]. For example, [25] apply GPS encoded model parameters derived from space weather observations [27] and although their model contains parameters for temporal, diurnal and geographic variations, they are unable to capture high frequency variations in the ionosphere and have errors of up to 50% of the actual ionospheric delay. While Spencer et al [26], apply a Kalman filter to estimate a thin-screen TEC map at 350-km altitude using double-differenced phase observations yielding improved phase residuals to 0.1 L1 wavelengths (19.0 cm) for up to 500-km baselines, their work does less applicable for highly localized regions or areas of high frequency variations.

In this work, I present a technique for mitigating GPS phase induced in the position calculation through traditional use of the phase observables to remove ionospheric delays. Contrary to previous workers, I apply a Kalman filter and smoother to remove the phase noise from the delay calculation of the individual observables, as opposed to creating a global-scale model.

2.3 Methodology

Track is a kinematic GPS software that is developed and maintained at MIT. It computes GPS receiver time histories using double-differences of phase observables to cancel the effects of the receiver and satellite clocks, mitigate the effects of the atmosphere and ionosphere, and estimate phase ambiguities (see, e.g., Herring et al., [28], and Dong and Bock, [29]). In its operation, Track uses GPS pseudorange data to compute coarse position time histories for the receiver network, and subsequently refines the computed positions using the double-differenced L1 and L2 phase measurements. For the double differencing calculations, effects of the satellite and receiver

clock biases are cancelled by differencing simultaneous observations from two GPS spacecraft by two GPS receivers. This technique mitigates the effect of atmospheric and ionospheric delays when the GPS receivers are in close proximity (< 3 km). This is true because nearby receivers likely observe signals to the same satellite through similar neutral atmospheric and ionospheric conditions. As the receivers are moved farther apart, different regions of the atmosphere and ionosphere affect the respective GPS signals. Therefore, with increasing baseline length, the assumption that ionospheric effects largely cancel begins to break down.

The equation for a GPS phase observable on the L1 and L2 carrier frequencies for receiver k and spaceraft p, in units of cycles is (see Leick [22]):

$$\begin{aligned}\phi^p_{k,1}(t_k) &= \tfrac{f_1}{c}\rho^p_{k,1}(t^p) + N^p_{k,1}(1) - f_1\Delta t_k + f_1\Delta t^p + \tfrac{f_1}{c}I^p_{k,1,\phi}(t_k) + \tfrac{f_1}{c}T^p_{k,1}(t_k) + \delta^p_{k,1,\phi} + \varepsilon_{1,\nu}\\ \phi^p_{k,2}(t_k) &= \tfrac{f_2}{c}\rho^p_{k,2}(t^p) + N^p_{k,2}(2) - f_2\Delta t_k + f_2\Delta t^p + \tfrac{f_2}{c}I^p_{k,2,\phi}(t_k) + \tfrac{f_2}{c}T^p_{k,2}(t_k) + \delta^p_{k,2,\phi} + \varepsilon_{2,\nu}\end{aligned} \tag{2.1}$$

where the parameters are defined in Table 2.1.

Parameter	Description
c	Speed of light.
f_1	L1 carrier frequency, 1575.42 MHz.
f_2	L2 carrier frequency, 1227.60 MHz.
t^p	Time of signal transmission from spacecraft.
t_k	Time of signal reception at receiver.
$\rho^p_k(t_p)$	Geometric vacuum distance between the receiver and spacecraft, computed in inertial cartesian coordinates.
$N^p_k(1)$ and $N^p_k(2)$	Phase ambiguities on the L1 and L2 signals, cycles.
Δt_k	Receiver clock bias, in seconds.
Δt^p	Satellite clock bias, in seconds.
$I^p_{k,1,\phi}(t_k)$	Ionospheric delay on the L1 signal, in meters.
$I^p_{k,2,\phi}(t_k)$	Ionospheric delay on the L2 signal, in meters.
$T^p_k(t_k)$	Tropospheric delay on the L1 and L2 signals, in meters.
$\delta^p_{k,1,\phi}$	Hardware delays and multipath effects on the L1 signal, in cycles.
$\delta^p_{k,2,\phi}$	Hardware delays and multipath effects on the L2 signal, in cycles.
$\varepsilon_{1,\nu}$	L1 phase noise, in cycles.
$\varepsilon_{2,\nu}$	L2 phase noise, in cycles.

Table 2.1: Parameters in the GPS phase observable expression in Eqn. 2.1.

The observables in Equation 2.1 can be calculated in units of distance by multi-

plying by the respective L1 and L2 wavelengths, 19.0 and 24.4 cm. The ionospheric group delays in Eqn. 2.1 can be computed in units of distance as:

$$I(f) = \frac{40.3}{f^2}\text{TEC} \tag{2.2}$$

where f here is either the L1 or L2 frequency, and TEC is the "total electron content" affecting the signal from satellite to the receiver. This expression approximates the first order effects of the ionosphere, and for the phase delay, will have the opposite sign (see Jackson [30]). The TEC is the integration of the electron density, N_e, along the transmitted signal, s:

$$\text{TEC} = \int N_e ds \tag{2.3}$$

The TEC is expressed in TEC units, or TECU, and 1 TECU=10^{16} e^-/m^2. Equation 2.1 describes the phase observation by one receiver from one spacecraft. If we difference the L1 phase observation with receiver, k, and another L1 phase observation from receiver m, as:

$$\phi^p_{km,1}(t_k) = \phi^p_{k,1}(t_k) - \phi^p_{m,1}(t_m) \tag{2.4}$$

we obtain the following single-difference expression:

$$\phi^p_{km}(t) = \frac{f_1}{c}\rho^p_{km}(t^p) + N^p_{km}(1) - f_1(\Delta t_k - \Delta t_m) + I^p_{km,1,\phi}(t_k) + \frac{f_1}{c}T^p_{km}(t_k) + \delta^p_{km,1,\phi} + \varepsilon_{km,1,\nu} \tag{2.5}$$

In this expression of the receiver-to-receiver single difference, the satellite clock bias term, Δt^p, is not present because it cancelled in the difference. Also, the time of reception terms, t_k, and t_m, are equal to within several nanoseconds, and we use t. The terms with km subscripts, denote the difference between those effects on the respective signals at receiver k and receiver m. For example, the difference in the ionospheric delay is given by:

$$I^p_{km,1,\phi}(t_k) = I^p_{k,1,\phi}(t_k) - I^p_{m,1,\phi}(t_m) \tag{2.6}$$

If the two receivers are close in proximity, one could image that signals they receive

from the same satellite travel through the same portion of the ionosphere, in essence making $I^p_{k,1,\phi}(t_k) \approx I^p_{m,1,\phi}(t_m)$, which would cause the differenced ionosphere term to 0. This would also be true for the tropospheric delay. The next step in differential processing is to form a double difference, in which two single-differenced observations from different spacecraft, say satellite p and satellite q is computed:

$$\phi^{pq}_{km}(t) = \phi^p_{km}(t) - \phi^q_{km}(t) \tag{2.7}$$

Here, the pq supersript denotes the difference between the single differences. If we expand Eqn. 2.7, we have:

$$\phi^{pq}_{km}(t) = \frac{f_1}{c}\rho^{pq}_{km}(t) + N^{pq}_{km}(1) + I^{pq}_{km,1,\phi}(t_k) + \frac{f_1}{c}T^{pq}(t_k) + \delta^{pq}_{km,1,\phi} + \varepsilon^{pq}_{km,1,\nu} \tag{2.8}$$

In this expression, there is no receiver clock bias term, $f_1(\Delta t_k - \Delta t_m)$, because it cancelled in the double difference. For short baselines between the receivers the same negation occurs with the ionosphere and troposphere, since the receivers will observe the second spacecraft through the same portion of the ionosphere. The focus of this work deals with what happens when this is not true, and $I^p_{km,1,\phi}(t_k) \neq 0$, $I^q_{km,1,\phi}(t_k) \neq 0$, and $I^{pq}_{km,1,\phi}(t_k) \neq 0$. It is for this reason that GPS was designed with two transmission frequencies. In such cases, when there are large baseline distances between receivers, it becomes necessary to compute an ionosphere-free combination of the phase observables given by Dong and Bock, [29], and Bock [31]:

$$\Phi_{LC} = 2.546\Phi_{L1} - 1.546\Phi_{L2} \tag{2.9}$$

In Eqn. 2.9, the phase observables are represented in units of distance as:

$$\Phi_{L1} = \frac{c}{f_1}\phi_{L1} \tag{2.10}$$

and

$$\Phi_{L2} = \frac{c}{f_2}\phi_{L2} \tag{2.11}$$

where the symbology was simplified by representing $\phi^p_{k,1}(t_k)$ as ϕ_{L1} and $\phi^p_{k,2}(t_k)$ as ϕ_{L2}. The coefficients in this expression result from forming a linear combination of the phase observations on the L1 and L2 frequencies and are: $\frac{f_1^2}{f_1^2-f_2^2} = 2.546$ and $\frac{f_2^2}{f_1^2-f_2^2} = 1.546$ (see Leick [22]).

While equation 2.9 can be used to compute positions, it can magnify the noise of the phase observables by up to 3 times. If we consider the standard deviation of the noise of the phase residuals is approximately 1% of their respective wavelengths, then the L1 noise standard deviation is 2 mm, and the L2 noise standard deviation is 3 mm (which is dependent on the algorithm the receiver uses to aquire the L2 phase, and vary with different receiver brands). In Equation 2.9, we have $\sqrt{(2.546 \times 2 \text{ mm})^2 + (1.546 \times 3 \text{ mm})^2} \approx 7$ mm. This increase in the noise is enough to degrade the positioning solution by 10s of centimeters.

In the work presented here, I perform the double differencing calculation without using Eqn. 2.9, and apply an ionospheric model to Eqn. 2.1. Through the ionospheric model, the objective is to calculate the ionospheric contribution to the phase observables, and smooth its associated phase noise. We start with the L1 and L2 phase residuals, converted to meters, $d\Phi_1$ and $d\Phi_2$. The difference between the converted phase residuals *is* the contribution of the ionosphere, in meters, on the L1 and L2 signals:

$$\Delta\Phi_{12} = \frac{40.3 \times \text{TEC}}{f_1^2} - \frac{40.3 \times \text{TEC}}{f_2^2} \tag{2.12}$$

where the difference in Eqn. 2.12, carries the factor ~ 3 augmentation of the noise discussed earlier since it is a linear combination of the phase residuals. Eqn. 2.12 is our starting point in the creation of the ionospheric model. We aim to filter the noise caused by the phase observations from Eqn. 2.12 and apply it directly to the one-way signals in Eqn. 2.1to remove only the noise associated with the phase observations, while retaining the real variation in the ionosphere.

For this investigation the phase observation residuals output by Track are used to compute the ionospheric delay on each GPS-to-receiver one-way signal. Then I attempt to smooth the noise from the phase residuals out of the estimate of the iono-

spheric delay with a forward Kalman filter and backward-running smoother. The forward-running Kalman filter is a sequential estimator that makes use of the measurements and covariance computed from the previous time step. Next, a backward-running Rauch-Tung-Striebel (RTS) smoother is applied to make optimal use of both the forward and backward values of the estimate and variance ([32]). The measurement noise parameter is set to reflect the actual noise in the GPS phase measurements: 1 mm. Finally, the TEC estimates are adjusted to preserve the values of the double differences computed in the initial Track run. Next, receiver positions are computed using both the GPS phase observations and TEC estimates in a third Track run. Track has been modified to input the line-of-sight TEC estimates to compute and remove the ionospheric delays on the individual one-way signals. A flow diagram of the steps in the processing for this work is shown in Fig. 2-2.

The process noise parameter in the Kalman filter characterizes the amount of variation allowed in the TEC estimate from one time step to the next. Care must be taken to set the value of the process noise such that noise from the phase residuals is minimized while preserving the actual trend of the ionospheric delay. An example of this effect is shown in Fig. 2-3. As the process noise is decreased, it has the effect of smoothing the noise of the Eqn. 2.12.

In Figure 2-1, the spectra of the L1 and L2 observations and $d\Phi_1 - d\Phi_2$ is dominated by noise at approximately 0.29 Hz. The process noise for this application was chosen to be 4.1×10^{-3} m^2/second, which produces the spectrum of the red line, with diminished power for frequencies higher than 0.005 Hz. This method was applied to 5 Hz GPS data from April 3, 2010, and April 4, 2010 (the day before, as well as the day of the seismic event). This was done so that the effects of daily-repeating multipath errors could be removed from position time histories (see, e.g., [33], [34]). Multipath errors are caused by reflections of GPS signals off nearby objects, such as buildings or wet asphalt.

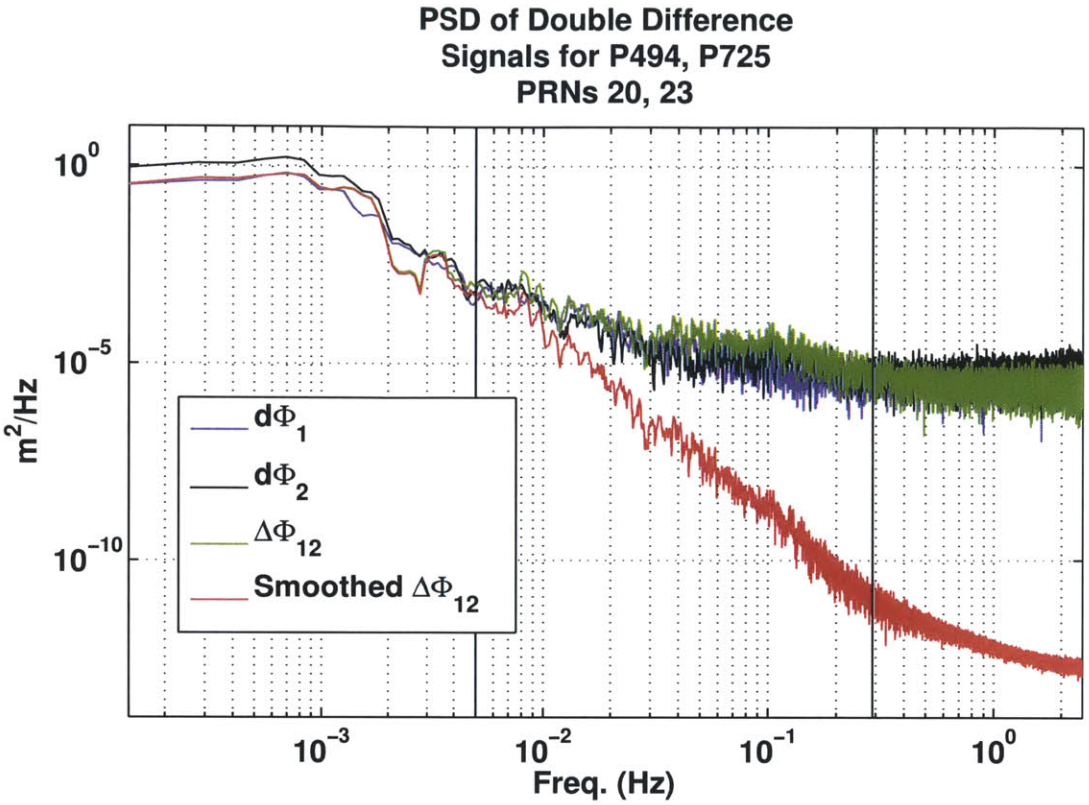

Figure 2-1: Power spectral density of the double-differenced L1 and L2 phase observations, the L1-L2 combination and the TEC, in units of m^2/Hz. The solid vertical lines mark the frequencies at 0.29 Hz, and 0.005 Hz. At 0.005 Hz, white noise begins to dominate the LC signal, and at 0.29 Hz, the smoothing of the filter applied to the ionosphere begins to diminish the LC signal power.

2.3.1 Data Description

The M_w7.2 El Mayor-Cucapah event took place at 22:40:42 UTC on 4 April 2010. The epicenter was located at 31.13N and 115.30W on the Sierra El Mayor fault, and subsequent shocks occurred along the Laguna Salada, Indiviso, Sierra Cucapah and Elsinore faults (see e.g., [35], [36] and [37]). These faults are largely parallel, and lie on the boundary between the Pacific plate and the North American plate, southeast of the San Andreas Fault. A right lateral slip of up to 2 m was detected along the Sierra Cucapah fault, and centimeter-level dynamic motion was recorded up to 200 km from the epicenter (see, e.g., [35] and [20]).

The Plate Boundary Observatory (PBO) GPS station P725 was selected as the

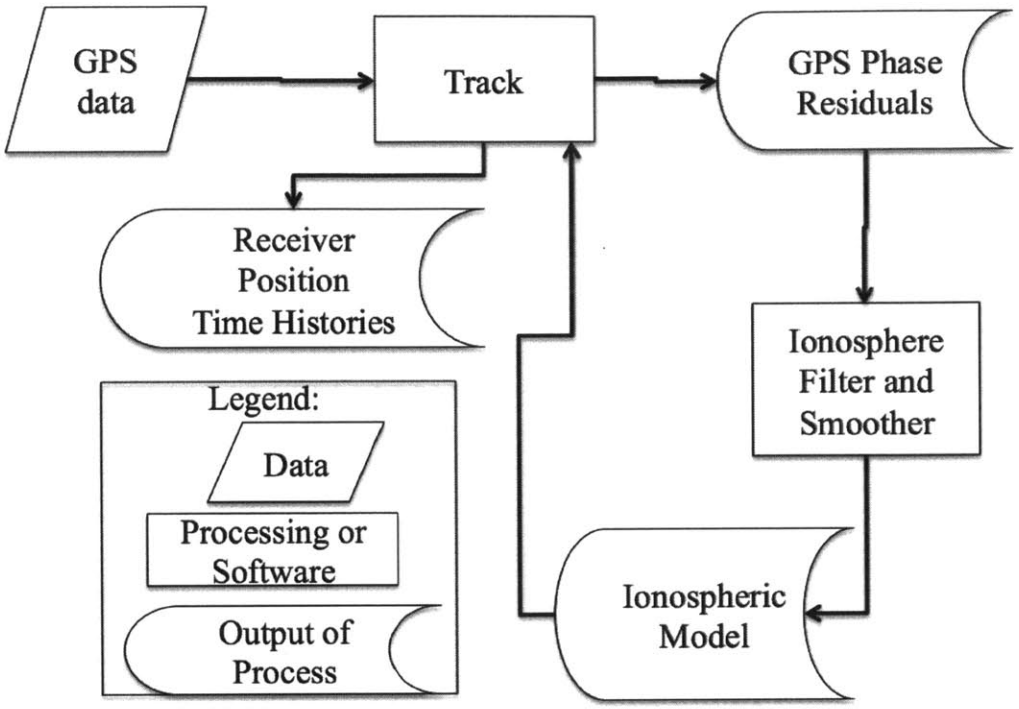

Figure 2-2: Workflow of estimating an ionospheric model and computing receiver position time histories.

reference station for 36 other stations. The rest of the stations were processed in groups of 4 to 8 stations. Distances between stations and the base station ranged from 99-713 km, and their range from the earthquake epicenter ranged from 48 to 642 km. Due to the large baselines in this study, Track was run first with the IONEX model applied to obtain an initial ambiguity estimate set. Well-determined ambiguities were then input as fixed (not free to be estimated) values into a second Track run. Next, phase residuals from the second Track run were used to estimate and smooth the ionospheric delays on each satellite's signal on each station. The line of sight ionospheric delay estimates where then applied to the phase observables in a third Track run.

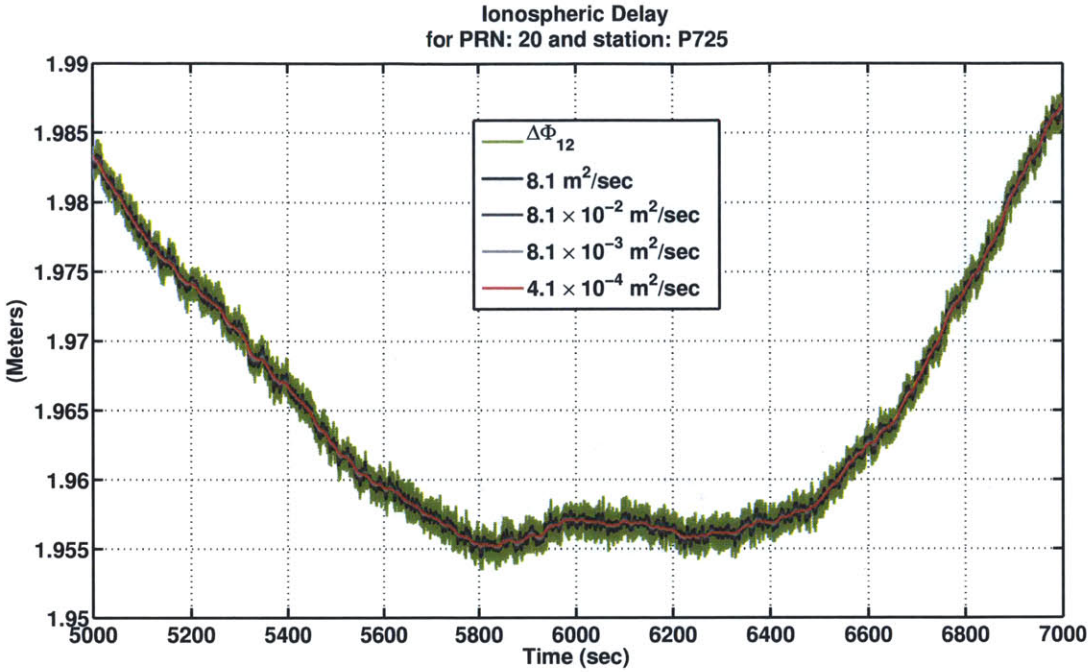

Figure 2-3: Example of the line of sight ionospheric delay in meters. The value of the ionospheric delay computed with Eqn. 2.12 is shown in green. Various levels of process noise are shown and the value of the process noise chosen for this work, PN=4.1×10^{-4} m^2/sec is plotted in red. Here $\Delta\Phi_{12}$ is shown as the green curve and should be noted as having the largest noise magnitude.

2.4 Results and Analysis

Figures 2-5 through 2-7 show the position time histories of GPS stations compared with positions computed from integrated 50-Hz data from the seismic accelerometers. Figures 2-5 and 2-6 compare the P494 station with the WES accelerometer, which is part of the Caltech Regional Seismic Network (see [38]). The two instruments are about 80 m apart (latitude: 32.76, longitude: -115.73), and roughly 70 km from the epicenter. Figure 2-5 shows the position histories during the surface wave arrival dynamics and Figure 2-6 shows ground motions after major arrival dynamics have ended.

These are surface wave arrivals (likely Rayleigh and Love waves), because the pressure and shear wave (S- and P-wave) arrival times, calculated with Tau-P software using the PREM model (see Crotwell, et al., [39]) arrive 15 and 30 seconds prior to

Figure 2-4: Map of GPS receivers used in this study. The station network is represented by small red targets. The earthquake epiceter is the large red target to the lower right of the image. The reference station is the white flag in the upper left corner, and the stations referenced in Figs. 2-5 through 2-8 are shown as white stars.

the observation of ground motion by the GPS. In addition P-waves are much more difficult to observe with GPS because they manifest in the vertical component and their amplitudes are small compared to the GPS vertical noise variance.

Figure 2-7 shows the comparison between the P742 GPS station (latitude: 33.50, longitude: -116.60) and the BZN accelerometer, which is part of the ANZA network (see [40]). These two instruments are separated by 6 km, and are roughly 184 km from the epicenter. It can be seen in Figures 2-5 through 2-7 that GPS positions match integrated accelerometer measurements well in the East and North directions, and that the largest differences occur in the height component.

Also, GPS positions in Figures 2-5 and 2-7 show the coseismic deformation, mostly visible in the east and north components. Specifically in the north components in Fig. 2-5, the GPS position readings start at roughly +200 mm, and are at 0 mm at the end of the time series. In Fig. 2-7, this can be seen in the east and north

components, where P725 starts at about +10 mm east and +10 mm north.

In these comparisons it can be seen that GPS position time histories best match the strong motion observations in the horizontal directions. Generally, vertical wave arrival dynamics are much smaller in magnitude than horizontal dynamics, which can be seen in Figs. 2-5 and 2-7. In addition, sensing millimeter-level dynamics with GPS is most difficult in the height component. The fact that application of the smoothed ionospheric model largely affected the positions in the vertical component suggests the utility of accurately modeling the ionosphere.

A 100-second moving RMS of the position histories and smoothed position histories at the P494, P742, and P485 stations is shown in Figures 2-8, 2-11, and 2-14. These were computed as the difference between the actual observed GPS trajectory and a smoothed GPS trajectory. The smoother window was chosen to be 75 seconds. The moving RMS for both the LC and L1L2 methods is most visible in the plots after the surface wave arrivals subside. The increase in the RMS in the east and north components at approximately 200 seconds represents the surface wave arrivals at the base station. Other smoother lengths and moving RMS spans also show a statistical improvement with the application of the smoothed ionospheric model. The choice of 100-seconds and 75-seconds shown here is representative of a span longer than the $\sim$ 10second period of the dynamics of the surface wave motion, and captures more long-term variation in moving RMS.

The RMS difference between the moving RMS for the LC and L1L2 methods is shown in Figs. 2.4, 2.4, and 2.4. The median LC moving RMS is greater by 1-3.5 mm in the east and north components, and by 2-6.8 mm in the height component for P494, P742, and P485. Plase plots and histograms of the moving RMS values are shown in Figs. 2.4, 2.4, and 2.4. The histograms show the distribution of the RMS difference between the LC and the L1L2 calculations. A positive median RMS difference is shown for all three stations, in each of the east, north, and height directions.

The mean RMS difference between LC and L1L2 for all the components of each GPS stations from 400-1000 seconds after the earthquake are shown in Table 2.2. In this table it can be seen that applying the ionospheric filter reduced the moving

RMS most in the height component, by approximately 4 mm. In the east and north components, the mean reduction was 1.9 mm and 2.3 mm, respectively.

Stacks of the GPS position time histories for all 36 GPS stations in this study are shown in Figures 2-17, 2-18, and 2-19 for the East, North and height components. The wave form stacks in these figures show that GPS observations can be used to compute surface wave speeds. S- and P-waves arrivals are computed using the PREM model in Tau-P software (see Crotwell, et al., [39]). The P- and S-arrival times are represented as vertical red lines in the figures, and the surface waves captured by GPS arrive approximately 10-15 seconds after the predicted S-arrival.

It should be noted that the surface wave arrivals at the base station, P725 can be seen in at all of the stations in each of the east, north and height stacks at roughly 220 seconds after the earthquake. This is a characteristic of computing the positions of a network of roving GPS stations while holding the base station fixed. When the surface waves arrive at a station which is held fixed in the calculation, the motion of the fixed station becomes observable in the stations which have positions that are allowed to vary.

Surface wave speeds computed by fitting a linear trend to the detection of the waves in the GPS position histories is shown in Table 2.3. The surface wave speeds are 3.97 km/s in the east component, 3.83 km/s in the north component, and 3.05 km/s in the height. These might strike the reader as high for surface waves, especially for sedimentary basins like those near the Salton Sea. Tomographic studies of this region, however, suggest Rayleigh and Love wave speeds of up to 4.0 km/s in the region within 200 km of the Salton Sea, where the vast majority of the GPS stations in this study are deployed (see Shapiro, et al., [41], and Sabra et al., [42]). Slower surface speeds are predicted in these investigations, but in the Los Angeles basin, and 300 km to the northwest in the San Jaoquin valley, where we have used relatively few GPS receivers.

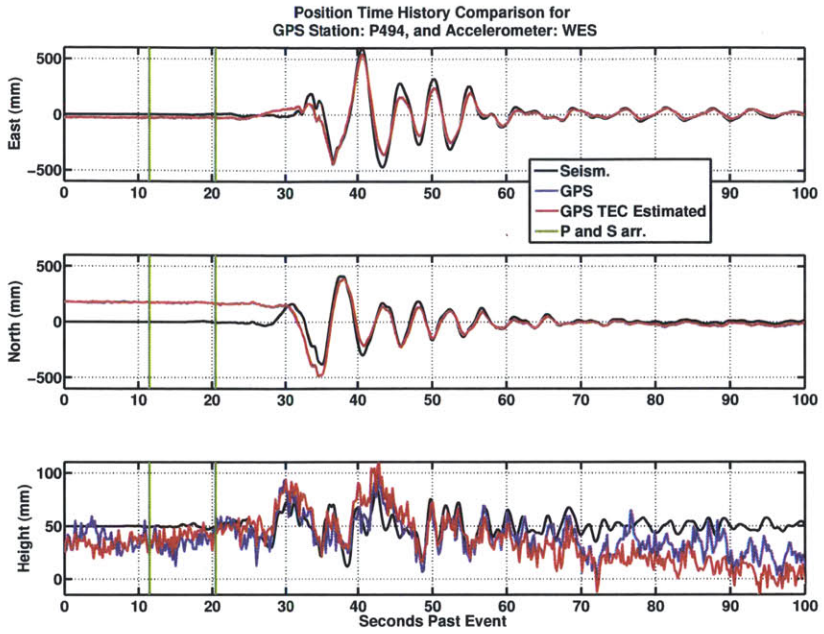

Figure 2-5: Integrated seismometer accelerations from the WES station compared with GPS positions estimated from the P494 station. The black line represents positions computed from integrated accelerometer measurements. The blue line shows the GPS position time history with the ionospheric delay computed using Eqn. 2.9. The red line shows the GPS position time history with the ionospheric delay smoothed.

2.5 Conclusions

In this work the line of sight ionospheric delay computed from GPS phase observations was smoothed and removed from the phase measurements. The position noise reductions shown here illustrate the necessity of accurately modeling the ionosphere for computing GPS station positions in networks with baselines over 3 km in length. The application of this technique resulted in a decreased station position noise in both the horizontal and vertical components. The noise reduction was most visible in the vertical component of the GPS positions. GPS position time histories showed agreement with nearby strong-motion sensors in the horizontal components. Although the application of the smoothed ionospheric model decreased noise in the GPS height measurements, GPS observations in the height components captured less ground motion than the accelerometers. This is possibly due to the fact that vertical

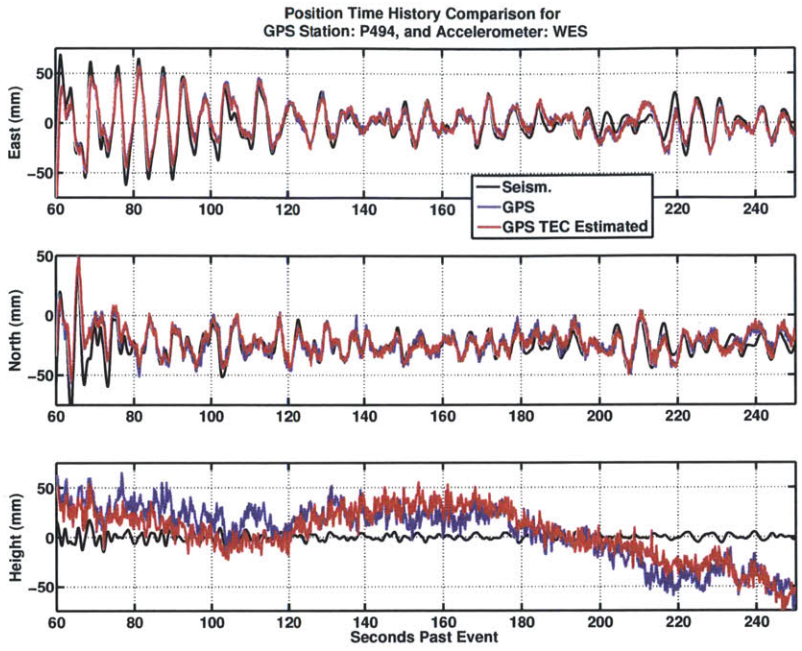

Figure 2-6: Zoom of earthqquake coda for the P494 GPS station and WES accelerometer station. The black line represents positions computed from integrated accelerometer measurements. The blue line shows the GPS position time history with the ionospheric delay computed using Eqn.2.9. The red line shows the GPS position time history with the ionospheric delay smoothed.

ground motions have amplitudes which are much closer to the noise variance of the GPS positions in the vertical component.

The fact that arrival dynamics are much larger in magnitude in the horizontal components than in the vertical illustrates the necessity of improving GPS observations in the vertical component. This is where room for further improvement of the technique applied in this work still lies. To further decrease the noise in the vertical component, one might suggest further decreasing the process noise applied in the Kalman filter. Simply smoothing the ionospheric model without an informed selection of Kalman filter process noise, however, can result in the removal of actual dynamics of the ionosphere, which can then be injected into the computed GPS positions.

A subsequent step to this work could be the estimation of a local ionospheric thin-screen model, which makes use of the line of sight estimates from each receiver-

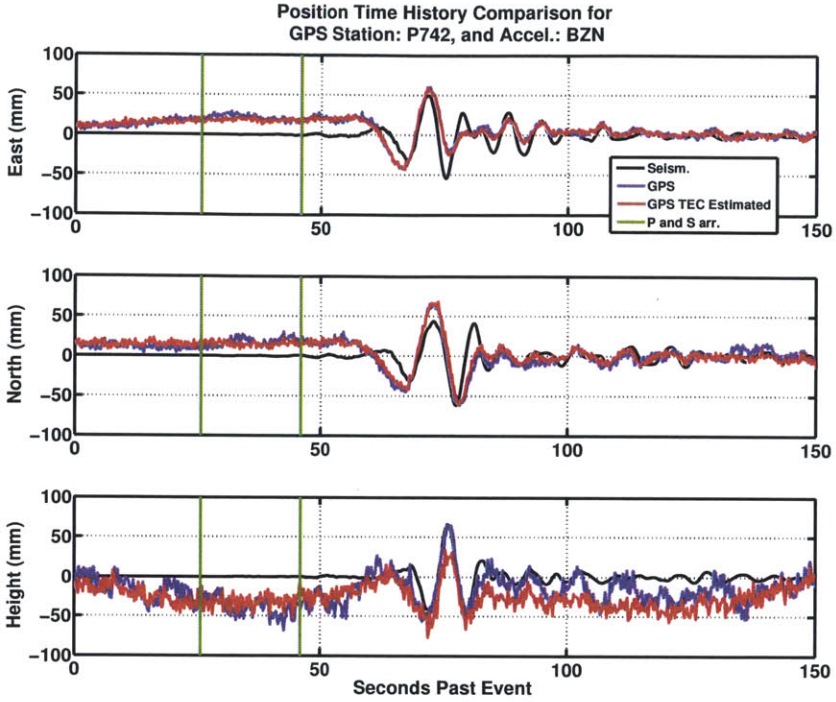

Figure 2-7: Integrated seismometer accelerations from the BZN station compared with GPS positions estimated from the P742 station. The black line represents positions computed from integrated accelerometer measurements. The blue line shows the GPS position time history with the ionospheric delay computed using Eqn. 2.9. The red line shows the GPS position time history with the ionospheric delay smoothed.

to-satellite estimate of the ionospheric delay. In this way the ionospheric applied to the phase observations of each receiver could be informed by that of its neighbors. This could aid in the estimation of GPS phase ambiguities, which could in turn improve positioning uncertainties. It would also provide an image of actual local ionospheric dynamics.

The analysis of this network also shows the utility in using high-rate GPS data for seismological observations. The wave form stack of station positions can be used to estimate surface wave speeds, and GPS position time histories can capture much of the horizontal motion observed by co-located accelerometers. Improvements are still needed to refine GPS height observations to observe vertical motions. Accurately modeling the ionospheric delay will be essential in this objective, especially as we

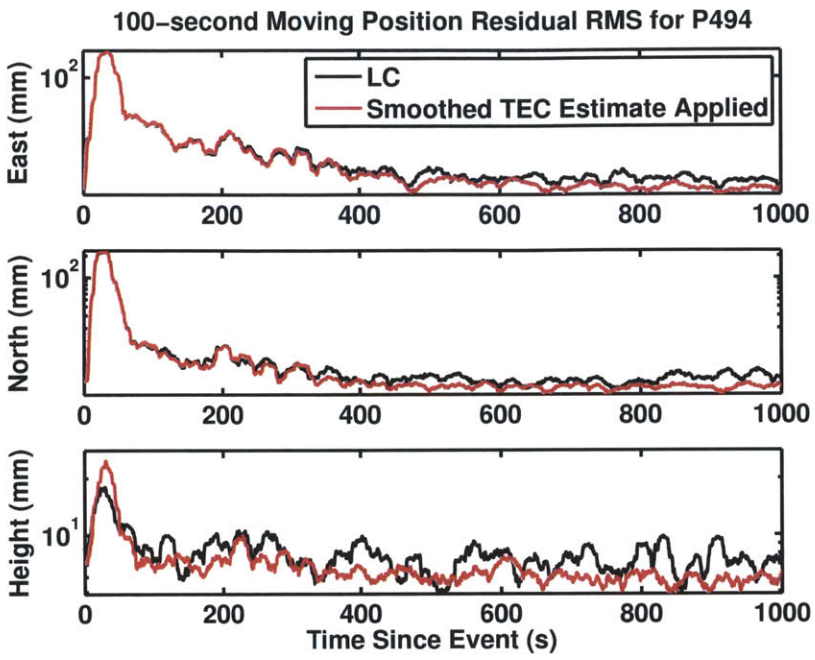

Figure 2-8: The 100-second moving RMS with respect to a smoothed position history for both the LC and L1L2 position time histories, for the P494 station. In the all three components the surface wave arrivals at P494 can be seen prior to 100 seconds, and in the east and north components, the slight increase in the RMS at 220 seconds represents the surface wave arrivals at the base station.

approach solar minimum, and the dynamics of the ionosphere become more quiescent. The technique applied here will be most applicable during periods of minimum ionospheric activity because the noise from GPS measurements will be easier to isolate from variation in the ionosphere. This will make filtering the noise of the phase observable without filtering actual ionospheric dynamics will be easier. Finally as the GPS equipment improves and becomes more prevalent, techniques such as the one applied in this work will become more useful in realizing the full scientific potential of GPS.

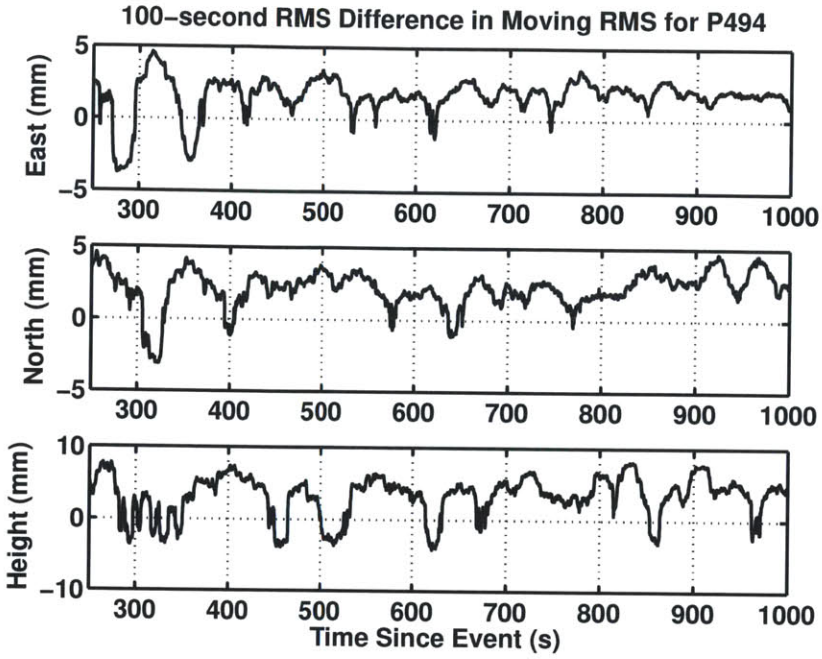

Figure 2-9: RMS difference of between the LC and L1L2 moving RMS values plotted in Fig. 2-8.

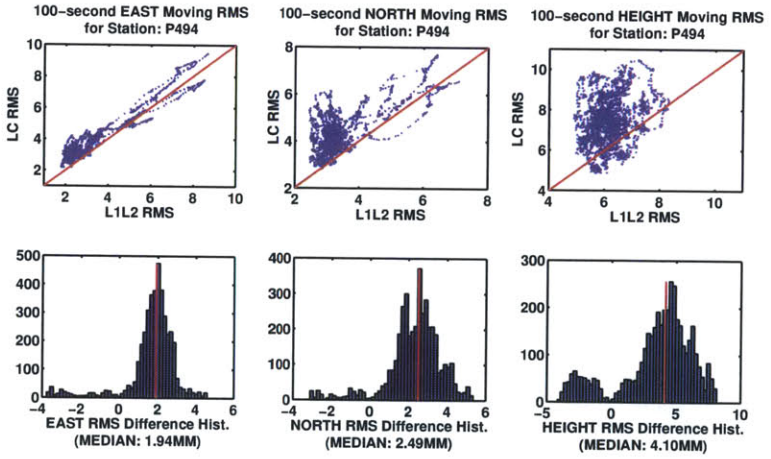

Figure 2-10: Comparison of the difference in LC and L1L2 RMS differences for station P494. The top three subfigures compare the LC RMS to the L1L2 MRS. The red line is the 1:1 demarcation. Points plotted above the line indicate the L1L2 method had a lower RMS than the LC method. The bottom three subfigures show a histogram for the RMS difference between the moving RMS of LC and L1L2 for the east, north, and height components.

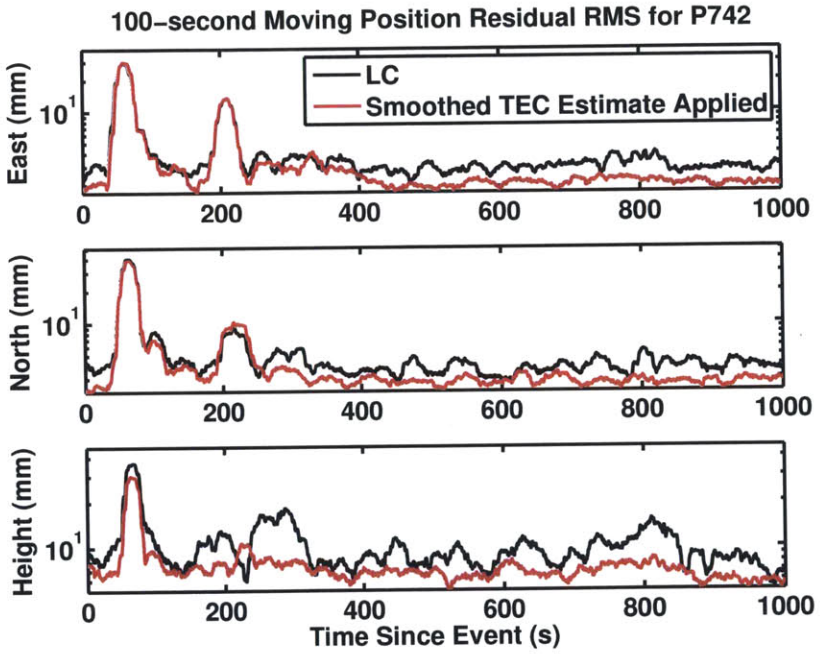

Figure 2-11: The 100-second moving RMS with respect to a smoothed position history for both the LC and L1L2 position time histories, for the P742 station. In the all three components the surface wave arrivals at P742 can be seen prior to 100 seconds, and in the east and north components, the slight increase in the RMS at 220 seconds represents the surface wave arrivals at the base station.

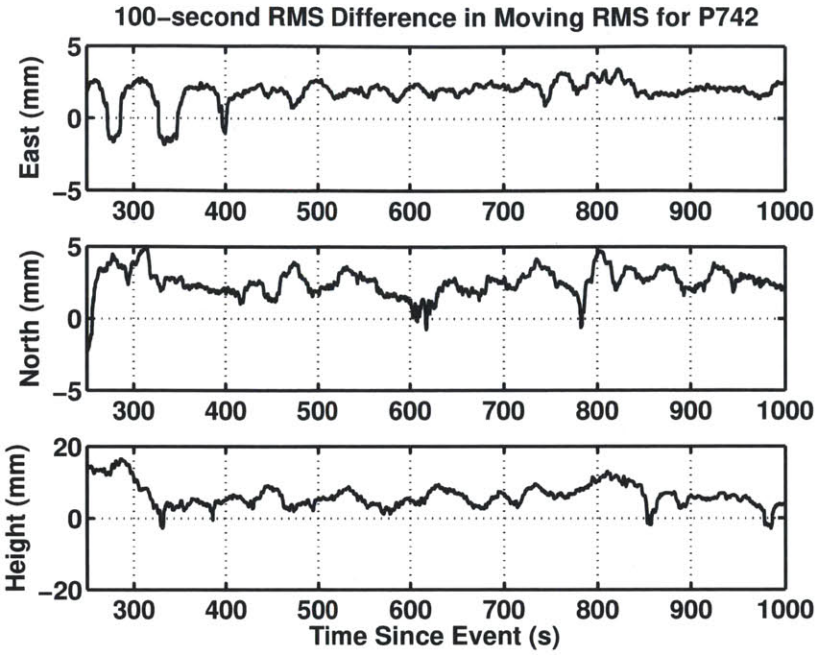

Figure 2-12: RMS difference of between the LC and L1L2 moving RMS values plotted in Fig. 2-11.

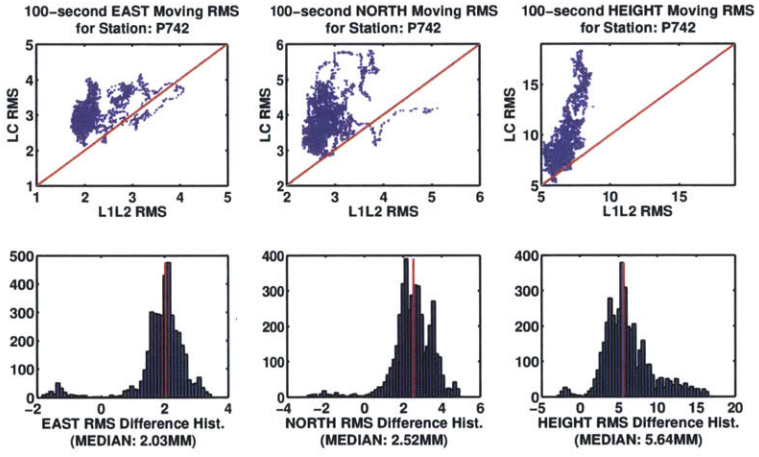

Figure 2-13: Comparison of the difference in LC and L1L2 RMS differences for station P742. The top three subfigures compare the LC RMS to the L1L2 MRS. The red line is the 1:1 demarcation. Points plotted above the line indicate the L1L2 method had a lower RMS than the LC method. The bottom three subfigures show a histogram for the RMS difference between the moving RMS of LC and L1L2 for the east, north, and height components.

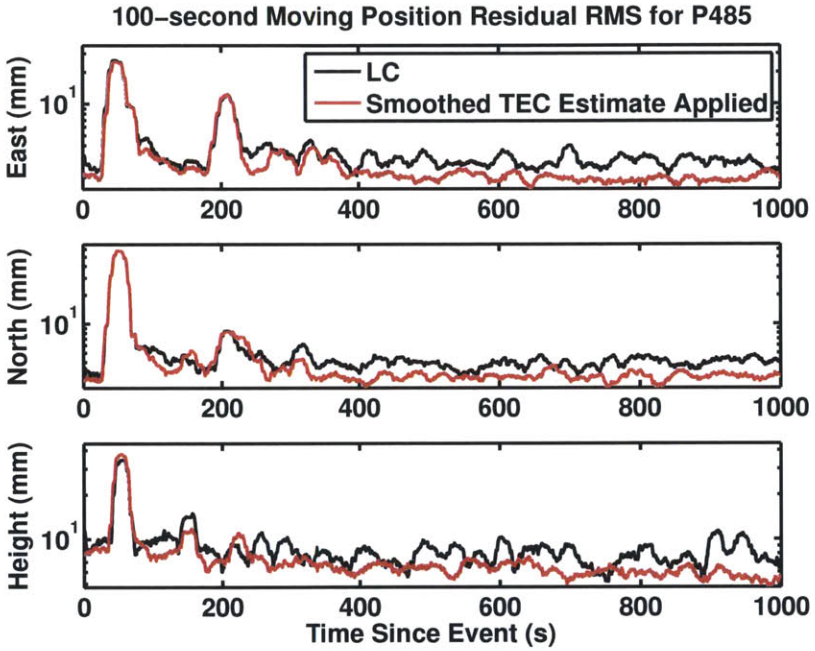

Figure 2-14: The 100-second moving RMS with respect to a smoothed position history for both the LC and L1L2 position time histories, for the P485 station. In the all three components the surface wave arrivals at P485 can be seen prior to 100 seconds, and in the east and north components, the slight increase in the RMS at 220 seconds represents the surface wave arrivals at the base station.

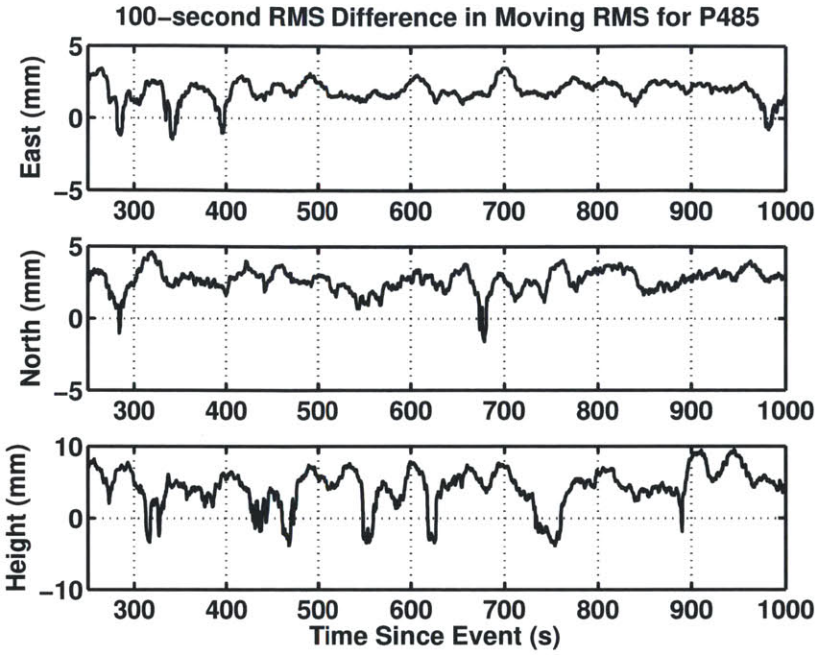

Figure 2-15: RMS difference of between the LC and L1L2 moving RMS values plotted in Fig. 2-14.

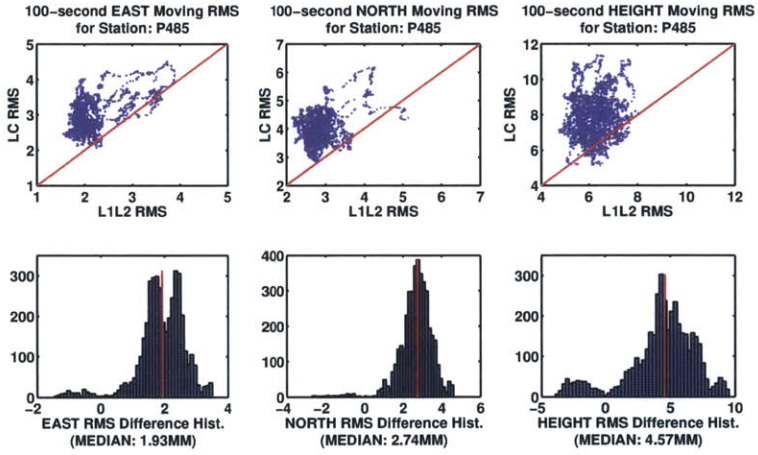

Figure 2-16: Comparison of the difference in LC and L1L2 RMS differences for station P485. The top three subfigures compare the LC RMS to the L1L2 MRS. The red line is the 1:1 demarcation. Points plotted above the line indicate the L1L2 method had a lower RMS than the LC method. The bottom three subfigures show a histogram for the RMS difference between the moving RMS of LC and L1L2 for the east, north, and height components.

Station	East (mm)	North (mm)	Height (mm)
CRRS	2.08	1.87	4.28
GLRS	1.70	2.16	4.45
HNPS	2.19	2.90	5.90
IID2	1.46	2.43	4.68
P066	1.55	1.97	3.24
P300	2.50	2.12	4.43
P472	1.47	2.19	3.70
P473	1.75	2.24	3.61
P480	1.82	2.46	3.78
P481	1.56	1.93	2.91
P482	1.67	2.21	3.22
P483	1.68	2.11	2.23
P484	2.04	2.43	4.00
P485	1.91	2.66	4.27
P487	1.88	2.23	4.57
P488	2.11	2.55	3.93
P489	2.40	2.74	5.15
P491	1.92	2.81	5.40
P492	1.69	2.17	3.88
P494	1.72	2.33	3.44
P495	1.87	1.70	3.77
P496	1.69	2.28	4.17
P497	1.03	1.66	3.12
P498	1.99	2.45	3.81
P499	1.43	1.66	2.37
P500	1.42	1.76	3.39
P504	2.63	3.49	5.36
P507	1.70	2.20	3.26
P508	1.83	2.13	3.50
P553	1.69	1.82	3.68
P607	2.27	3.05	6.84
P742	1.88	2.49	6.21
P744	1.62	1.98	3.14
SLMS	2.01	1.95	4.49
USGC	1.96	2.80	3.67
WGPP	2.16	2.67	5.01
MEAN	1.84	2.29	4.08

Table 2.2: Mean RMS differences in millimeters between applying Eqn. 2.9 and the smoothed ionospheric model with a process noise of 5.0×10^{-6} TECU^2/epoch. These are the mean of the RMS differences from 400 seconds to 1000 seconds after the earthquake.

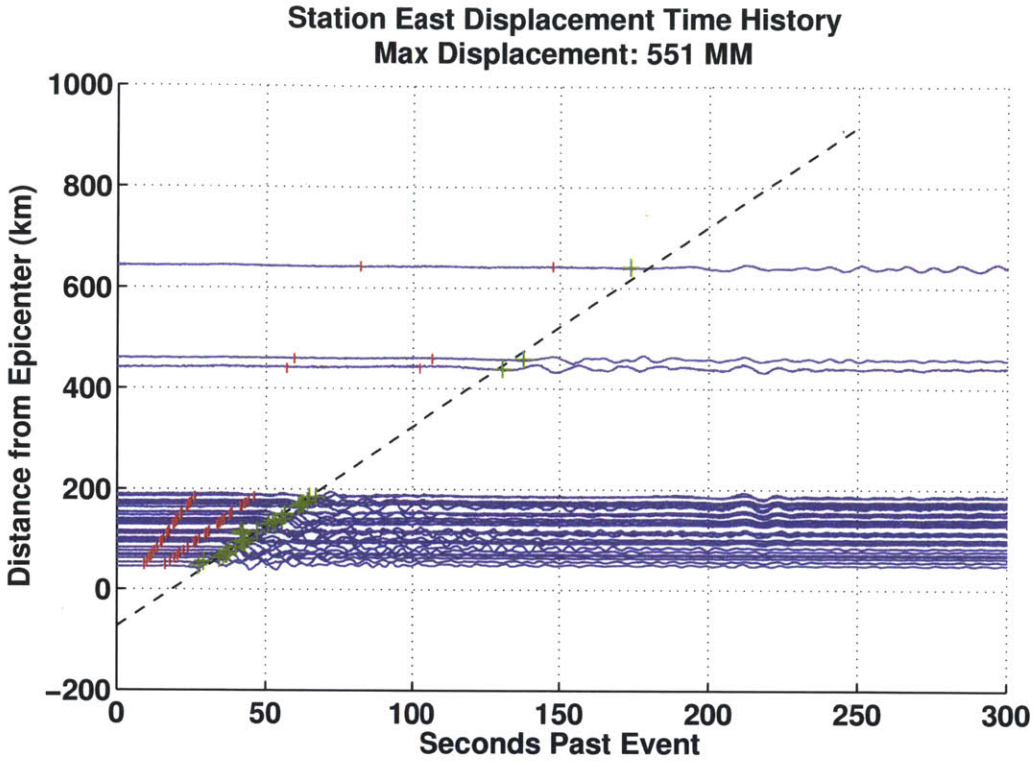

Figure 2-17: Stack of normalized east displacements as a function of distance from the estimated earthquake epicenter. Red vertical lines indicate the calculated P and S wave arrival times calculated with the PREM model using Tau-P software. Green "+" signs indicate the surface wave arrival time, and the dashed black line shows the best fit of a line through these points. The slope of this line indicates the surface arrival velocity was 3.97 km/s in the east component. Also it should be noted that at roughly 220 seconds after the event the same wave form can be seen at each station, which is representative of the surface wave arrivals at the base station P725.

Component	East (km/s)	North (km/s)	Height (km/s)
Speed	3.97	3.84	3.05

Table 2.3: Surface wave speeds calculated from GPS trajectories. These were calculated by fitting a linear trend to the times at which the surface waves arrived at each station.

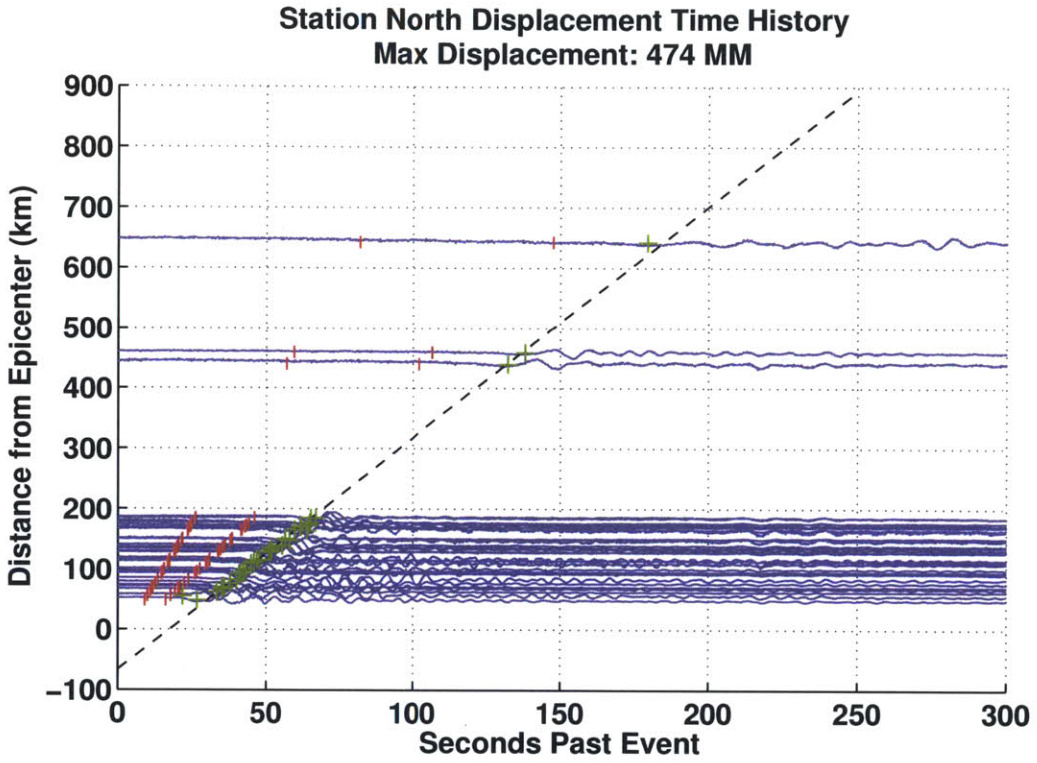

Figure 2-18: Stack of normalized north displacements as a function of distance from the estimated earthquake epicenter. Red vertical lines indicate the calculated P and S wave arrival times calculated with the PREM model using Tau-P software. Green "+" signs indicate the surface wave arrival time, and the dashed black line shows the best fit of a line through these points. The slope of this line indicates the surface arrival velocity was 3.84 km/s in the north component. Also it should be noted that at roughly 220 seconds after the event the same wave form can be seen at each station, which is representative of the surface wave arrivals at the base station P725.

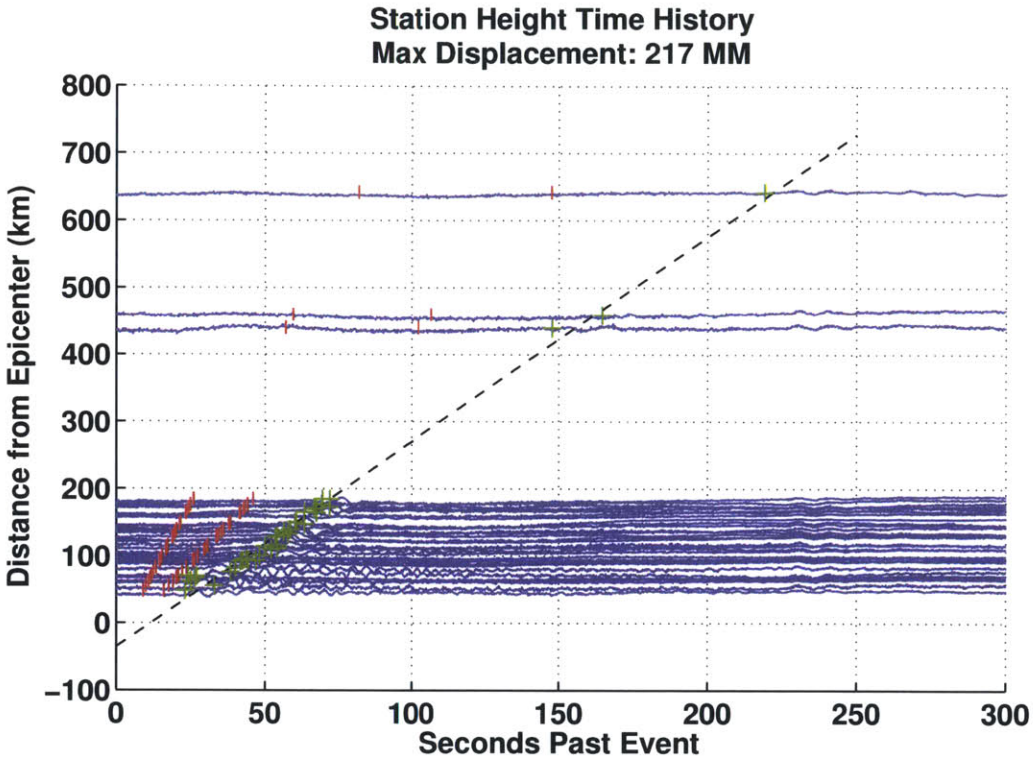

Figure 2-19: Stack of normalized height displacements as a function of distance from the estimated earthquake epicenter. Red vertical lines indicate the calculated P and S wave arrival times calculated with the PREM model using Tau-P software. Green "+" signs indicate the surface wave arrival time, and the dashed black line shows the best fit of a line through these points. The slope of this line indicates the surface arrival velocity was 3.05 km/s in the height component. Also it should be noted that at roughly 220 seconds after the event the same wave form can be seen at each station, which is representative of the surface wave arrivals at the base station P725.

Chapter 3

Effect of Ionospheric Modeling on Airborne Gravimetry with Data from NOAA Aircraft

3.1 Abstract

In this work, the effect of smoothing the contribution of the ionospheric delay on GPS phase observables utilized in the kinematic GPS software "Track" is studied with application to airborne gravimetry. The accuracy of airborne gravimetry relies on the positioning quality of gravimeter measurements using GPS observables. The noise in the treatment of the ionosphere for kinematic GPS can contribute up to 1 mGal of error for the final gravity solution (see Bruton [43]). Gravity profiles are most sensitive to the height component of the aircraft position, and improvements in lateral positioning result in better registration of gravity measurements to the surface of Earth. Therefore, any improvements in the positioning of gravity measurements will result in improved gravity products. Here, GPS phase measurements are utilized both for precise aircraft positioning as well as in the calibration and estimation of various offsets in gravimeter readings. Typically the ionosphere can represent up to 10s of meters of delay on the GPS pseudorange and phase observables, and depending

on how the ionospheric delay is treated, can inject noise on the order 3× that of the GPS phase observables, or up to 9 mm, into the position calculation.

In this work the technique described was applied to GPS data collected for the NOAA/NGS GRAV-D project. The purpose of the dataset presented here was the calibration of the instrumentation and techniques used. It contains four reflights of the same approximate latitude. These co-located trajectories were computed using the Track software, which is the differential kinematic GPS software maintained at MIT (see, e.g., Herring et al., [28]). Aircraft trajectories computed with Track were then used to calibrate gravimeter measurements using the "Newton" software of the NOAA NGS [44], and the resulting gravity profiles were compared in terms of repeatability. A span of filter smoothing parameters were examined for both the filter applied to the ionosphere and the low-pass filter used on gravimeter measurements. Application of the ionospheric model affected GPS heights by up to 20 cm, and it was found that an optimal selection of filter parameters resulted in an RMS improvement of 0.6 mGal when applying the ionospheric model.

3.2 Introduction

The aim of this work is to improve airborne gravimetry through the application of an ionospheric model in a kinematic differential GPS processing scheme. In differential GPS, signals are differenced between receivers and spacecraft to counter a variety of errors. This technique is most commonly used to cancel the effect of clock biases in receivers and the spacecraft (see Leick, [22]). It is also utilized to cancel delays caused by the neutral atmosphere and ionosphere (see Grewal [21]).

Differencing to cancel ionospheric and atmospheric effects works over short baselines, which are generally under 3 km. This is because receivers that are close to one another record GPS signals that pass through relatively similar parts of the ionosphere and atmosphere. As the receivers are moved farther apart from one another, they observe signals through different portions of the ionosphere and atmopshere, and the assumption that its effect will cancel begins to break down (see Bruton, [45]).

An example of the ionospheric profiles that were observed by the COSMIC spacecraft constellation on the day of the airborne survey studied in this work are shown in Figure 3-1. The COSMIC constellation are a fleet of six spacecraft in low Earth orbit that are equipped with GPS receivers. They record over 2000 radio occultations per day and are useful for constructing global ionospheric maps (see Anthes, et al., [46]).

Fig. 3-1 illustrates some of the ionospheric variation which affects precise GPS positioning over long baselines and long-duration data collections. The map shows the point of closest approach of the occultation to the surface of Earth. Because the GPS spacecraft, the COSMIC spacecraft, and the Earth are in motion, this point can track for 1000s of km across the surface. The map shows large variations in the total electron content (TEC) over North America, and over the 6 hour period in which the flight takes place. The ionosphere typically has one or two peaks in TEC between 100 and 400 km see Bilitza [47]). The profiles show the TEC in TEC units (TECU); 1 TECU causes about 16 cm of line-of-sight delay on the GPS L1 observable. The large increases in the TEC at low altitudes are an artifact of the Abel inversion used in their computation (see Hysell [48]).

This investigation focuses on the effect of the ionosphere on GPS phase observables. The ionosphere is a dispersive medium, which means its effect on electromagnetic signals is frequency-dependent (see Klobuchar, [25], and Grewal et al., [49]). The GPS L1 and L2 frequencies are broadcast at 1575.42 MHz and 1227.60 MHz, respectively. The difference in the GPS frequencies allows the calculation and removal of the ionospheric contribution through the use of linear combinations of the observables (see Herring et al., [28]). Generally an ionosphere-free linear combination of the phase observables is used in the differencing scheme to cancel the effect of the ionosphere. Because this relies on a combination of the observables, however, it increases the noise in the quantities used to compute receiver positions in an RMS sum sense by a factor of ~ 3, to approximately 9 mm. In this work, an ionospheric model is proposed which filters the noise contribution of the GPS phase observables. This can be seen in Figure 3-2. The power spectral density (PSD) of the phase residuals, dL1 and dL2, are plotted along with the spectrum of the ionosphere-free linear com-

bination of the phase residuals, dL1-dL2. The spectrum of the smoothed ionospheric model, which has the lowest high-frequency power, is also shown.

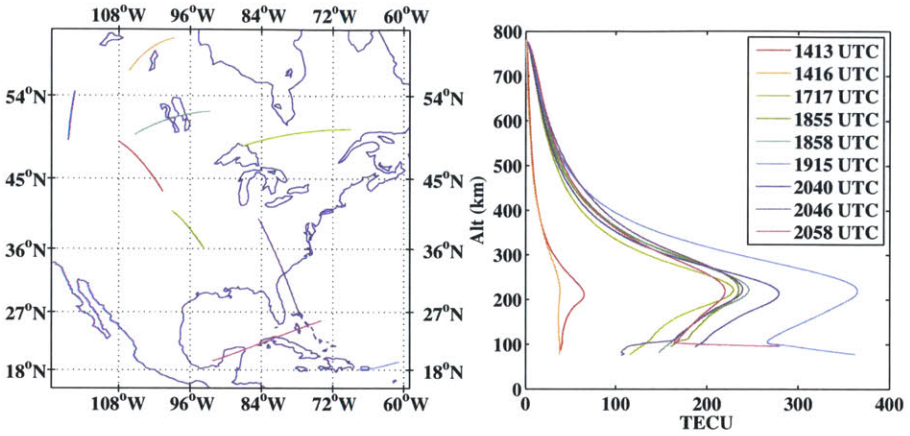

Figure 3-1: Profiles of the ionosphere observed by the COSMIC constellation radio occultations with GPS signals on 2012 DOY 365 during the flight period. The map shows the point of closest approach, or the impact parameter, of the radio occultation, which was smeared by spacecraft motion, and the Earth rotation. The vertical profiles on the left show the TEC observed at the impact parameter as it moves away or toward the Earth's surface which is dependent on the rising or setting geometry of the spacecraft.

3.2.1 Airborne Gravimetry

Aircraft are used for gravimetry surveys when areas of coverage are large and/or inaccessible by other means. The data studied in this project were gathered by the National Oceanic and Atmospheric Administration (NOAA) as part of the Gravity for the Redefinition of the American Vertical Datum (GRAV-D) project [44]. GRAV-D is a survey of the geoid in the United States and its territories to aid in the measurement of the height of the vertical datum to ±2 cm. Data products from this project will be used for landslide risk and floodplain mapping. These objectives depend heavily on the quality of aircraft positioning, and specifically aircraft height knowledge. To investigate a variety of kinematic GPS processing capabilities, NOAA made a calibration dataset available to the kinematic GPS community in 2010 (see Damiani, et al., [50]). The aircraft positioning requirements for the GRAV-D project

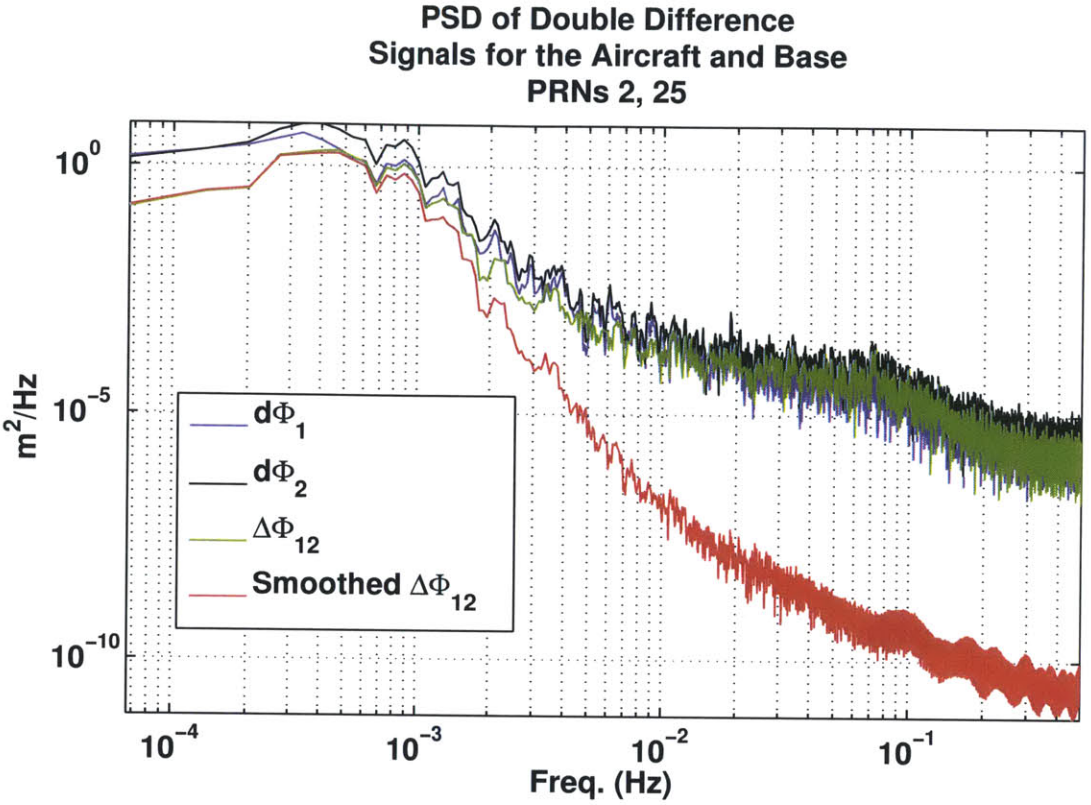

Figure 3-2: The PSD of the GPS L1 and L2 phase residuals, labeled dL1 and dL2 is plotted in blue and black, respectively. The PSD of the difference between the phase residuals, dL1-dL2, is shown in green, and the PSD of the the ionospheric model presented in this research is shown in red. The noise inherent in the linear combination of the phase residuals, $\Delta\Phi_{12}$, is mitigated by using a Kalman filter with a process noise of 1×10^{-3} TECU^2/second. Here it can be seen that the power of the spectrum is minimized for frequencies greater than 10^{-3} Hz.

are 30 cm in height, and 10 cm for horizontal component accuracy.

Aircraft are used in this survey because the area of coverage is large. Airborne gravimetry also provides a level of spatial resolution between that of ground- and space-based techniques. The resolution of space-based gravimetry is dependent on the orbit altitude. The current gravity model produced with measurements from the Gravity Recovery and Climate Experiment (GRACE) mission, which orbits at approximatly a 500 km altitude, has a gridded resolution of $\sim$ 100 km (see [51]). This resolution is too coarse for the GRAV-D survey since the geoid can vary by 10 m (3 mGal in free air anomalies) at resolutions finer than 110 km (see Pavlis [52]).

On airborne gravity surveys, the instrumentation generally consists of a gravimeter, a GPS receiver, and an inertial measurement unit (IMU). The aircraft moves very fast compared with terrestrial or nautical surveys, and is subject to a variety of effects which can degrade the fidelity of the estimated gravity field. The atmospheric and ionospheric delay, multipath reflections and turbulence can degrade the GPS solution. For the gravimeter measurements, aircraft motion is the dominant source of error, which accelerations from differentiated GPS positions are used to correct [45]. Other gravimeter errors exist in the determination of the still reading in the case of relative gravimeters, the drift rate, and the offlevel error inherent the stabilization of the gravimeter platform (see Peters and Brozena [53]).

3.3 Methodology

The data processing steps for this work are shown in the flow diagram in Fig. 3-3. We use the GPS phase observables in Track software to calculate the position of the aircraft and, using a lever-arm, the position of the gravimeter. The GPS positions are then differentiated to compute accelerations and used to calibrate gravimeter measurements, as well as calculate several adjustments applied to the gravity measurements, such as the Eötvös correction, and the offlevel corrections. In the case of the NOAA GRAV-D project, GPS measurements are coupled with IMU data to provide smooth trajectories in a differential GPS processing software of NOAA National Geodetic Survey (NGS). It should be noted here that Track currently does not have the capability of using IMU data, so measurements from the IMU are not used in the Track solutions computed in this investigation. There are analyses presented of the GPS-only Track solution compared with the GPS and IMU solutions computed by the NOAA NGS. Track first computes a coarse position time history using GPS pseudorange observables. Next, it searches for discontinuities in the widelane combinations of the phase observables and assigns floating-point values to them. The phase ambiguities are then fixed to integers, if possible, through the use the algorithm described by Dong and Bock, [29]. A smoother is then applied to the final position time

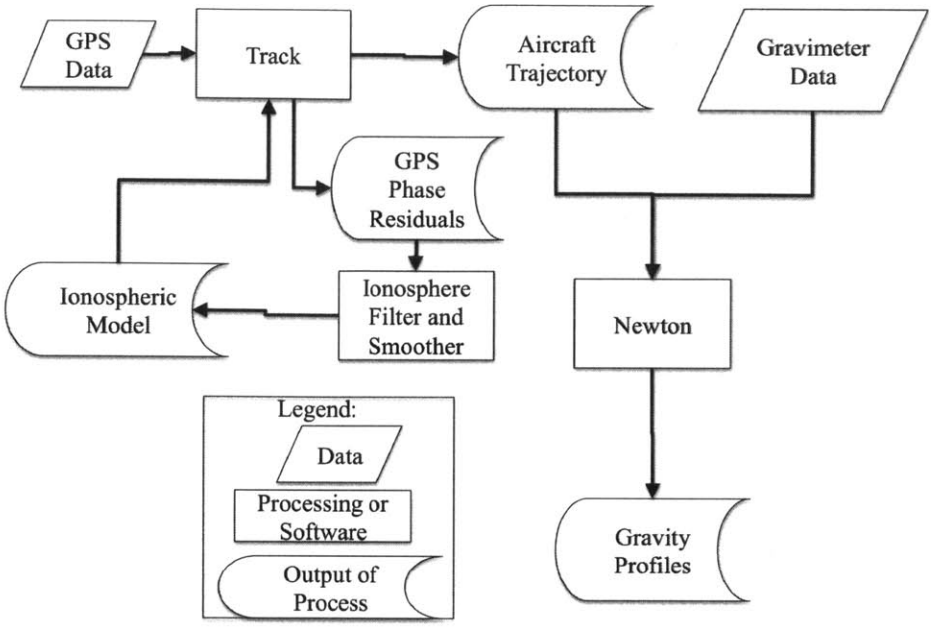

Figure 3-3: Workflow of the Track and Newton software for this project. First GPS RINEX data are processed by Track, which estimates the aircraft trajectory and also produces the residuals of the GPS phase observables. The filter which estimates and smooths the ionospheric delay does so using the phase residuals. These line-of-sight TEC values are then inputted into Track for a second run. The aircraft trajectory from Track with and without the ionospheric model applied are then used along with gravimeter data in Newton to compute gravity profiles.

history.

"Newton" is the airborne gravimetry software developed by the NOAA NGS (see Damiani, et al., [44]). It is used to combine GPS and gravimeter data to produce accurate gravity profiles. Newton applies calibrations and corrections to gravimeter data in the calculation of the gravity profiles. Newton calculates the difference in position between the gravimeter and the GPS receiver, timing offsets between GPS and gravimeter measurements, and an offlevel correction. The offlevel correction counters the effect of incorrect gravimeter stabilization due to horizontal aircraft accelerations (see Peters and Brozena [53]). After these corrections are applied, the gravimeter data are filtered using a Hanning window, Newton computes free air disturbances (FADs). This process is described in Sec. 3.5.

Accurate GPS positions are useful in this process for the calculation of the various

offsets described above, and for determining the gravimeter still readings, which are estimated using GPS measurements when the aircraft is at rest before and after the flight. The position component with the largest effect on gravity profiles is the height component, and any improvement to this measurement in terms of the magnitude or short-period noise characteristics can have a positive impact on the final gravity model. Finally, performance is characterized by comparing the co-located gravity profiles in terms of their residual RMS with respect to their mean, and their correlation. They are also compared with the EGM08 gravity model.

3.4 Data Used for Airborne Gravimetry

The data used to study the application of the ionospheric model is a calibration dataset which the NOAA NGS contracted. Data consisted of measurements from GPS receivers, a gravimeter, and an IMU. The gravimeter was a Micro-g LaCoste Turn-key Airborne Gravimeter System (TAGS) [54]. The laboratory precision of the TAGS is 0.01 mGal (see, e.g., [55], [56]), and the data rate is 1 Hz. The IMU used was an Applanix POS/AV, which operated at 10 Hz [57]. The IMU data were not utilized in the computation of GPS positions and the application of the ionospheric filter using the Track software.

The GPS receiver on the aircraft and at the base station were each NovAtel DL4+ instruments, and logged measurements at 1 Hz. The aircraft receiver's antenna was mounted on top of the fuselage. The flight studied for this work took off from Rapid City Regional Aiport in South Dakota on December 30 2012, and flew four repeating ground east-west tracks, at approximately 44 deg. Latitude, which were each approximately 220 km long (see map in Fig 3-4), and two north-south tracks. Only the east-west tracks were considered in this study. The aircraft used was a Cessna Conquest, shown in Fig. 3-5, which was flown at a velocity of 120 m/s and an altitude of 6000 m. The base station's receiver was positioned at the airport, about 500 m from the aircraft parking position. This flight took place from 07:09 to 14:17 local time on December 30 in 2012.

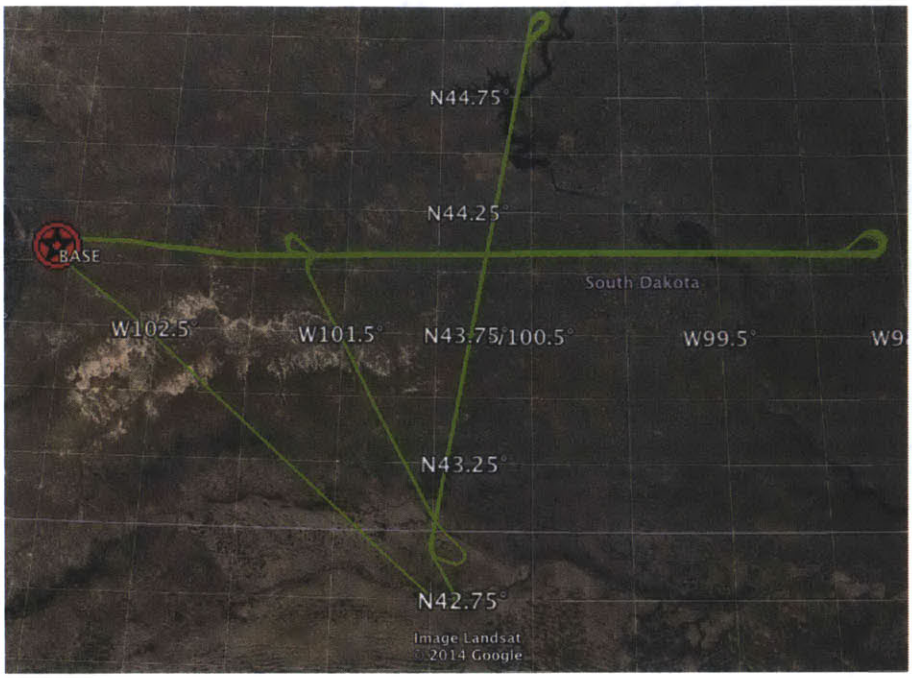

Figure 3-4: Ground tracks flown by the aircraft in South Dakota. The airport, labeled "BASE" is the Rapid City Regional Airport, which is where the base station for the kinematic processing was deployed. The East-to-West tracks are approximately 220 km long.

Figure 3-5: Example of Cessna Conquest aircraft used in this study.

3.5 Free Air Disturbance Profiles

The affect of applying the ionospheric model to the GPS data is assessed by a comparison of "free air disturbances" (FAD) calculated by the Newton software. The FAD is the measured gravity at altitude corrected with an approximation of the Earth's normal gravity at the altitude of measurement (see Damiani, [58], and Preaux and Damiani, [59]). Gravity disturbances are often corrected using a normal gravity computed on the surface of the WGS84 ellipsoid, with a free air correction applied to account for the measurement at altitude (see Heiskannen and Moritz, [60], and Hackney and Featherstone, [61]). The FADs presented here incorporate the affect of altitude by computing the normal gravity at the altitude of measurement through the definition of an ellipsoid confocal with that of WGS84, but with axes defined so that the ellipsoid intersects the aircraft altitude. This is described in the appendix of Pavlis, et al., [52]. The confocal ellipsoid has an associated Somigliana-Pizzetti gravity formulation which is used to compute the normal gravity (see Heiskannen and Moritz, [60]).

To compute the FAD, Newton first calibrates the raw gravimeter beam velocity, $\dot{b}$, output for cross coupling, spring tension and scaling (see [44] and [56]). The corrected beam velocity $\dot{b}_{\text{corr}}$ has units of milligals. The unfiltered full field gravity (FFG) is given by:

$$g_{ffg} = \dot{b}_{\text{corr}} - a_{\text{vert}} + c_{\text{O}} - c_{\text{drift}} + c_{\text{tie}} \tag{3.1}$$

where a_{vert} is the vertical acceleration sensed caused by flight in a rotating reference system, given as the vertical component of [44]:

$$\mathbf{a} = \frac{d^2\mathbf{r}}{dt^2} + 2\boldsymbol{\omega} \times \frac{d\mathbf{r}}{dt} + \frac{d\boldsymbol{\omega}}{dt} \times \mathbf{r} + \boldsymbol{\omega} \times \boldsymbol{\omega} \times \mathbf{r} \tag{3.2}$$

Eqn. 3.2 describes the kinematic vertical acceleration, $\frac{d^2\mathbf{r}}{dt^2}$, as well as the Eötvös correction described by Harlan, which is in the vertical components of the second and fourth terms [62]. The offlevel correction, c_{O} is required for misalignment of the gravimeter with the local vertical, which can cause aircraft motion to be mapped into

the gravity reading. The correction applied is given by Peters and Brozena as [53]:

$$c_{\mathrm{O}} = \sqrt{g_{\mathrm{loc}}^2 + (a_{x,\mathrm{meter}}^2 + a_{l,\mathrm{meter}}^2) - (a_{x,\mathrm{GPS}}^2 + a_{l,\mathrm{GPS}}^2)} - g_{\mathrm{loc}} \tag{3.3}$$

where g_{loc} is an approximate measure of the local gravity. The cross-track and along-track accelerations sensed by the gravimeter are $a_{x,\mathrm{meter}}^2$ and $a_{l,\mathrm{meter}}^2$. Those computed from differentiation of GPS positions are $a_{x,\mathrm{GPS}}^2$ and $a_{l,\mathrm{GPS}}^2$. The GPS positioning solution is used in the calculation of Eqns. 3.2 and 3.3. For the velocities and accelerations required in these calculations the GPS positions are differentiated and smoothed with a Chebyshev filter.

The drift and tie corrections are c_{drift}, and c_{tie}, respectively. The meter drift is computed by linearly interpolating between gravimeter readings when the aircraft is stationary at the same location before and after the flight. The tie value c_{tie} recorded with an absolute gravity meter at the exact spot the aircraft will be parked in prior to starting the flight. Next, Newton smooths the gravity profile using a Hanning window:

$$g_{FFG} = g_{ffg} * w_{Hanning}(t) \tag{3.4}$$

Final gravity profiles are subject to the choice of filter parameters used in the computation of the GPS trajectory and in the smoothing of the gravimeter output. NOAA NGS best-practices have determined that a Hanning filter length of 120 seconds produces optimal gravity profiles in spread and repeatability statistics. In this work, the Hanning filter length was varied from 15 seconds to 300 seconds, in increments of 15 seconds.

Airborne gravimetry depends heavily on low-pass filtering due to the high frequency noise of gravimeters and the long-wavelength nature of the gravity signal (see Childers, et al., [63], and Brozena, et al., [64]). The Newton software typically applies a 120-second Gaussian window low-pass filter three times to the full field gravity. This was changed to a Hanning window, shown in Fig. 3-6, because of its better cut-off characteristics compared to the Gaussian window. The power spectra of various smoothing windows are shown in Fig. 3-7. Here it can be seen that the $\times$3-Hanning

filter diminishes power for frequencies roughly 0.015 Hz lower than the Gaussian filter applied three times.

Figure 3-8 shows the progression from raw gravimeter output to the FFG for the third east-to-west ground track. The "raw" gravity in the top axes in Fig. 3-8(a) is the measured beam velocity from the gravimeter corrected for spring tension and cross coupling biases, converted to Gals. Accelerations calculated from differentiating the GPS positions are shown in Figs. 3-9(a) through (c). Accelerations measured with an IMU mounted to the gravimeter are shown in Figs. 3-9(d) and (e). GPS-derived and IMU accelerations are used to calculate the offlevel correction with Eqn. 3.3, which is shown in Figure 3-8(b). A magnification of the offlevel correction is shown in Fig. 3-10, because its magnitude is $\sim$ 3 orders of magnitude smaller than the other accelerations shown in Fig. 3-8. GPS measurements are also used in the calculation of the Eötvös correction, shown in Fig. 3-8(c). Fig. 3-8(d) shows the unfiltered FFG, which is the "raw" gravity with the Eötvös and offlevel corrections applied.

Finally, the unfiltered FFG is convolved with a 120-second Hanning window to produce the filtered FFG in the bottom axis of Fig. 3-8(e). It can be seen that the gravity signal becomes visible after filtering, but the degree to which gravimeter noise is smoothed is subject to the interpretation of what the gravity signal is for a given terrain. Childers et al. suggest that the smallest gravity signal sensed is $\sim$ 1.5 to 3$\times$ the aircraft altitude, depending on airspeed, turbulence, and variation in the actual gravity signal. In the case of this investigation the aircraft altitude is 6 km [63]. Since the aircraft is flying at 120 m/s, 100 seconds in Fig. 3-8 represents approximately 12 km. The RMS of the full field gravity with its mean removed is 1300 mGal, and 4 mGal after the Hanning window is applied three times. The effect of the low-pass filter on the gravimeter output is shown in Fig. 3-8. Here it can be seen that applying the filters more than once decreases the amplitude of the approximately 100-second oscillation in the gravity signal.

Figure 3-12 shows the effect the choice of the Hanning filter length used on the gravimeter measurements has on gravity profiles. The Hanning filter length must be chosen so that the noise from the gravimeter is minimized with respect to the actual

gravity signal, without smoothing out real variations in the gravity. Figure 3-13 shows the RMS of the repeat ground tracks in this study with respect to the mean ground track as the Hanning filter length is varied.

The choice of low-pass filter length must remove as much noise from the FFG while still allowing the gravity signal to be observed. In Fig. 3-13, it can be seen that at approximately 120 seconds, the RMS of the repeat ground tracks with respect to their mean has flattened, which suggests a low-pass window length of 120 seconds is possibly the shortest filter length before the gravimeter noise begins to dominate the solution.

The last step in the computation of the FAD profile is the subtraction of the normal gravity computed on a confocal ellipsoid which intersects the aircraft height:

$$g_{FAD} = g_{FFG} - \gamma_h \tag{3.5}$$

where γ_h is the normal gravity described in Pavlis et al., [52].

The process noise value used in the Kalman Filter applied to the ionosphere line-of-sight delay in the computation of GPS positions should be chosen based on the actual variation in the ionosphere from one measurement epoch to the next. The effect of the choice of process noise on the GPS height is shown in Fig. 3-15. Here it can be seen that the largest process noise value results in a position time history with the greatest short-term variation, and by using smaller values of process noise, the variations in the height time history become smoother. Choosing an optimal value for the process noise will result in an ionospheric model which correctly reflects the difference in ionospheric delays between the aircraft and base station receivers, while minimizing the amount of noise from the observables which eventually communicates through to the height time history. Subsequent examples of gravity profiles shown here were composted using a process noise of 1×10^{-3} TECU^2/s, and a Hanning filter length of 120 s.

The heights of the various GPS trajectories compared in the analysis of this work are shown in Fig. 3-14. Here the LC solution is the Track solution which treats the

ionosphere through the use of a linear combination of the phase observable. The L1L2 solution is that which utilizes the smoothed estimate of the line-of-sight ionospheric delay applied. The NGS trajectory is that computed by the NOAA NGS using both GPS and IMU data, and the "NGS NOIMU" solution is the NGS solution computed with only GPS data.

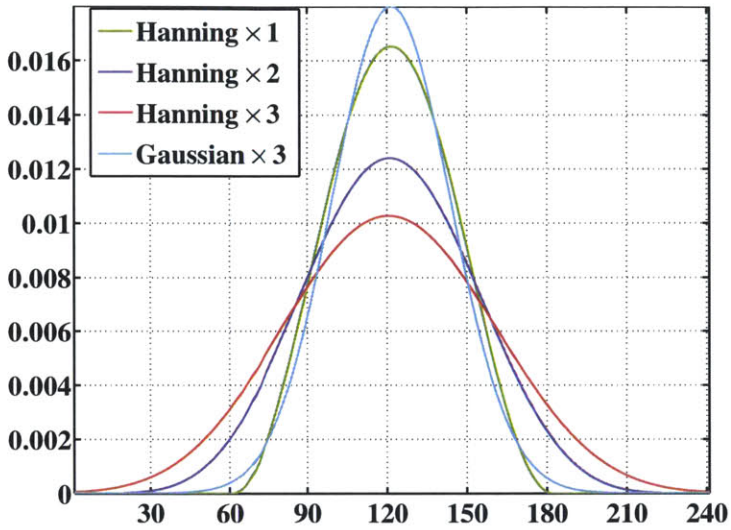

Figure 3-6: The 120-second Hanning window applied to the FFG. The shape of the Hanning window is shown here as if it were applied to the data once, twice and three times, as well as compared to a 120-second Gaussian window applied three times. The peak narrows and the tails diminish as the window is applied more than once.

3.6 Gravity Results

In Fig. 3-16, it can be seen that all four methods show the same general trend in free air disturbance from West to East, where the gravity signal increases from approximately -30 mGal and increases by approximately 20 mGal at an approximate longitude of 259.9 deg. The general trend of the gravity profiles agrees with the trend of the EGM08 field computed along these profiles, but the EGM08 profiles are 3-7 mGal less in magnitude than the measured gravity profiles.

In Figure 3-16, there are four profiles plotted for EGM08, which is indicative of the aircraft flying a slightly different latitude for each profile. The maximum cross-track

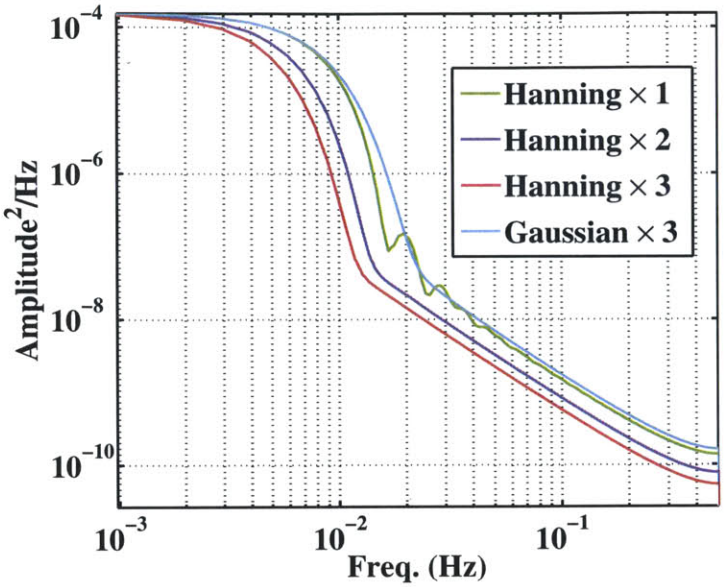

Figure 3-7: The power spectra of the Hanning window applied once, twice and three times, as well as the Gaussian window applied three times. Here it can be seen that the Hanning window diminished power for the frequencies above 40 Hz, and the Gaussian window's slope shallows around 100 Hz.

difference between the profiles was 100 m. The mean gravity profile for each of the LC, L1L2, NGS GPS-INS and NGS GPS-only trajectories is shown in Fig. 3-17. The profiles were corrected to a mean latitude, which are shown in Figs. 3-18 and 3-19. The residuals of the four west-east spans with respect to the mean profiles are shown in Figs. 3-20 and 3-21, with their RMS values. Here it can be seen that maximum differences of all four spans with their respective mean are about 6 mGal. The RMS of these differences for each profile are shown in Table 3.1.

When filtering the ionosphere with a process noise of 1×10^{-3} TECU^2/s, and, when using a Hanning filter length of 120 seconds, RMS difference from the LC solution is 0.6 mGal. The RMS difference of the L1L2 solution with the NGS solution is 0.43 mGal when GPS and inertial measurements are used, and the RMS difference with the NGS GPS-only solution is 0.45 mGal. The differences of the individual profiles shown in Fig. 3-20 with the mean profile calculated with the LC solution are shown in Fig. 3-22, where it can be seen that the four mean profiles differ from one another on the order of 0.5 mGal.

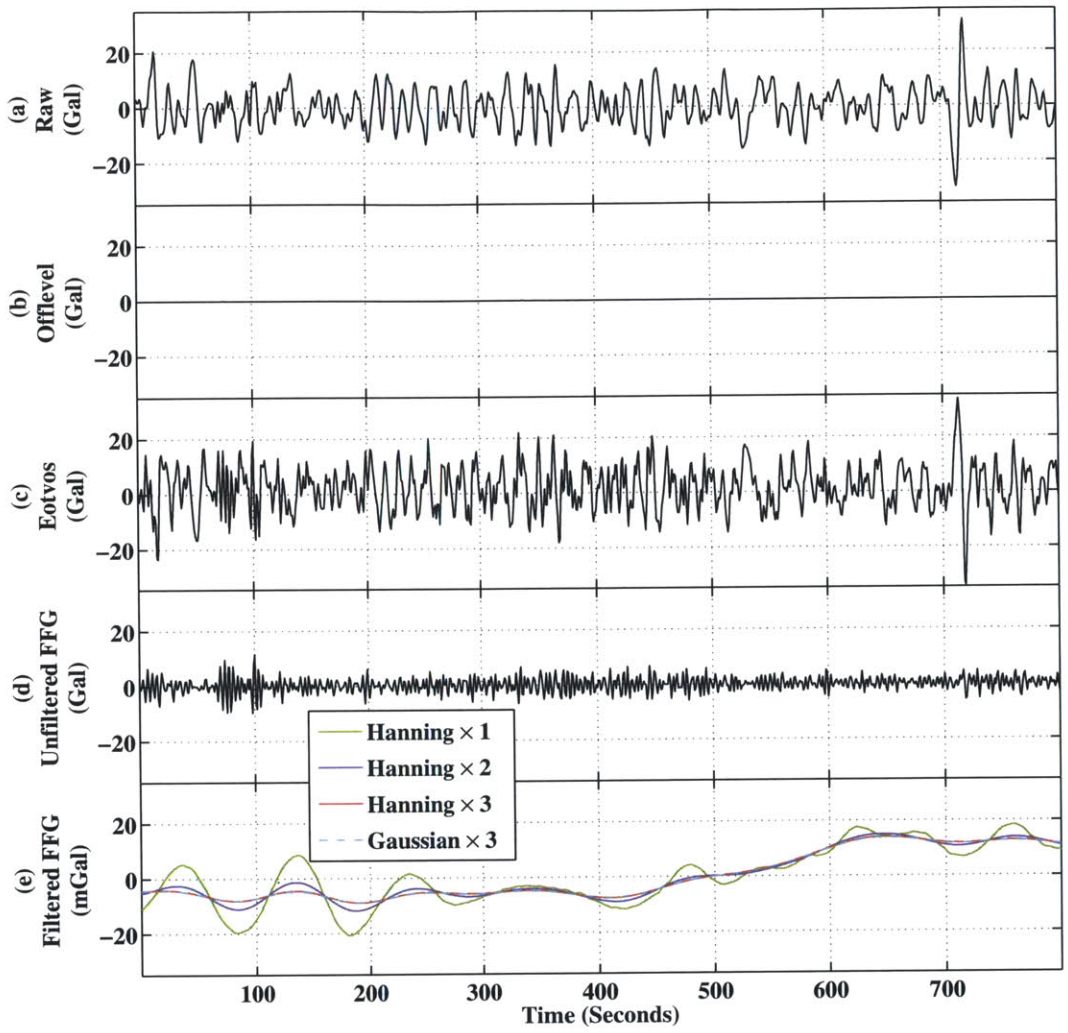

Figure 3-8: Steps in the process of calculating the filtered FFG. Axis (b) shows an example of raw gravimeter data corrected for spring constant and cross correlation biases in the upper axis. Axis (b) shows the offlevel correction which accounts for the misalignment of the gravimeter with the local vertical, calculated with Eq. 3.3. The offlevel correction is on the order of ~ 3 orders of magnitude smaller than the other accelerations shown here, and a magnification is shown in Fig. 3-10. Axis (c) shows this Eötvös correction. The unfiltered full field gravity is plotted on axis (d); this quantity is the raw gravity with the Eötvös and offlevel corrections applied. The 120 second-filtered full field gravity is plotted on axis (e), with the mean of 9.78663×10^5 mGal removed.

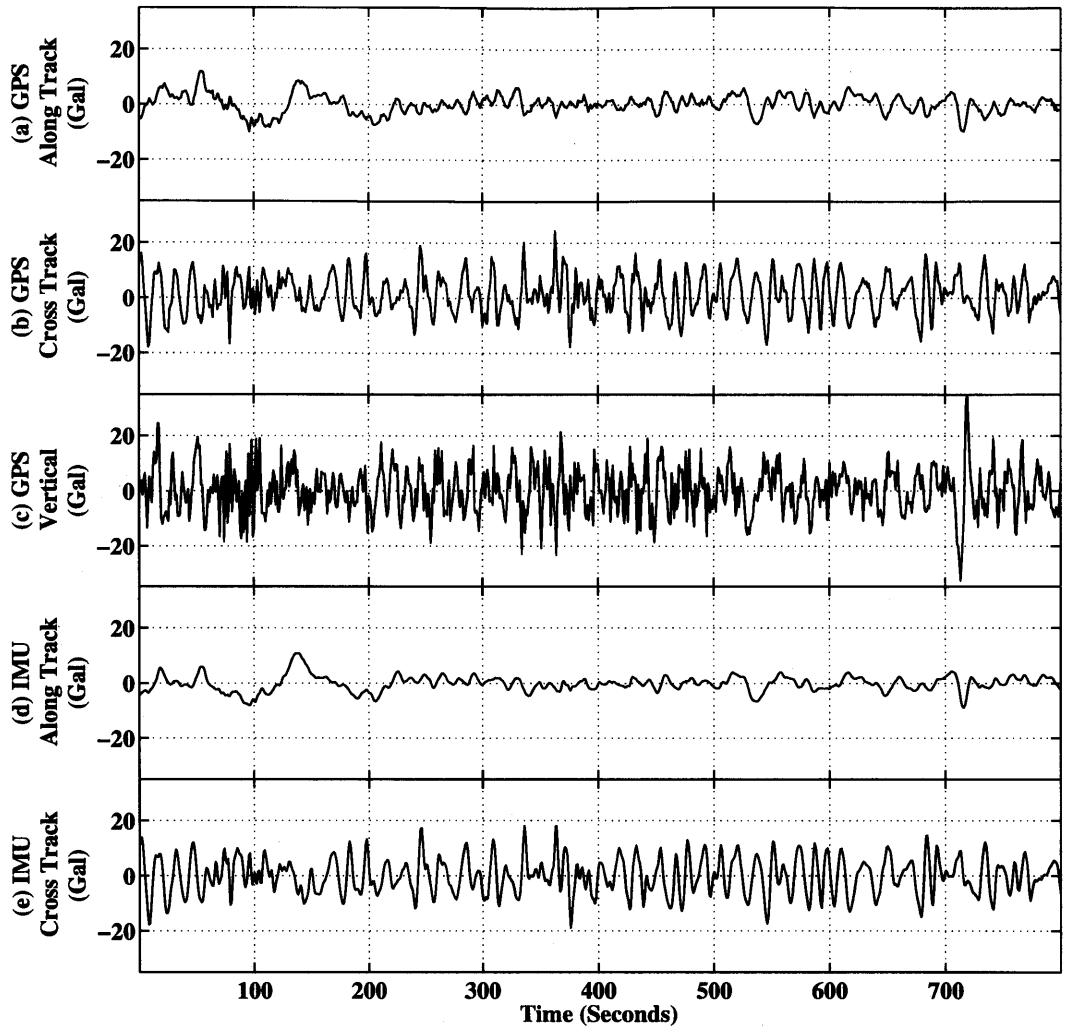

Figure 3-9: Accelerations calculated form GPS positions and observed with IMU measurements. Axes (a) through (c) are the GPS along-track, cross-track and vertical accelerations. Axes (d) and (e) are the along-track and cross-track accelerations measured with an IMU mounted on the gravimeter platform.

The mean of the difference between each east-west profile and the EGM08 field calculated along each profile is shown in Table 3.2. These differences range from 3 to 7 mGal, and the differences among the four GPS trajectories' results vary from one another by approximately of 0.01 to 0.1 mGal. There is a much starker contrast between profiles 1 and 2 and profiles 3 and 4. Profiles 1 and 2 differ with EGM08 by

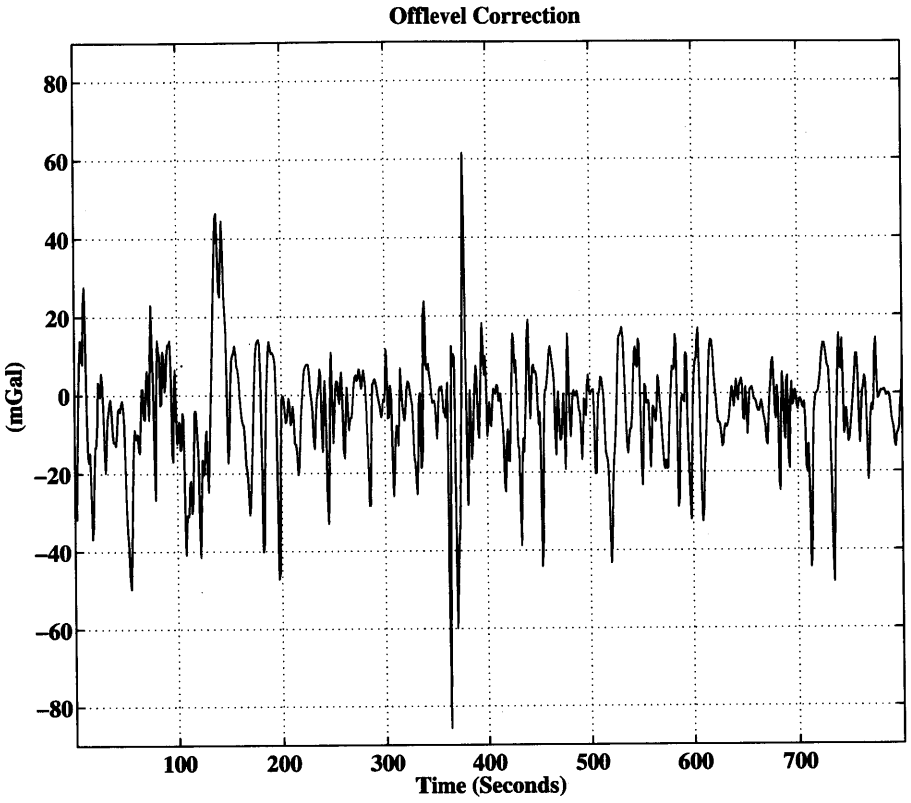

Figure 3-10: The offlevel correction computed using equation 3.3, and the GPS and IMU accelerations shown in Fig. 3-9, which calculates the misalignment of the gravimeter measurement with the local vertical.

3-4 mGal, and profiles 3 and 4 differ from EGM08 by 6-7 mGal. These are on the order of the error of the EGM08 field for this region [52].

There are several possible causes for the difference between the EGM08 field and the gravity profiles computed here. EGM08 is the product of the synthesis of a variety of data types from spacecraft orbits, airborne gravity, altimetry, and terrestrial and oceanic surveys. Also EGM08 has a block size of 9 km at the equator (see Pavlis et al., [52]). While Fig. 3-16 shows that the gravity profiles computed with Newton are internally consistent with one another, and their residual RMS with respect to the mean of the four profiles is 2-3 mGal, there still could be inaccuracies in the estimation of the gravimeter still readings, and drift rate. On the other hand, if this is a region where EGM08 data coverage was more sparse than the data in this survey, the aircraft in this survey could have recorded more signal than is present in EGM08.

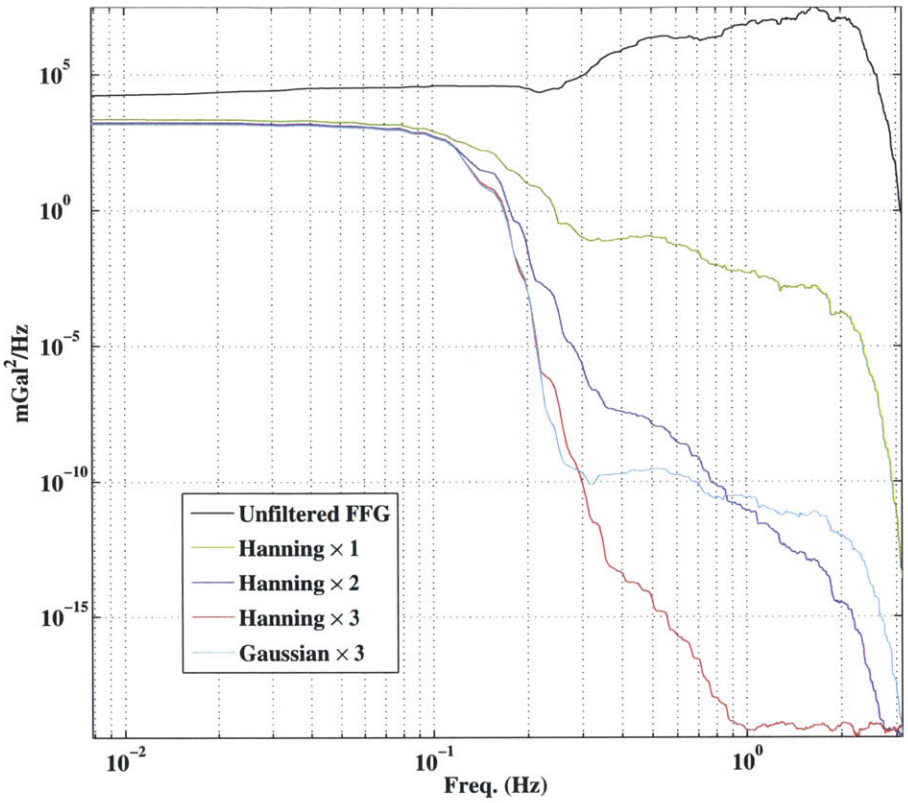

Figure 3-11: The power spectra of the unfiltered and filtered full field gravity profiles shown in Fig. 3-8. The black spectrum shows the highest power as it was computed from the unfiltered FFG. The red spectrum was computed from the full field gravity after a 120 second Hanning window was applied three times.

Next performance was mapped over a span of ionosphere Kalman filter process noise values and the Newton software's Hanning filter length values. Figure 3-23 is a contour plot of the RMS difference between the LC and L1L2 solutions between the RMS values of the four gravity profiles with their respective mean. In this representation, it can be seen that a local minimum occurs at approximately 1×10^{-3} TECU^2/s and a Hanning filter length of 120 seconds, and is marked by a white dot in Fig. 3-23. In this region the gravity profiles computed with L1L2 solution with the ionospheric model applied has a lower total RMS than the gravity profiles computed with the LC solution. It can also be seen that a trough exists for Hanning filter lengths from 90-300 seconds between approximately 1×10^{-4} TECU^2/s and 1 TECU^2/s. Although the trough extends through very long Hanning filter lengths (up to 300 seconds), the

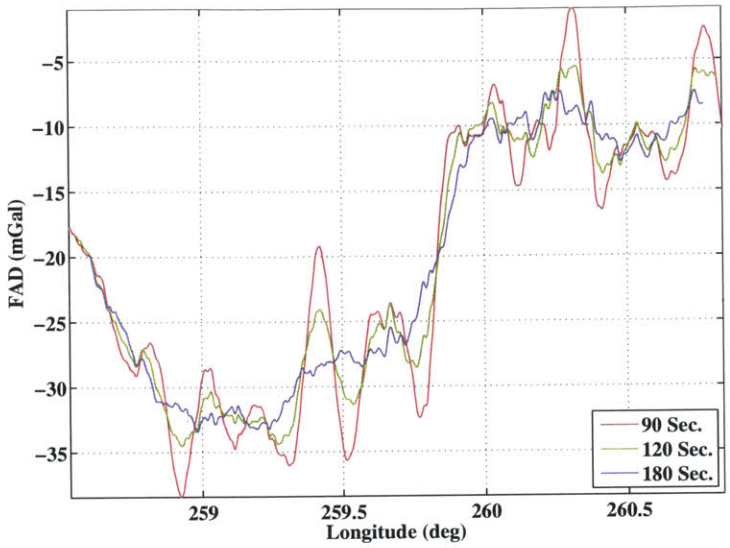

Figure 3-12: Free air disturbance computed using various filter lengths on the gravimeter output.

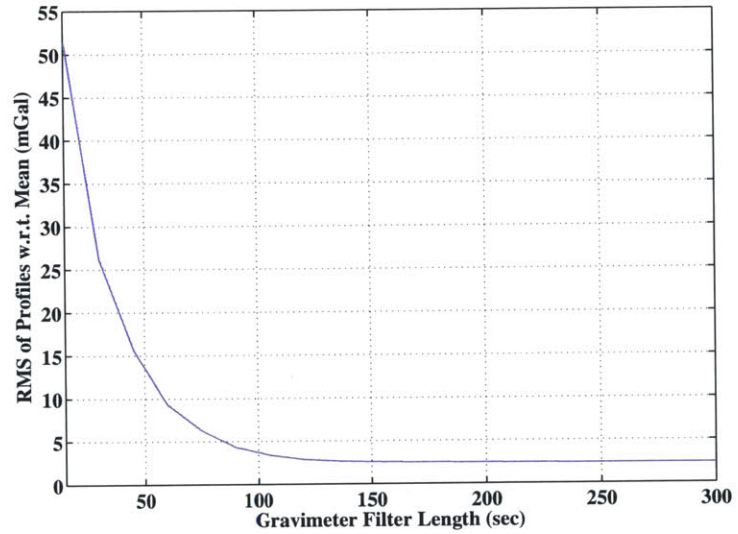

Figure 3-13: Variation of the RMS of the four gravity profiles with respect to their mean as the Hanning filter length is changed.

use of such long filter lengths removes much of the gravity signal. Although Fig. 3-23 shows a lower RMS of the solution in which the ionosphere was applied for these lengths, it is not necessarily indicative of a useable gravity solution for *both* the ionospheric model solution or the standard linear combination (LC) solution. A metric was added to redden the short Hanning filter length portion of the plot because even

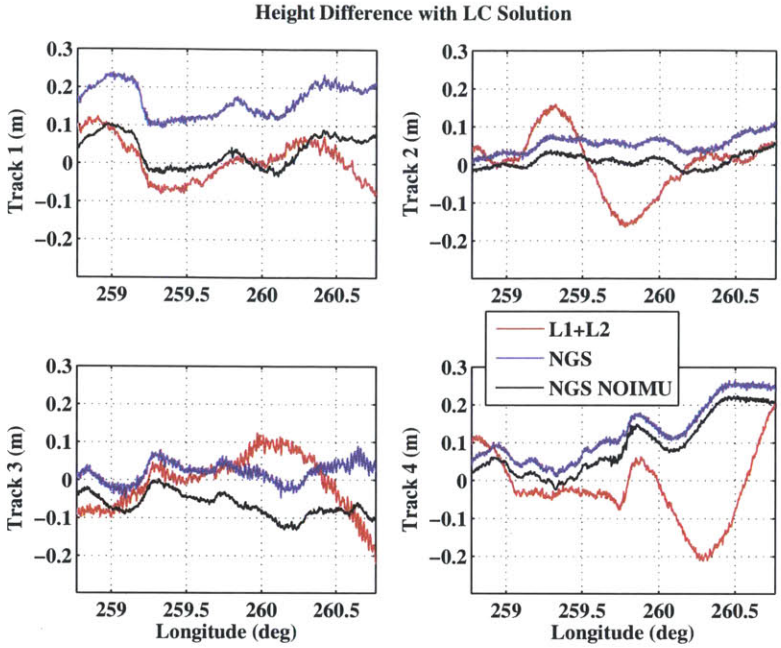

Figure 3-14: Differences in height with the LC solution heights. Red is the difference of the L1L2 heights with the LC heights. Blue shows the NOAA NGS NGS solution differences, which makes use of both GPS and IMU data. Here the LC solution is the Track solution which treats the ionosphere through the use of a linear combination of the phase observable. The L1L2 solution is that which utilizes the smoothed estimate of the line-of-sight ionospheric delay applied. The NGS trajectory is that computed by the NOAA NGS using both GPS and IMU data, and the "NGS NOIMU" solution is the NGS solution computed with only GPS data.

though the L1L2 solution has a lower RMS in this region, the gravity profile itself is not useful, since the total RMS is large (refer to Fig. 3-13).

The contour plots shown in Figs. 3-24 and 3-25 show the RMS difference comparing the gravity computed using the L1L2 trajectory to those computed using the NGS software. Fig. 3-24 is comparing the L1L2 solution to the NGS solution which makes use of both GPS and IMU data, and Fig. 3-25 compares L1L2 to the NGS solution that uses only GPS data. The contribution of the increasing RMS due to short Hanning filter lengths is represented here by the vertical red region on the left side of the plot.

In Figs.3-24 it can be seen that the L1L2 solution has a lower RMS than the NGS GPS-INS solution for Hanning filter lengths less than 100 seconds. There is a

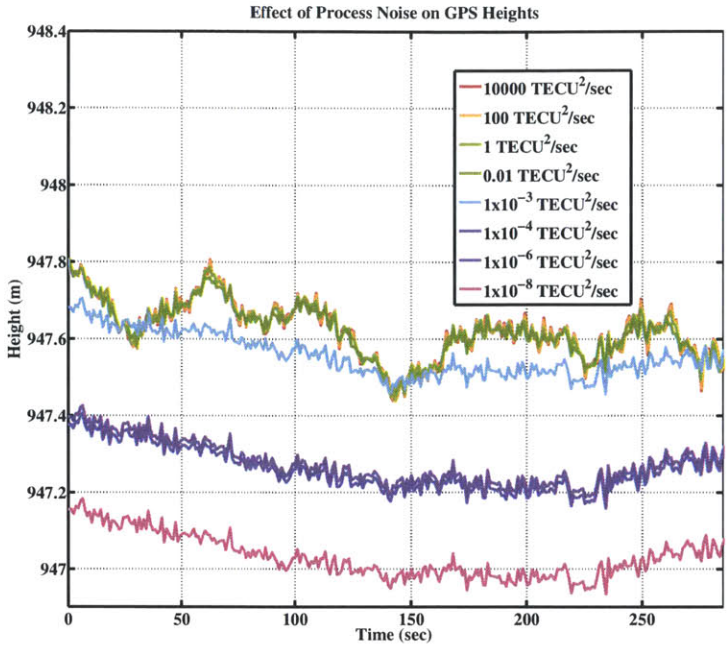

Figure 3-15: Effect of choice of Kalman filter process noise on the smoothness of GPS-computed heights in Track software for the stationary portion of the flight before the aircraft began its taxi.

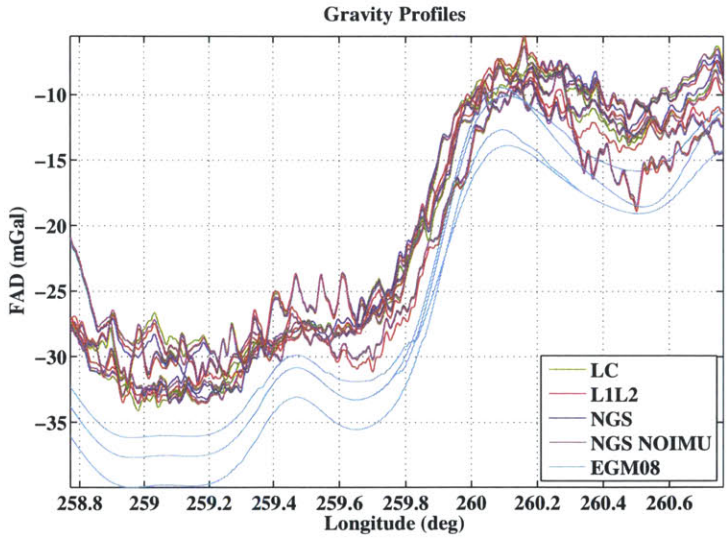

Figure 3-16: Free air disturbance profiles for various GPS processing techniques.

slight deviation from this for ionosphere filter process noise values between 1×10^{-4} TECU$^2/s$ and 0.1 TECU$^2/s$, in which longer Hanning window lengths will still result in a lower repeat RMS with the Track L1L2 solution than with the NGS GPS-INS

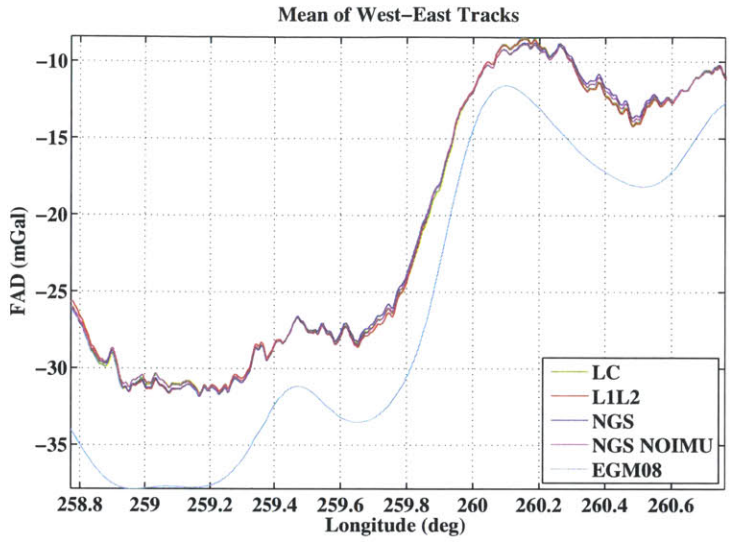

Figure 3-17: Mean of FAD profiles for various GPS processing techniques.

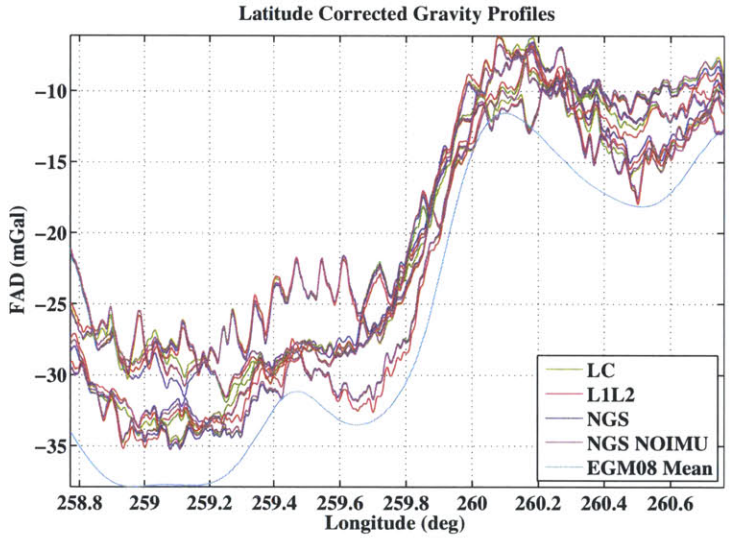

Figure 3-18: Latitude-corrected FAD profiles. The single EGM08 profile here is the mean of the EGM08 profiles in Fig. 3-16. The profiles for the various other processing techniques were corrected to this latitude.

solution. In Fig. 3-25, it can be that the Track L1L2 solution has a lower RMS than the NGS GPS-only for a much larger span of Hanning window lengths and ionosphere filter process noise values. A similar trough to that shown in Fig. 3-23 appears.

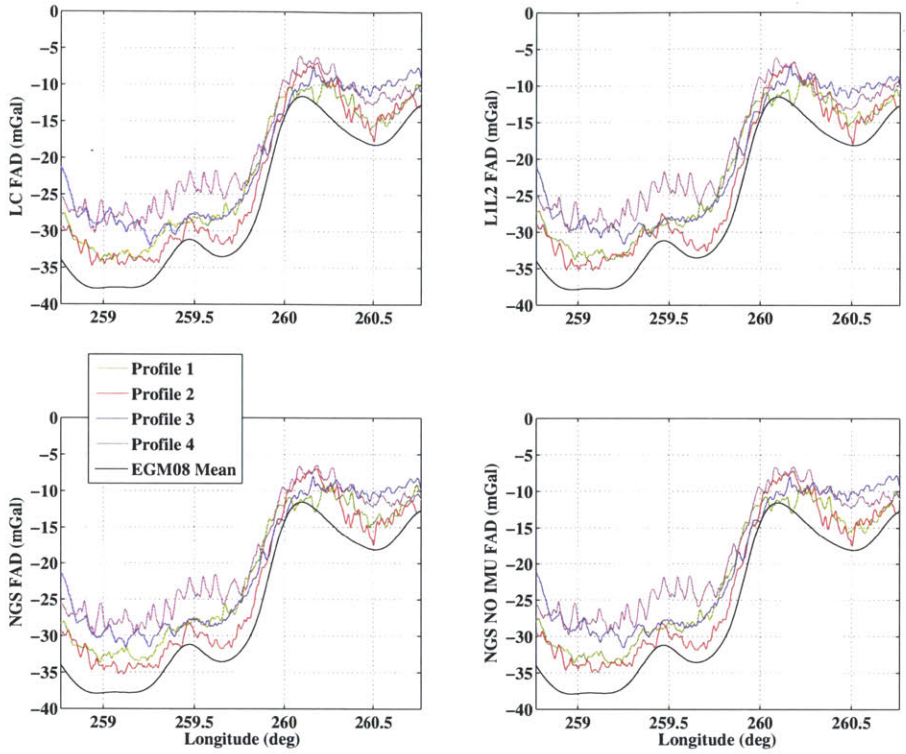

Figure 3-19: Latitude-corrected FAD profiles. The single EGM08 profile here is the mean of the EGM08 profiles in Fig. 3-16, and is the same in all four axes.

3.7 Conclusions

The technique of computing and smoothing an ionospheric model, and applying it to GPS data in a double-differencing scenario can improve the trajectory computed by improving its noise characteristics. This is a useful technique as long as the level of filtering applied to the ionospheric model is judiciously chosen to remove measurement noise caused by the GPS phase observables, but does not remove actual ionospheric variations. It was for this reason that a range of process noise values was explored for this research. In some cases, the application of the ionospheric model resulted in gravity profiles which had a smaller residual RMS than traditional double-differencing and NGS techniques. Conversely, there are combinations of ionospheric and gravity smoothing parameters which resulted in the technique performing worse than others,

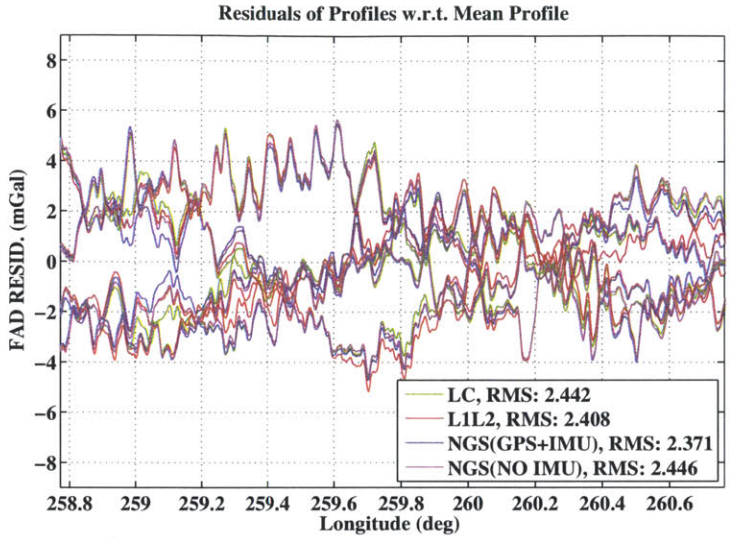

Figure 3-20: Plot of residuals of FAD profiles with respect to the mean profile for all four GPS trajectories.

Run	Profile 1 West to East	Profile 2 East to West	Profile 3 West to East	Profile 4 East to West
LC	2.20	2.78	2.10	2.71
L1L2	2.09	2.83	1.95	2.65
NGS	2.12	2.89	1.92	2.68
NGS NO IMU	2.17	2.83	2.05	2.71

Table 3.1: The RMS of the difference between each gravity profile and the mean profile computed using the LC, L1L2, and NGS trajectories.

or which produce lower-quality gravity results.

The span of process noise for which the application of the ionospheric modeling technique appears most useful is for process noise values between approximately 1×10^{-3} TECU^2/s and 1 TECU^2/s, with a gravity filter length between 90 and 120 seconds. This region in Fig. 3-24 suggests that with this choice of parameters, using a smoothed ionospheric model can have the greatest effect to produce gravity profiles which are the most self-consistent. For ionospheric filter process noise values smaller than 1×10^{-3} TECU^2/s, actual ionospheric variation may be smoothed through, which could be the reason for the increased RMS in that region, resulting in gravity profiles which are less self-consistent. When the process noise value is larger than 1 TECU^2/s, more noise from the GPS phase observables is allowed into the computation of the

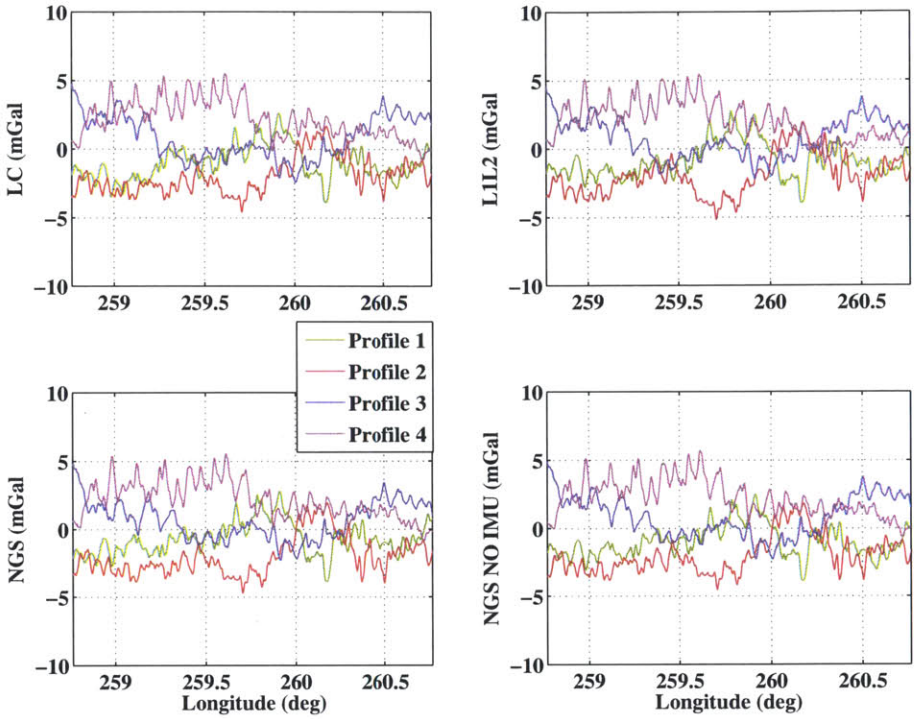

Figure 3-21: Plot of residuals of FAD profiles with respect to the mean profile for all four GPS trajectories, split on four axes for each of the GPS processing methods.

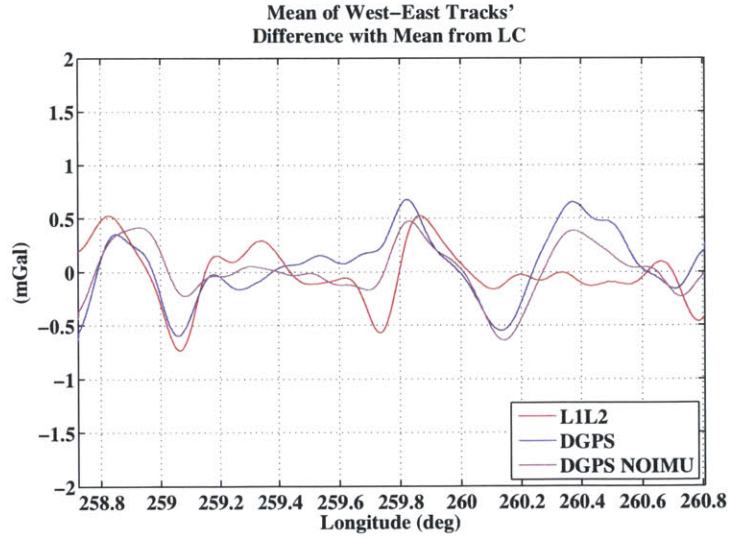

Figure 3-22: Mean of profiles differenced with the mean LC profile.

Run	Profile 1 West to East	Profile 2 East to West	Profile 3 West to East	Profile 4 East to West
LC	4.14	3.00	6.07	6.99
L1L2	4.25	2.99	5.98	6.92
NGS	4.46	2.99	5.98	7.01
NGS NO IMU	4.18	2.99	6.06	7.04

Table 3.2: Mean differences between each processing method's FAD the EGM08 field for each profile.

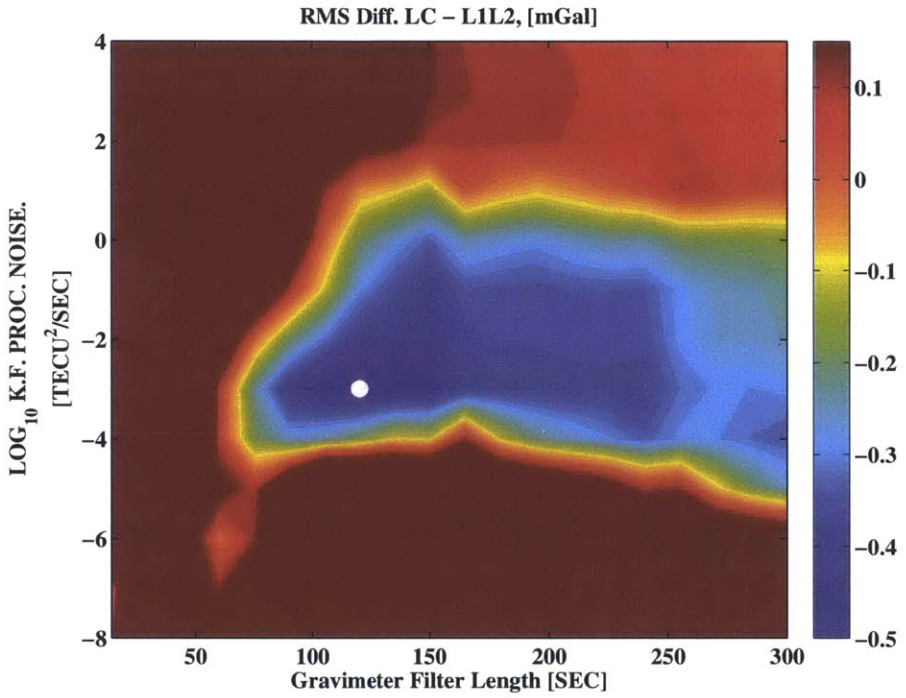

Figure 3-23: Free air disturbance RMS difference between the LC and L1L2 solutions computed using various filter lengths and ionosphere filter process noise values, with a metric added for short Hanning filter lengths. Red areas indicate process noise and Hanning filter length combinations which result in the LC solution having a lower RMS than the L1L2 solution. Blue regions are where the L1L2 solution has a lower RMS. A metric was added to redden the short Hanning filter length portion of the plot because even though the L1L2 solution has a lower RMS in this region, the gravity profile itself is not useful, since the total RMS is large (refer to Fig. 3-13). The minimum of this contour map is marked by a white dot at a Hanning window length of 120 seconds, and a inonsphere filter process noise of 1×10^{-3} TECU^2/s.

GPS trajectory, which in turn can result in less-reliable gravity. For the span of

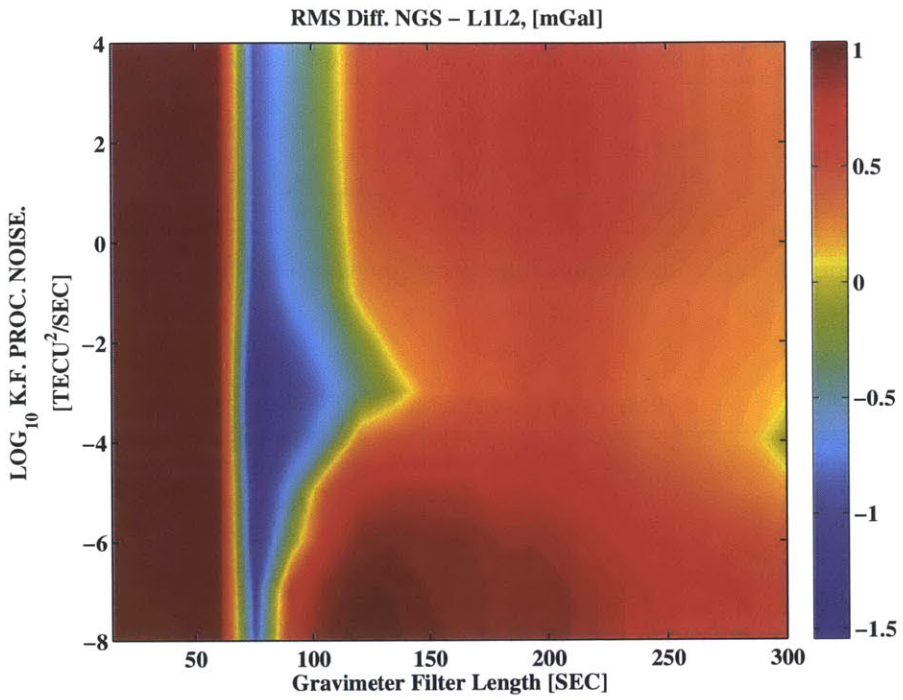

Figure 3-24: Free air disturbance RMS difference between the NGS GPS-INS solution and the L1L2 solution.

Hanning filter lengths between 30-75 seconds, the residual RMS is very high (shown in Fig. 3-13), due to the large RMS of repeat gravity profiles compared in that region. When the gravity filter length is longer than 150 seconds, we see no improvement in residual RMS, and are likely filtering through gravity signal. The optimal selection of process noise and Hanning filter length investigated here was 1×10^{-3} TECU^2/s and 120 seconds, which resulted in the L1L2 solution having RMS difference of 0.6 mGal with the LC solution.

The region for which the ionospheric technique had a lower gravity profile residual RMS than previous techniques is also indicative of the ionospheric variations observed by the GPS receivers, and possibly the effect of using GPS data from an aircraft over long baselines. The "optimal" performance regions shown in the contour plots above will likely not be the same across all investigations. Local ionospheric variations, as well as differences in equipment and the data rate of the GPS receivers can cause the

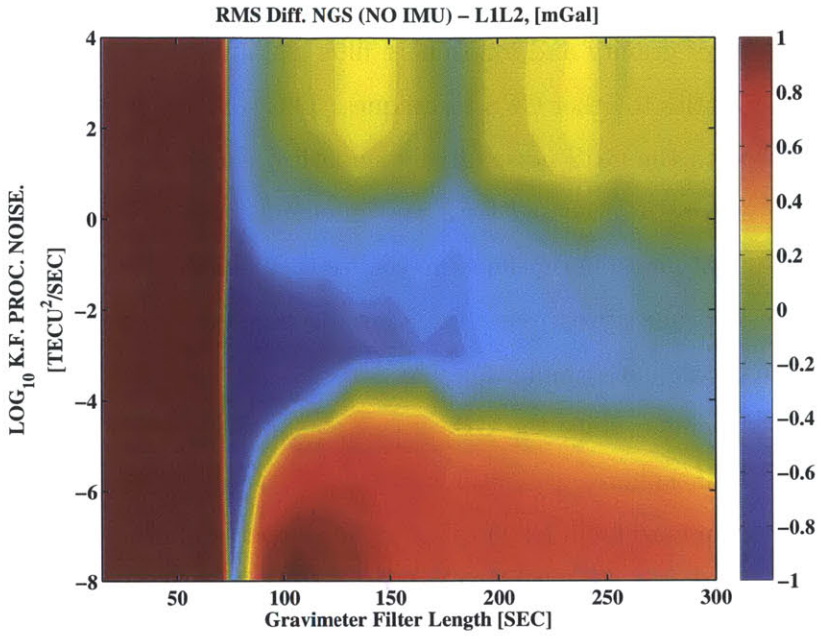

Figure 3-25: Free air disturbance RMS difference the NGS solution (using only GPS data) and the L1L2 solution.

need for a different selection of process noise. For this reason, it is recommended that a similar investigation of various levels of process noise and Hanning filter length be conducted if this technique is to be applied in the future.

The gravity repeatability was examined over a wide range of filter settings. In this process, we were able to arrive at a Hanning window length and Kalman filter process noise which produced a maximum RMS improvement when comparing the Track L1L2 to the Track LC gravity solutions. Operators may not always have the luxury of repeat tracks to arrive at an optimal choice of filter parameters, however. One way to help quantify the magnitude of the Kalman filter process noise is by examining the spectra of the GPS phase observables for the frequency at which noise dominates, as is shown in Fig. 3-2. In terms of setting the Hanning window filter length, the metric given by Childers et al. provides a starting point: that the shortest observable gravity wavelength is given by the height of the aircraft [63].

The application of a smoothed ionospheric model to GPS phase observables here has produced a lower residual RMS for repeat-profile measurement for this aircraft

configuration and geographic area. A local minimum of optimal performance with respect to the choice of gravity and ionosphere filter parameters was observed when comparing RMS statistics to other GPS techniques. This could indicate that using an ionospheric model with the GPS noise largely smoothed could have a positive effect on future gravity surveys. Increased GPS and gravimeter sensitivity could rely on the correct modeling of ionospheric effects to realize their full benefit. In addition, as the NOAA GRAV-D project progresses, the ionospheric conditions will become more quiescent as we approach solar minimum. As a result the technique presented here will be of increased benefit, since the GPS phase noise will be easier to isolate from the variation in the ionosphere.

Additional steps forward include: 1) the study of the performance of this technique at the polar and equatorial latitudes. 2) analysis of the ionospheric model through solar maximum. 3) the combination of IMU and GPS data with an ionospheric model applied to realize the full benefit of instrumentation and technique. 4) the study of this technique applied to various aircraft configurations (different airframes, altitudes, and airspeeds). Table 3.3 details some other aircraft used by NOAA for the collection of GRAV-D data.

Table 3.3: Platforms used for airborne gravimetry by NOAA for the GRAV-D project.

Aircraft	Cessna Citation	Cessna 208	Lockheed P-3 Orion	Aero Turbo Commander
Altitude (m)	11000	1000	2500	<5000
Speed (m/s)	145	75	211	91
Mass (kg)	4000-6600	4000	51000-61000	3000
GPS rate (Hz)	1	10	2	1
Along-Track Horiz. Resolution (m)	600	320	400	360

Chapter 4

Orbit Determination of the Dawn Spacecraft with Image Constraints using GEODYN

4.1 Abstract

The orbit of the Dawn spacecraft around asteroid 4 Vesta has been reconstructed using radiometric measurements and image constraints using NASA GSFC's GEODYN software. Image constraints are introduced as a new measurement type for GEODYN because they constrain the orbit in the along- and cross-track directions, while radiometric measurements provide a stronger constraint in the radial direction. High-quality orbit knowledge for interplanetary spacecraft is required for geophysical analysis and geographical registration of data. Image constraints are available whenever two image footprints on the surface overlap. The measurement uncertainty of images is limited by pixel scale, which in the case of the Dawn mission, ranges from 50 m/pixel to 150 m/pixel. The image constraint residual RMS is less than 0.5 pixels for all mission phases. Radiometric residual RMS spanned 0.07 - 0.44 mm/s for Doppler, and 0.7 - 1.5 m for range measurements. Radiometric and image constraint residual RMS values are comparable to those reported by the Dawn Science Team. Improve-

ments as a result of using image constraints are largest in the along- and cross-track directions during the Survey phase of the mission during this period. Agreement between our orbit reconstruction and the trajectory archived by the Dawn Gravity Science Team improves from several kilometers with radiometric measurements only to hundreds of meters when image constraints are included.

4.2 Introduction

Planetary missions rely on high-quality orbit knowledge of spacecraft for reference frame definition, geophysical analyses, and the registration of geographical datasets to the surface of the body being studied. Spacecraft trajectories are utilized to determine the center of mass and moments of inertia of the body, which are used to define the pole and reference frame used to register datasets to the surface. As such, improvements in orbit quality can benefit the science derived from high-resolution datasets. Also, precise spacecraft trajectories can be considered a scientific product themselves, since they are needed to estimate the gravity field, which yields insight into the internal structure, which bears on the formation and evolution of the body (see Ermakov et al. [65]).

Precision orbit determination (POD) is typically carried out using radiometric Doppler and range measurements, which can only be acquired when the spacecraft is visible from ground tracking stations. Radiometric measurements are also subject to the scheduling of availability of the Deep Space Network (DSN) or other tracking stations, which typically support many missions simultaneously. Orbits computed using radiometric Doppler and range observations have the lowest position uncertainty in the radial orbit component, while the uncertainty associated with the along- and cross-track components is typically an order of magnitude greater (see Mazarico et al. [66]).

Use of additional orbit constraints can improve the solution accuracy in ways that complement radiometric measurements. Examples of measurements used in addition to radiometric Doppler and range are laser altimetric crossovers, Earth-to-spacecraft

laser ranging, GPS position updates, spacecraft-to-spacecraft ranging, and optical observation from ground-based telescopes. Laser altimetry crossovers have been used on the Mars Global Surveyor (MGS), and the Lunar Reconnaissance Orbiter (LRO) missions at the Mars and the Moon, respectively (see Mazarico et al. [67], Rowlands et al. [68], and Lemoine et al. [69]). Crossovers occur most often at high latitudes for spacecraft in polar orbits, and constrain the orbits mostly in the radial and cross-track directions. Another example of how standard DSN measurements can be complemented was with the use of radiometric range-rate measurements between two spacecraft in formation. The technique of measuring the range and range rate between two spacecraft to improve orbit determination was used on the GRACE, SELENE, and GRAIL missions at Earth and the Moon (see Tapley et al. [70], Goosens et al. [71], and Zuber et al. [72]). GRACE utilized spacecraft-to-spacecraft measurements in Earth orbit and was able to measure seasonal and tidal gravitational variations. For SELENE and GRAIL this technique was crucial because direct ground-based radiometric measurements can never be acquired on the lunar farside due to the Moon's synchronous rotation.

Optical orbit determination methods can be characterized in terms of passive and active techniques. Passive techniques involve the optical observation of non-cooperative objects in space, such as small asteroids or space debris. These orbit determination (OD) techniques rely on the measurement of the azimuth and elevation of an object from the point of view of a ground based telescope, along with the variation of magnitude of light reflected from the object (see Bloch et al. [73], and DeMars et al. [74]). "Active orbit determination" refers to OD using cooperative spacecraft, such as those specially designed for ground-based tracking or those which can be commanded from the ground to return data relevant to orbit determination. These techniques include ranging with ground-based lasers to a spacecraft, or when a spacecraft is commanded to collect optical data such as images or laser ranging data. Active laser ranging methods include laser ranging from a ground station on Earth to spacecraft orbiting Earth, as was demonstrated with the LAGEOS spacecraft (see Bianco et al. [75]), and a technique that has been developed with the LRO spacecraft

orbiting the Moon (see Zuber et al. [76]). While this approach cannot be used when LRO orbits above the lunar farside, orbit determination with Earth-based lasers can provide tracking when radiometric tracking stations are unavailable.

Images from spacecraft have been used to improve orbit knowledge on the Near Earth Asteroid Rendezvous (NEAR) and Hayabusa missions, among others (see Konopliv et al. [77], and Gaskell et al. [78]). These constraints are critical in weak, non-uniform gravity environments. For this reason, image constraints were planned to be used along with radiometric observations as part of the orbit determination effort with Dawn (see Raymond et al. [79], and Konopliv et al. [80]). When of sufficient quality, the orbital constraints from images are important for interplanetary missions on which radiometric tracking is intermittent, and the magnitude of the radiometric noise varies. They also aid in the estimation of non-conservative forces such as solar radiation pressure, which can be a dominant error source for missions to small bodies such as Ceres and Vesta. The effect of solar radiation pressure on the Dawn spacecraft is substantial because of the low mass-to-area ratio of the spacecraft; as detailed by Thomas et al. [81], over 70% of the surface area of the spacecraft is contributed by the 19.7-m-long solar array span.

The use of image constraints is applicable for spacecraft that have cameras that can offer a pixel scale on the surface of the planetary body comparable to or better than the level of uncertainty of other measurements useful for OD. In addition to Dawn, these include spacecraft such as the Mars Reconnaissance Orbiter (MRO), LRO, NEAR, Hayabusa, and the Origins Spectral Interpretation Resource Identification Security Regolith Explorer (OSIRIS-REx) (see Table 4.1). The pixel scale varies with the spacecraft altitude and velocity with respect to the planetary body. This technique has been employed on the NEAR and Dawn missions, but was carried out with MIRAGE, the orbit determination software of JPL (see Moyer [16] and Konopliv [14]).

This work describes the first use of image constraints for orbit determination with the GEODYN II software (see Pavlis, et al. [10]). GEODYN is the orbit determination and geodetic parameter estimation software of NASA Goddard Space flight Cen-

Spacecraft	Target Body (approximate radii)	Imaging Instrument	Pixel Scale (m/pixel)
MRO	Mars (3400 km)	Height Resolution Imaging Science Experiment (HiRISE)	0.5 [82]
LRO	Moon (1737 km)	Lunar Reconnaissance Oribter Camera (LROC)	0.5 [83]
OSIRIS-REx	101955 Bennu (266 m)	OSIRIS-REx Camera Suite (OCAMS)	0.25 [84]
Hayabusa	Itokawa (260 m)	Asteroid Multiband Imaging Camera (AMICA)	0.1-2 [85]
NEAR	433 Eros (16 km)	Multispectral Imager	6 [78]
Dawn	Vesta (265 km) and Ceres (460 km)	Framing Cameras	50-150

Table 4.1: Spacecraft for which orbit determination using image data could be or has been utilized.

ter and is maintained by Stinger Ghaffarian Technologies, Inc. GEODYN iteratively integrates the trajectory of a spacecraft and fits estimated parameters to minimize the residuals between computed and measured observations. The orbit integrator uses Cowell's method, which was first documented by Cowell and Crommelin to predict the orbit of Halley's Comet [15], and is described by Brouwer and Clemence [86]. The effects of the gravitation of the Earth, Moon, Sun and planets, solar radiation pressure, and, when applicable, tidal gravitation and atmospheric drag are modeled by GEODYN. Relativistic corrections on time and range delays are also included, and are detailed by Moyer in [87] and [88]. A Bayesian least squares approach is used to incorporate various measurement types into the orbit solution. Recent missions for which GEODYN was used for orbit determination and geodesy are GRAIL [89], LRO [67], MRO [90] and MESSENGER [91].

In this paper, we define the new image constraint measurement type, describe the orbit determination methodology as applied to the Dawn spacecraft at asteroid 4 Vesta, and, finally quantify and analyze the performance of our new optical technique.

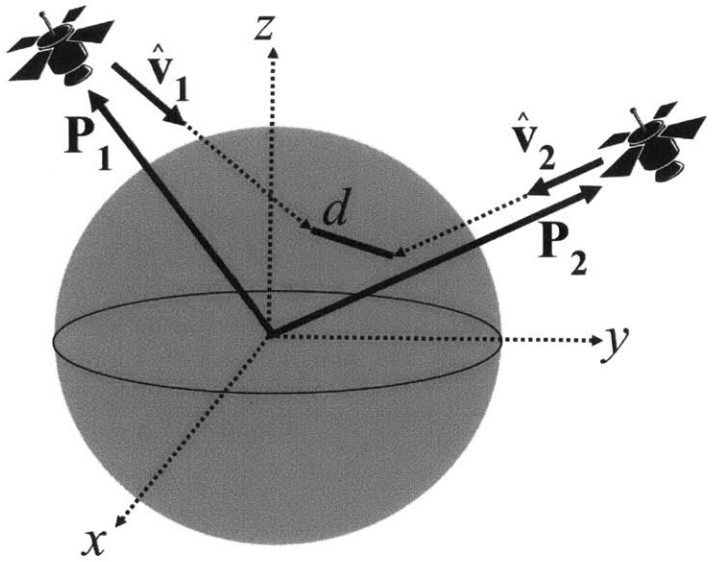

Figure 4-1: Schematic of the vectors used to define the image constraint.

4.3 Image Constraint Definition

The landmark data used in this work are a byproduct of the stereo-photoclinometry (SPC) work performed by Robert Gaskell at the Planetary Science Institute to create the Vesta shape model [92]. Repeatedly-imaged surface features are identified in the available images and measured in terms of pixel locations. The observation geometry is then used to constrain their 3-dimensional position. The measured line/sample values are the landmark data used for orbit determination by the Dawn Science Team (see Konopliv, et al. [14]), whereby the misfits with the computed values given the modeled trajectory are minimized. This landmark data type relies on a good *a priori* shape model, because the spacecraft trajectory will be modified so that the pixel locations match the pixel measurements, which are not dependent on the orbit, landmark position, or camera pointing errors. On the other hand, the image constraints are a differential measurement type, and are largely insensitive to errors in planetary orientation model and landmark position. They can thus be well-adapted to early mission operations. The image constraint inputs to GEODYN are the pixel coordinates of selected landmarks identified in image pairs. Figure 4-2 shows an example of two Dawn Framing Camera images that have overlapping footprints.

Figure 4-2: Excerpts from Dawn Framing Camera images FC21A0024464 (left) and FC21A0026765 (right), which have overlapping footprints. The images were acquired on 4 Apr 2012 22:13:43.414 UTC and 26 April 2012 23:14:21.595 UTC, and their resolutions are 21 m/pixel and 22 m/pixel respectively. The spacecraft altitude was 227 km and 233 km, respectively.

The unit vector pointing from the spacecraft to the landmark is rotated from the camera frame to the spacecraft frame, and to the Vesta-fixed frame to give the vectors $\hat{\mathbf{v}}_1$ and $\hat{\mathbf{v}}_2$, shown in Figure 4-1. The image constraint residual d is the minimum distance between $\hat{\mathbf{v}}_1$ and $\hat{\mathbf{v}}_2$ and is defined by:

$$d = (\mathbf{P_1} - \mathbf{P_2})^T \left(\frac{\hat{\mathbf{v}}_1 \times \hat{\mathbf{v}}_2}{||\hat{\mathbf{v}}_1 \times \hat{\mathbf{v}}_2||} \right) \tag{4.1}$$

where $\mathbf{P_1}$ and $\mathbf{P_2}$ are the position of the spacecraft at times $t_1$and t_2. In theory, d should be zero, but it is not due to errors in the spacecraft position, attitude, camera pointing, focal length and distortion. GEODYN has been modified to minimize d by updating the spacecraft position at times t_1 and t_2, as well as the spacecraft attitude, camera model and planetary orientation parameters. The camera model used to compute the vectors from the camera to the landmark starting with pixel coordinates includes radial, "tip," and "tilt" distortion parameters. Radial distortion refers to distortion of pixels dependent on their distance from the optical axis. Tip and tilt parameters model the misalignment between the detector and the camera axis. For

further information on this model, the reader is referred to Owen [93].

4.4 Methodology

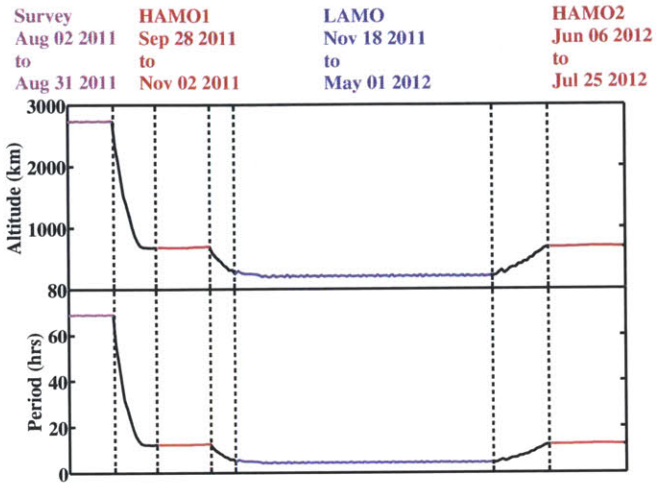

Figure 4-3: Altitude and orbit period of the Dawn spacecraft during the mission at Vesta.

While at Vesta, the Dawn spacecraft conducted four mission phases to accomplish various mission objectives: the Survey orbit, the first high-altitude mapping orbit (HAMO), the low-altitude mapping orbit (LAMO), and finally a second HAMO phase. The Survey orbit has an altitude of 2700 km, and a period of 68 hours. The HAMO orbit phases have an altitude of about 725 km, and a period of 12.1 hours, and the LAMO orbit has an altitude of about 200 km, and a period of about 4.4 hours. These orbit phases are detailed in Table 4.2 and Figure 4-3. In this work, data from time periods in which spacecraft operations minimally affected the orbit were culled for orbit determination. As a result, orbit time spans were selected to exclude times of transition between the orbits listed in Table 4.2, as well as large attitude slews, angular momentum wheel desaturation events, and spacecraft safing events. Over the course of its mission at Vesta, the spacecraft fired its attitude control thrusters every two to three days to desaturate its control momentum wheels. These selection

Orbit Phase	Survey	HAMO1	LAMO	HAMO2
Altitude (km) [14]	2725-2737	663-701	169-324	650-714
Period [14]	2.87 days	12.17 hours	4.25 hours	12.18 hours
Begin Time [14]	Aug. 2, 2011 07:49	Sep. 28, 2011 10:46	Nov. 18, 2011 02:00	June 6, 2012 06:00
End Time [14]	Aug. 31, 2011 21:39	Nov. 2, 2011 11:04	May 01,. 2012 12:00	July 25, 2012 15:00
Number of Doppler Data	21667	29514	92206	26449
Number of Range Data	4169	6531	4466	4901
Number of Image Constraints	8000	6000	18835	4994

Table 4.2: Orbital characteristics and numbers of various OD measurements used in the different phases of flight of the Dawn mission at Vesta.

criteria yielded 106 16- to 110-hour time spans (arcs) that were analyzed. The length of an arc depended on the mission phase, since lower-altitude orbits required more frequent maintenance and momentum wheel desaturations, which resulted in shorter arc spans. There were seven Survey arcs, 21 HAMO arcs and 77 LAMO arcs. Survey arcs were 1.5 to 3.5 days long and HAMO arcs were 2 to 4.5 days long. During the LAMO orbit the mean arc length was 1.5 days long, with a minimum of 16 hours and a maximum of 2.6 days.

GEODYN was parameterized to estimate the six Keplerian orbital elements for each arc. Other parameters adjusted in each iteration included scale factors for solar radiation pressure, radial, along-track and cross-track empirical accelerations, tracking station range biases, X-Y-Z spacecraft antenna offsets for both the high gain and low gain antennas, specular and diffuse reflectivities for a six-sided spacecraft macromodel, camera orientation biases, and camera distortion parameters; in total, 45 parameters per arc. Delay effects of the Earth's troposphere and ionosphere were modeled for radiometric measurements. In this study the gravity field and orientation parameters of Vesta were not estimated but held constant because our objective was to examine the effects and performance of the new image constraint data type

and not to estimate the geophysical parameters of Vesta. We used the degree and order 20 gravity model for Vesta and orientation parameters computed by the Dawn science team [14]. The solar system planetary ephemeris used in this study is DE421, and is archived by the Planetary Data System [94] and the Navigation and Ancillary Information Facility (NAIF) [95]. The spacecraft was modeled as a six-sided bus with two gimbaled solar arrays. The spacecraft attitude and solar array pointing, as well as the initial Keplerian elements were obtained from telemetry and navigation reconstruction archived at the NASA PDS [94].

The measurement weights in GEODYN were chosen based on typical noise characteristics of the DSN data. Dawn utilized 2- and 3-way X-band Doppler and range measurements to track the spacecraft. The uplink signal is 7179 MHz and the downlink signal is 8435 MHz. Doppler measurements with this system carry about 0.05 mm/s noise over 10-second integration times. The noise can increase to 0.35 mm/s depending on the Sun-Earth-Probe (SEP) angle and the thermal environment of the spacecraft (see Konopliv, et al., [14]). Range data typically carry 1-2 m of noise (see Konopliv et al., and [80], Moyer et al., [88]). For the Dawn mission, DSN Doppler measurements were integrated over 60 seconds, while range measurements were integrated over 1-2 minutes. The measurement weights used for radiometric tracking measurements were selected to be 1 mm/s and 2 m for Doppler and range, respectively. These weights were purposely selected to be larger than typical minimum residual root mean square (RMS) magnitudes so we would not overweigh the data. The measurement weight associated with the image constraints was chosen based on the image pixel scale and landmark position uncertainties: 150 m, 70 m and 30 m during the Survey, HAMO and LAMO orbits, respectively.

The Dawn spacecraft has two Framing Cameras (FCs) with a broadband visible and seven narrow band filters. Their field of view is 5.5° × 5.5°, and the sensor is a 1024 × 1024 CCD (see Sierks et al. [96]). Robert Gaskell defined 150,214 landmarks using 17,189 images in the creation of the Vesta shape model. The 5.34-hour rotation period of Vesta, combined with the 4-to-68 hour orbital periods shown in Table 4.2 resulted in over two million possible image constraint combinations. The large number

of landmarks was required for the creation of a high-fidelity shape model. The fact that there were so many possible landmark combinations in the creation of image constraints for GEODYN allowed us to select for spatial and temporal uniformity. The number of possible combinations was culled to increase computational speed, and also to provide a number of image constraints that was comparable to the number of range and Doppler observations used. Landmarks were selected based on parameters that varied with orbital altitude. In the Survey orbit, only the landmarks closest to a 2-degree grid on the surface of the body were selected. These were further limited to constraint combinations that had at least a 120-minute time-span between them. During HAMO, these criteria were relaxed to accommodate the smaller camera footprint on the surface of Vesta, and geographic spacing was relaxed to 1 degree and 60 minutes apart, and in the LAMO configuration, spacing was 0.2 degrees and 30 minutes. The distribution of the radiometric measurements and image constraints utilized in each orbit phase is shown in Table 4.2.

4.5 Results

The performance of Dawn POD was characterized through the level of radiometric and image constraint residuals and agreement with the published trajectory computed by the Dawn Science Team. Table 4.3 shows the various measurement residual root mean square (RMS) values for each phase of the mission at Vesta. Doppler residual RMS values spanned from 0.067 mm/s in the August 2011 to about 0.44 mm/s in July 2012. The range residuals in August 2011 were 0.71 m to 1.5 m in July 2012. The increase in residuals is a result of the decreasing SEP angle, which causes the noise inherent in the radiometric measurements to increase. This effect was predicted in Konopliv [80], and observed by the Dawn Science Team, as detailed by Konopliv et al. [14]. An example of Doppler and range residuals is shown in Figure 4-4. Figure 4-5 shows the stability of the orbital elements over successive iterative fits of the orbit using GEODYN.

The image constraint residual RMS values were dependent on the spacecraft al-

Orbit Phase	Doppler RMS (mm/s)	Range RMS (m)	Images Constraint RMS (m)
Survey	0.067	0.71	113
HAMO1	0.11	1.0	53
LAMO	0.44	1.5	22.9
HAMO2	0.15	1.1	57

Table 4.3: Residual RMS values during the different orbit phases of the Dawn mission at Vesta.

titude, and the image constraint RMS for each phase was less than 1 pixel for all mission phases. The use of image constraints generally caused radiometric residuals to increase slightly by less than 0.01 mm/s and 0.1 meters. This effect is not unexpected in least-squares estimation when a new data type is added. Plots of image constraint residuals during Survey, HAMO, and LAMO are shown in Figures 4-6, 4-7, and 4-8, respectively.

Another way performance was characterized was by directly comparing the trajectory computed with GEODYN to that computed by the Dawn Science Team. Table 4.4 shows the RMS of the difference of the radial, along and cross track differences for the various orbit phases, with and without the application of image constraints. Figure 4-9 shows the RMS of these differences with and without using image constraints in the radial, along- and cross-track orbit components. In the Survey phase of the mission, where the gravitational environment is weakest, the differences without images were 3.62 and 1.76 kilometers in the along- and cross-track components, respectively. This was reduced to 591 and 105 meters with the utilization of image constraints. During the first HAMO phase the RMS difference between the two trajectories decreased by several meters. For LAMO and HAMO2, there was little change as a result of adding image constraints. The LAMO trajectory computed with GEODYN differed with the science team's solution by about 12 m total RMS, and during the HAMO2 phase by about 29 m.

Orbit Phase Phase Phase	Radial (m) (Radiometric/ Radiometric + Image Constraints)	Along-Track (m)	Cross-Track (m)	Total (m)
Survey	83.2/84.8	3629/575	1768/105	4041/591
HAMO1	15.6/15.7	87.5/73.8	75.0/68.9	116/102
LAMO	5.1/5.1	8.8/8.2	5.9/5.7	12.5/11.9
HAMO2	17.8/17.8	12.2/13.8	17.1/17.4	28.6/29.5

Table 4.4: RMS of the difference between the spacecraft trajectory computed with GEODYN and that computed by the Dawn Science Team.

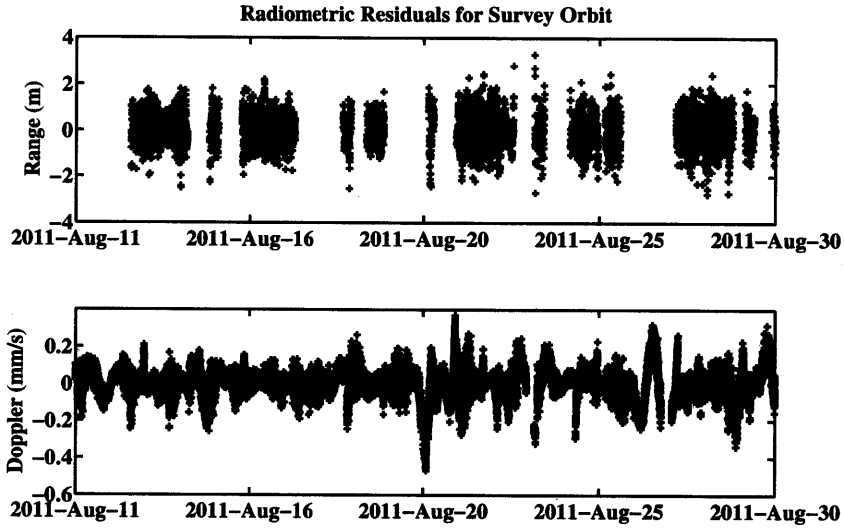

Figure 4-4: Radiometric residuals during the Survey orbit phase.

4.6 Conclusions

This work has demonstrated the capability of using image constraints in GEODYN for orbit determination. Final radiometric and image constraint residuals are reflective of the measurement noise of the instrumentation used. Orbit elements are stable over several iterations of GEODYN. Most of the improvement due to utilizing image constraints was observed in agreement between the GEODYN position and that computed by the Dawn Science Team during the highest altitude (Survey) phase of the mission. The improvements were mostly noted in the along- and cross-track directions, where the consistency between the trajectories improved from several km

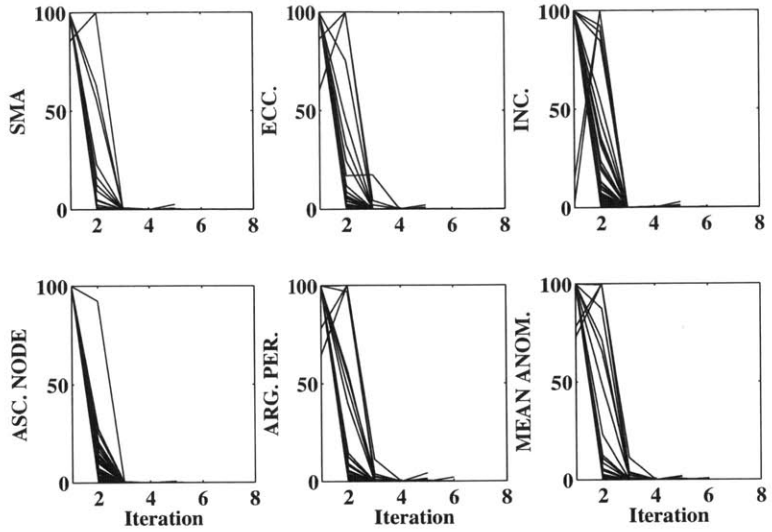

Figure 4-5: Percent of total change in orbital elements per GEODYN iteration for 106 16-to-110-hour-long arcs during Survey, HAMO, and LAMO. Generally, over 90% of the total change in the elements occurs in the first three iterations.

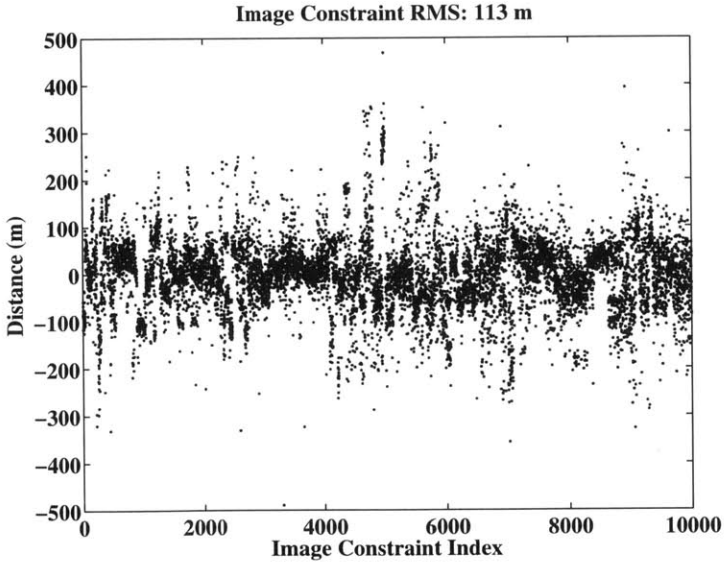

Figure 4-6: Image constraint residuals during the Survey orbit phase.

to under 600 m. Agreement between the trajectory produced by GEODYN and that computed by the Dawn Science Team is less than 10 meters during the low-altitude phase of the mission, mainly as a result of the strength of the Doppler data in the

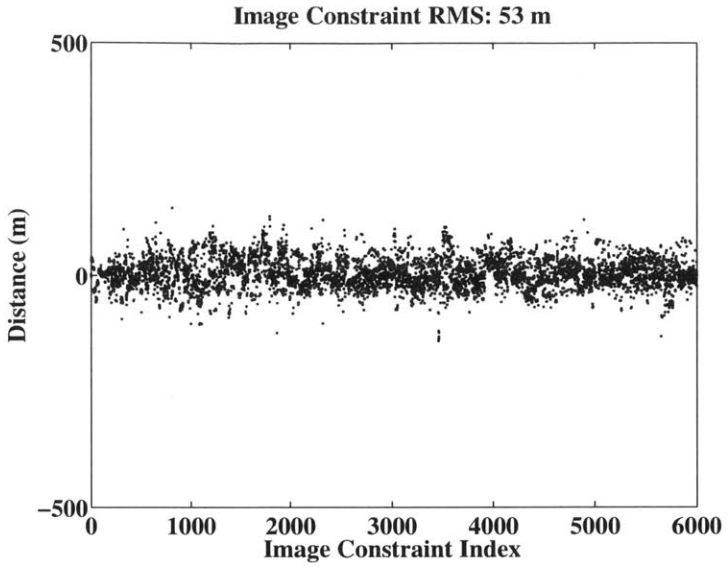

Figure 4-7: Image constraint residuals during the first HAMO orbit phase.

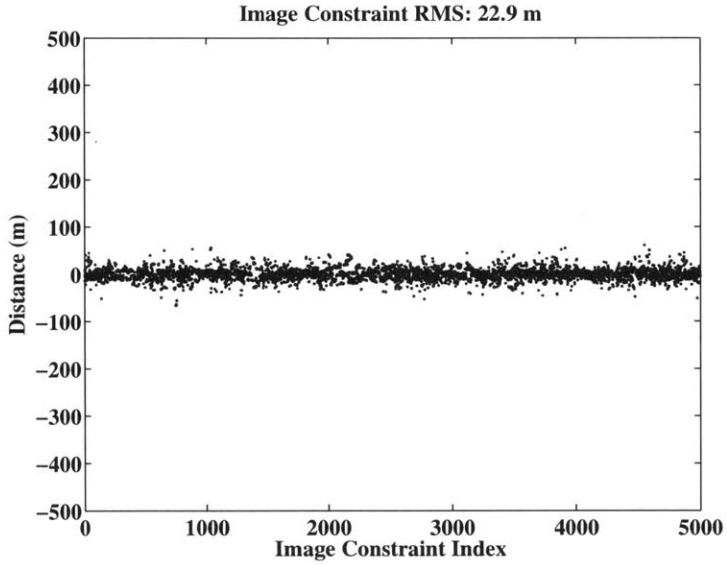

Figure 4-8: Image constraint residuals during the LAMO orbit phase.

stronger gravity environment.

The demonstration of using image constraints in GEODYN will aid in the orbit reconstruction effort of future missions. The application of this technique can be used in the recovery of the gravity field and rotation axis orientation of planetary bodies. These results contribute to the geophysical understanding of a planetary body and

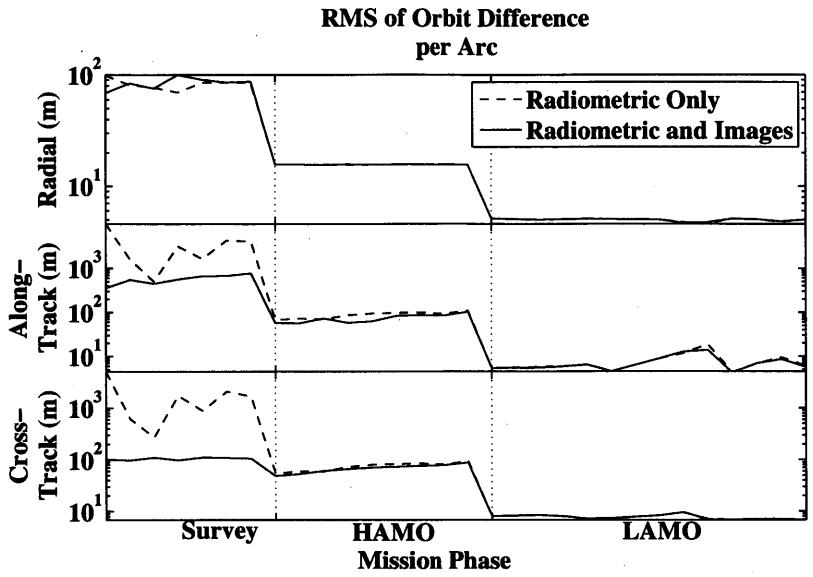

Figure 4-9: RMS difference between the GEODYN trajectory and that computed by the Dawn Science Team in the radial, along-, and cross-track components.

its formation. They also will improve the accuracy of the definition of a body-fixed reference frame, to which other scientific datasets can be registered.

There are many opportunities to apply this new capability to future scientific investigations. The most apparent application is the computation of the gravity field and orientation parameters of Vesta with GEODYN. The fact that most of the improvement from using images occurs in the highest altitude phase of the mission suggests that this technique will aid most in the estimation of the pole orientation of Vesta as well as the low-degree gravity harmonic coefficients. Next, the Dawn spacecraft will arrive at the protoplanet 1 Ceres, where this orbit determination technique can be used to aid the geophysical investigation there. The new image constraint capability in GEODYN also has applications with missions such as NEAR, OSIRIS-REx, and future small-body missions with high-resolution images.

Chapter 5

Vesta Gravity and Spin Axis Orientation Recovery

5.1 Abstract

Image constraints, which represent a new data type applicable in GEODYN software, were combined with radiometric Doppler and range measurements to estimate the orbit of the Dawn spacecraft, the gravity field and the orientation parameters of the asteroid 4 Vesta. Using image constraints substantially aided in the initial determination of the Vesta pole orientation as well as the GM and J_2 parameters. The image constraints enhanced orbit knowledge in the along- and cross-track orbit components, and thus improved the observability of the orientation parameters. The pole orientation estimated here differed from that computed by the Dawn Science Team by 0.01°. After the low-degree gravity field and orientation parameters were estimated, a gravity field of Vesta of degree and order 5 was estimated. This gravity model agreed in magnitude and spatial distribution with that presented by the Dawn Science Team using a different software analysis system. The differences in power between the two fields was less than 5% up to degree 4. The agreement between the gravity model presented here and that presented by Konopliv et al., [97] also serves to corroborate the suggested thicknesses for a proposed three-layer structural model of Vesta [65], and the extent of Vesta's equatorial bulge, which is indicative of past

state characterized by higher temperature and more rapid rotation than observed today [98]. This analysis demonstrates the utility of image constraints for space-based geophysical investigations of small bodies, where non-conservative accelerations are the dominant source of orbit error.

5.2 Introduction

Launched in 2007, the Dawn investigative mission is to explore Vesta and Ceres, located in the main asteroid belt. Representing a unique opportunity for planetary science, this mission has provided new insight into planetary bodies that do not fit neatly into the classification of "asteroid" or "planet." Thought to be the remnants of early planetary formation processes, the investigation of Vesta and Ceres can yield unparalleled insight into the conditions of the early solar system during the planetary accretion process (see Russell [99] and Bottke [100]). The asteroid belt is composed of hundreds of thousands of objects which have been observed and many more which have not. The vast majority of these orbit the sun at a mean semi-major axis between 2.1 and 3.5 AU. Most of the asteroids have diameters less than 100 km, and are carbonaceous in composition (C type). Carbonaceous material contains grains from before the first 10^8 Myr after the formation of the planetary accretion disk (see DePater and Lissuaer [101], and Gradie [102]).

Modeling the interior structure and composition of planetary bodies is informed by precisely computing the trajectory of orbiting spacecraft. Precision orbit determination (POD), which accounts for small non-conservative accelerations such as solar radiation pressure, reveals the accelerations caused by the gravitational field of the body itself. In turn, the quality of the gravity field knowledge is essential for orbit determination and navigation at small, non-uniform bodies. For planetary bodies, the iterative process of POD and gravity field estimation makes observable non-uniformities in the gravity field with which we can begin to infer the density, structure, and chemical constitution of the body's interior.

While the Dawn spacecraft was at Vesta, there were four distinct mapping phases:

Orbit Phase	Survey	HAMO1	LAMO	HAMO2
Altitude (km) [14]	2725-2737	663-701	169-324	650-714
Period [14]	2.87 days	12.17 hours	4.25 hours	12.18 hours
Begin Time [14]	Aug. 2, 2011 07:49	Sep. 28, 2011 10:46	Nov. 18, 2011 02:00	June 6, 2012 06:00
End Time [14]	Aug. 31, 2011 21:39	Nov. 2, 2011 11:04	May 01, 2012 12:00	July 25, 2012 15:00
Number of Doppler Data	21667	29514	92206	26449
Number of Range Data	4169	6531	4466	4901
Number of Image Constraints	8000	6000	18835	4994

Table 5.1: Orbital characteristics and numbers of various OD measurements used in the different phases of flight of the Dawn mission at Vesta.

Survey, the first High-altitude mapping orbit (HAMO), the low altitude mapping orbit (LAMO), and a second HAMO orbit. These are detailed in Table. 5.1. The various orbits were planned in order to achieve various mission objectives while allowing successive improvements in the determination of the pole and gravity field. In the Survey orbit, which had a 2700 km altitude, the pole and low-degree gravity coefficients were determined. In the HAMO (altitude 700 km), and LAMO (altitude 200 km) phases, higher degree gravity coefficients became observable, to degree and order 20 (see Konopliv et al., [97]).

In the work presented here, the radiometric and image data from the Survey phase of the Dawn mission at Vesta are used for POD and gravity field recovery to demonstrate the effect of using image constraints on the calculation of the spin axis orientation and low-degree gravity coefficients. The image constraints will have the largest effect in the Survey phase due to the relatively high uncertainty in the *a priori* knowledge of the pole orientation, GM and J_2 parameters at the start of the Survey orbit, compared to the HAMO and LAMO phases. Data from the HAMO and LAMO orbit phases will be included in the estimation of the gravity field in future efforts.

5.3 Early Planet Formation & the Asteroid Belt

One stage in the formation of terrestrial planets is the collision of bodies at low enough velocity so that their collective material will mutually accrete rather than fragment (see dePater and Lissauer [101]). Some of the contents of the asteroid belt are the fragmented results of these collisions, and others are the products of the nascent stages of planet formation. In this way the contents of the asteroid belt represent some of the building blocks of planet (see Chambers [103]).

A relative handful of the asteroids have accreted to 100 km or more in diameter, and have survived to the present (see McCord [104]). Vesta's polar radius is 226.838 km, and its equatorial radii are 284.895 km and 277.431 km (see Ermakov et al., [65]). Ceres has a polar radius of approximately 455 km, and a mean equatorial radius of 487 km (see Thomas [105]). Additionally, Vesta and Ceres exhibit evidence of differentiation likely due to the heat sustained through accretional collisions and the decay of radiogenic isotopes. At these large diameters, Vesta and Ceres are distinct from the rest of the asteroid population in that their self-gravitation offers an additional potential source of heat which aids in core and mantle formation (see Halliday [106]).

Another important factor in considering asteroid belt objects is that at approximately 2.7 AU, our Solar System's "snow line" marked the boundary beyond which the temperature is below the condensation temperature of water in the protoplanetary disk (see Lecar [107]). Thus, early solar system bodies that have orbits beyond $\sim$2.7 AU had a much greater possibility of retaining water and volatiles. This zone is a possible volatile reservoir from which water could have been transported to the terrestrial planets of the inner Solar System (see Chyba [108]).

Ceres and Vesta, in addition to being in a class of bodies unique in the asteroid belt, are vastly different from one another. Vesta is differentiated, has approximately half the diameter of Ceres, and orbits inside the snow line. The mean density of Ceres is less than two-thirds that of Vesta ($\rho_{Ceres} = 2.077$ kg/m^3, $\rho_{Vesta} = 3.456$ kg/m^3) [104], and orbits outside the snow line. These major differences provide a starting

point from which we can examine Vesta and Ceres with respect to one another.

It has been known since prior to the Dawn mission that Vesta is a differentiated body (see Zuber [76]). Analysis by Fu et al., has shown that the magnetic signatures of HED meteorites, thought to be from Vesta, have provided evidence of a radiogenic heat source and convecting interior [109]. As a result of the orbit determination and gravity recovery at Vesta, a range of internal structure models have been developed. Because interior structure modeling from gravity and topography datasets is non-unique, we are required to make assumptions about the various thicknesses and densities of the layers of the structural model (see Bills et al., [110] and Park, et al., [111]).

Vesta's oblate shape adds to the complexity of gravity estimation and interior structure modeling. Traditionally a spherical harmonic expansion is used to model the gravitational fields of planetary bodies. This has worked well since the terrestrial planets from which we have estimated gravity fields have a flattening less than 0.01. Vesta's flattening is nearly 0.2, and has a strongly oblate, non-hydrostatic shape. When spherical harmonics are used in this case, there is attenuation of the gravity in the polar regions, because the spherical harmonics are mapped to a spherical surface which circumscribes the shape of Vesta (known as a Brillouin sphere, which has a radius of 292.7 km for Vesta [111]). In the north, Vesta's shape is almost 70 km from the Brillouin sphere. Spherical harmonic gravity solutions diverge when the surface of the body does not fit well to the Brillouin sphere. Park et all address this by computing an ellipsoidal harmonic gravity model which is mapped to a 303.9 km $\times$ 228.7 km $\times$ 246.5 kmBrillouin *ellipsoid* [111]. An ellipsoidal expansion is not employed in this work, but the gravity model computed is compared with the spherical harmonic gravity model computed by the Dawn Science Team (see Konopliv et al., [97]).

When modeling the interior structure of Vesta, we begin by assuming densities from the howardite-eucrite-diogenite (HED) meteorite collection. The HED meteorites have a similar isotopic signature to Vesta, and are thought to have originated there (see McCord, et al., [112]). Densities or ranges of densities must be selected for

each of the zones in a three-layer model, consisting of a core, mantle and crust. From this point, using the gravity model, we can compute thicknesses for the various layers of the model. Current results from the Dawn mission at Vesta, carried out by Ermakov et al., Park et al., and Konopliv et al., suggest a three layer model of Vesta with a core between 110-140 km, and a core density bounded as 7000 kg/m^3 $< \rho_c <$ 8000 kg/m^3. Generally the mantle can be constrained to 100-150 km in thickness with an assumed density ranging from 3150 kg/m^3 $< \rho_m <$ 3500 kg/m^3, while the crust can be up to 55 km thick, with an assumed density of 2900 kg/m^3 $< \rho_c <$ 3400 kg/m^3 ([111],[65], [97]).

Ceres presents a greater challenge since we have no known specific samples that can be used to constrain its density. Many interior models predict a rocky core covered by a layer of ice and rock up to 100 km thick [113]. The surface of Ceres is dark and uniform and current results suggest this could mean that there may not be a layer of ice. If there is ice at Ceres, it is underneath a thin veneer of rock or clay on the surface, and thus hidden from detection (see Rivkin et al., [114]). It has also been suggested that the smoothness could indicate the presence of an icy mantle, as this would promote relatively rapid crater relaxation at the equatorial and mid-latitudes (see Bland [115]). Furthermore, it has been suggested by Zolotov that the data we have of Ceres may not be consistent with a differentiated body [116]. The Dawn mission will provide insight into the possible presence and thickness of an ice layer through the complementary measurements of the shape and gravity field of Ceres.

5.4 Gravity Recovery

The GEODYN and SOLVE programs were used to estimate the gravity field and spin axis orientation of Vesta using data from the Dawn spacecraft. GEODYN is the orbit determination and geodetic parameter estimation software of NASA Goddard Space flight Center and is maintained by Stinger Ghaffarian Technologies, Inc. GEODYN iteratively integrates the trajectory of a spacecraft and fits estimated parameters to minimize the residuals between computed and measured observations [10]. This work

represents the first time image constraints are utilized by GEODYN and SOLVE to estimate the geodetic parameters of a planetary body. GEODYN uses a Cowell's method integrator and models the gravitation of the solar system along with non-conservative accelerations such as thrusting, solar radiation pressure, and atmospheric drag.

After the orbit solutions stabilize for a given geophysical model, GEODYN outputs normal matrices, which contain partial derivatives of global parameters with respect to the measurement residuals for the Doppler, range and image constraint data types. SOLVE uses a weighted least squares algorithm to compute global parameters specified by the user (see Crassidis [32]). In this case, global parameters are selected as the gravity field and pole, along with antenna offset models, once-per-revolution general accelerations, and solar radiation pressure coefficients. Once SOLVE determines a new gravity field and pole, the orbits are re-computed in the next iteration.

Previous efforts to estimate the Vesta gravity field have been made by the Dawn Science Team, at the Jet Propulsion Laboratory (JPL) [14]. The work presented by Konopliv et al. made use of JPL's MIRAGE square root information filter (SRIF) software ([16],[88]). The SRIF algorithm is a sequential state estimator, meaning that it estimates the spacecraft trajectory and relevant parameters such as empirical accelerations as it propagates the orbit, utilizing knowledge of the measurement noise and the amount of expected variance in the state estimates from one time step to the next (see Crassidis [32]). GEODYN and SOLVE are "batch" processing algorithms in that they compute the satellite trajectory, and fit the estimated parameters *after* each integration of the trajectory. In this way, we are comparing two different estimation algorithms.

The work presented here shows the first results of an effort to use image constraints in GEODYN and SOLVE, as well as to corroborate and compare the results of the Dawn Science Team. While orbit determination is typically performed using radiometric range and Doppler measurements between Earth-based tracking stations and the spacecraft, other measurements are often used to improve the orbit and gravity determination capability of a mission. Examples of supportive measurements

include spacecraft-to-spacecraft ranging (see Zuber [72]), laser altimetric crossovers (see Mazarico [117]), and in this case image constraints. Image constraints have proven to be extremely valuable for navigation and orbit determination at small bodies, with weak, non-uniform gravity fields where non-conservative forces such as that caused by solar radiation pressure can dominate the orbit perturbations. Optical orbit determination was first employed by the Near Earth Asteroid Rendezvous (NEAR) mission at the asteroid 433 Eros, and was described by Miller et al., [118]. OD with constraints from images have been employed on several subsequent missions, such as Hayabusa ([119] and [78]).

Utilizing additional constraints for orbit determination is especially important for the Dawn spacecraft because of the frequent thrusting required to maintain the orbit in a highly non-uniform gravity field, as well as the modeling of the non-conservative accelerations affecting the spacecraft orbit (see Tricarico and Sykes, [120] and Delsate, [121]). The spacecraft maintains its orbit using a Solar Electric Propulsion (SEP) system with ion thrusters, detailed by Brophy [122]. The effect of solar radiation pressure is magnified due to the fact that Dawn's solar arrays make up over 70% of the spacecraft surface area ([81], [80]).

5.5 Mission Overview and Measurements

The Dawn mission at Vesta was comprised of four major orbit phases to accomplish various mission objectives, one of which was to record sufficient orbital trajectories to map the gravity field to degree and order 20 (see Konopliv et al, [80]). The spacecraft was inserted into a Survey orbit from August 2, 2011 through August 31 2011. The Survey orbit had an approximate altitude of 2700 km, and a period of 68 hours. The next orbit phase was the first High Altitude Mapping Orbit (HAMO1), and lasted from September 28, 2011 until November 2, 2011. HAMO1 had an altitude of approximately 700 km and a 12.7-hour period. From November 18, 2011 through May 1, 2012, Dawn was placed in the Low Altitude Mapping Orbit (LAMO). The altitude of LAMO varied between 169 and 324 km, and its period was 4.25 hours.

Only data from the Survey phase of the mission is used in the gravity recovery and orientation parameter investigation in this paper.

Radiometric Doppler and range measurements were recorded via the Deep Space Network (DSN) (see Moyer [88]), which are a family of antennas of 26-m, 35-m and 70-m diameters deployed globally that NASA uses to track spacecraft. Typically Doppler measurements carry a noise RMS of 0.05 mm/s, and range measurement noise RMS is less than 1 m.

In addition to the radiometric measurements, this investigation utilized constraints derived from images of Vesta obtained by the Dawn spacecraft. The image constraints were derived from the pixel locations of landmarks recorded in two or more images by the Dawn Framing Cameras (FC) (see Sierks et al., [96]). The pixel information used in this work is a byproduct of the Vesta shape model created by Gaskell (see [92]). To create an image constraint, the pixel locations of the same landmark in two or more images taken at two different times were used to compute unit vectors that point from the Dawn spacecraft to the landmark on the surface of Vesta. The GEODYN and SOLVE programs have been programmed to minimize the distance between the two unit vectors, which is nonzero due to uncertainties in the spacecraft position, attitude and camera model. The image constraints carried a measurement root mean square (RMS) which is the pixel scale for the given mission phase. For the images taken during the Survey phase, this RMS was 150 m/pixel ([80]).

The radiometric and image data used were selected from times of minimal spacecraft operations. Data during thrusting, spacecraft safing events, momentum wheel desaturations, and major attitude maneuvers were excluded, because the effects of modeling these perturbations on the trajectory can degrade the gravity solution. The spacecraft typically fired its thrusters every 2 to 3 days to desaturate its momentum wheels. These events typically lasted 2 minutes. Culling these events resulted in seven "quiet" periods which lasted from 1.5 to 3.5 days during the Survey orbit phase from which radiometric and image constraints were selected.

In the Survey orbit image constraint combinations had to be culled. Due to the long Survey orbit period and the fact that Vesta rotates 360° in 5.34 hours, millions

of landmarks could be used in combination to create image constraints. To cull this amount, and speed computation, only landmarks that were observed closest to a $2° \times 2°$ grid on the surface were selected for the creation of image constraints. In total 4169 range measurements, 21667 Doppler measurements and 8000 image constraints were used in this work.

5.5.1 Estimation Technique

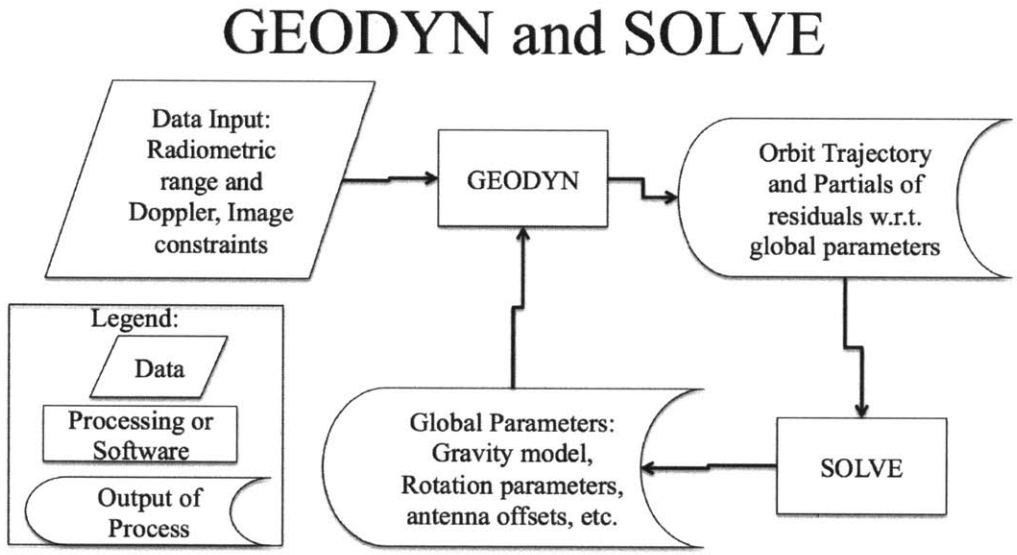

Figure 5-1: Flow diagram depicting the iterative use of the GEODYN and SOLVE programs.

The work flow for this research is separated into two tasks: orbit determination, and gravity field estimation and is shown in Figure 5-1. The POD step is carried out using GEODYN software, and the estimation of the gravity field and orienta-

tion parameters is performed with SOLVE, a companion program which can compute geodetic parameters using normal matrices computed and outputted by GEODYN. SOLVE in this case has been configured to estimate the gravity field, the orientation parameters, spacecraft antenna offsets, camera attitude biases, empirical accelerations, and solar radiation pressure coefficients. The gravity field is described with a spherical harmonic model. SOLVE estimates the parameters of the harmonic expansion of this model, given as described by Heiskanen et al., in [60], and Kaula in [123]:

$$U = \frac{GM}{r} + \frac{GM}{r}\sum_{n=1}^{\infty}\sum_{m=0}^{n}\left(\frac{R_V}{r}\right)^n \bar{P}_{nm}(\sin\phi_{lat})\left[\bar{C}_{nm}\cos(m\lambda) + \bar{S}_{nm}\sin(m\lambda)\right] \quad (5.1)$$

The potential field of the body is described by U, in terms of distance from its barycenter r, its latitude ϕ_{lat} and longitude λ. Here n and m are the degree and order of the harmonic computed, and R_V is a reference radius for Vesta, 265 km. SOLVE estimates the gravitational constant GM, and the coefficients of the expansion $\bar{C}_{nm}$ and $\bar{S}_{nm}$.

The *a priori* values for the pole were set to the values determined by Thomas et al., ([124]), via the use of photometric data from the Hubble Space Telescope. The right ascension (RA) was estimated to be 301°, the declination (DEC) was determined to be 41°, and length of day (LOD) estimated was 1617.33277°/day. The *a priori* gravity model used was the same used by the Dawn Science Team, and was created using a shape model created using photometric data from the Hubble Space Telescope, with an assumption of constant density. The gravitational constant and J_2 of the *a priori* model are $GM = 17.5 \times 10^9$ km^2/s^2, $J_2 = 0.03868$, and are consistent with their *a priori* knowledge, before the arrival of Dawn at Vesta [80].

The process of estimating the gravity field and pole was done incrementally. First the pole orientation parameters, rotation rate, GM, and J_2 were estimated while holding the spacecraft orbital elements constant. This strategy for the initial estimation was performed because when starting with a pole and gravity model that was so different from the present accepted solution, that GEODYN could not converge an

orbit trajectory. It still, however, provided enough partial information of the gravity field and orientation parameters to allow SOLVE to estimate the pole and low-degree gravity field. After the pole orientation, GM and J_2 stabilized in the initial estimation, the spacecraft orbital elements were allowed to vary. In this configuration the pole orientation, GM, and J_2 were further refined and a gravity field of degree and order 5 was estimated.

5.6 Results

The results of the initial convergence of the pole and low-degree gravity parameters are shown in Figs. 5-2 through 5-4. In general, the pole orientation, GM, and J_2 converge and stabilize more quickly when image constraints are used, than when images are not used. In Figure 5-2, it can be seen that when image constraints are used, the pole orientation converged after five iterations. When image constraints are not used, the RA stays stable near 300° and the DEC is not converged after 20 iterations. The convergence of the LOD is shown in Fig. 5-3. The solution in which image constraints are used settles after 10 iterations, and the radiometric-only solution settles after 14 iterations. This result is supported by the geometric nature of image constraints, which enhance the sensitivity of the estimation to the spin rate and axis orientation.

The initial estimation of GM and J_2 are shown in Fig. 5-4. When images are used, the estimates of GM and J_2 settle near the value determined by the Dawn Science Team after the second iteration, whereas the solution without image constraints takes much longer to converge. Figure 5-5 shows the initial convergence of the degree-2 gravity coefficients. When image constraints are utilized, the C_{21} and S_{21} parameters are stabilized after 5 iterations. The C_{22} and S_{22} coefficients are stable after 10 iterations when image constraints are used. When only radiometric constraints are used, the degree-2 gravity coefficients take more than 15 iterations to stabilize.

The next stage in the estimation of the gravitational field was to use the pole RA, DEC, LOD, GM and J_2 as the initial conditions for GEODYN in which the POD

solution was allowed to fully converge. In this step, GEODYN was allowed to iterate the orbit solutions while estimating the initial spacecraft ephemeris, solar radiation pressure coefficients, empirical accelerations, measurement biases, and camera model parameters. Full-convergence of the orbit determination is favorable in that it allows the orbit parameters to be converged as much as they can be without updating the Vesta geophysical properties. The final measurement residual RMS values during this phase of the estimation were 0.068 mm/s for Doppler, 0.82 m for range, and 114 m for the image constraints.

In the estimation of the gravity field, a Kaula power law constraint was applied with a relative weight of 0.1, where as the normal matrix from GEODYN was weighted 1.0. This is the same as was applied by Konopliv et al., [97] and is defined by Kaula [125] as:

$$M_n = \frac{K_{Vesta}}{n^2} \tag{5.2}$$

where K_{Vesta} is computed as:

$$K_{Vesta} = K_{Earth}\left(\frac{M_{Earth}}{M_{Vesta}}\right)^2\left(\frac{R_{Vesta}}{R_{Earth}}\right)^4 = 0.011 \tag{5.3}$$

Here, $M_{Earth} = 5.972 \times 10^{24}$ kg, $M_{Vesta} = 2.59 \times 10^{20}$ kg, and $R_{Vesta} = 265$ km, and $R_{Earth} = 6371$ km. The Kaula parameter for Earth is defined as $K_{Earth} = 0.0691$.

The orientation parameters and normalized gravity coefficients for each phase of the estimation are shown in Tables 5.3 and 5.4. The full-arc convergence GEODYN-SOLVE solution RA and DEC differ from the Dawn Science team by 0.004° and 0.03°, respectively. The final $3-\sigma$ uncertainty in the pole RA and DEC is 5.4×10^{-2}°. The final GEODYN GM and J_2 values differ from the JGV20G02 solution by 4.0×10^{-4}% and 0.05%, respectively. The J_3 and J_4 parameters agree with the JGV20G02 solution to within 0.5% and J_5 to within 6%. The uncertainties associated with the GEODYN gravity model are much larger than those of the JGV20G02 model. This is expected due to the fact that this analysis only incorporates one month of radiometric data in the gravity estimation, whereas the JGV20G02 model utilizes data from the enter Vesta mapping mission, which lasted 12 months.

The Low-gain Antenna (LGA) offsets were estimated to be $\Delta X = 0.10$ m, $\Delta Y = 0.18$ m, and $\Delta Z = -0.57$ m, and the High-gain Antenna (HGA) offsets were $\Delta X = 1.26$ m, $\Delta Y = -0.01$ m, and $\Delta Z = 1.09$ m. The $3-\sigma$ uncertainty for the antenna offsets was 0.9 m in all directions for both the LGA and the HGA. Their estimation with subsequent iterations of GEODYN and SOLVE is shown in Fig. 5-6. For the Survey phase of the mission, there were 12506 Doppler measurements and 4169 range measurements from the HGA used here. There were 9161 Doppler measurements from the LGA (no range data were recorded on the LGA). Once-per-revolution empirical acceleration coefficients were applied, and estimated by both GEODYN and SOLVE. The final estimates of these parameters ranged between 1×10^{-10} and 1×10^{-12} m/s^2, and were allowed to vary up to 1×10^{-8} m/s^2. The empirical acceleration coefficients are unitless because they act as multipliers on the actual accelerations in GEODYN. The small magnitude of these parameters with respect to the amount of variation allowed suggests empirical accelerations were not absorbing gravitational effects on the orbit.

The power of the gravity field from degree and order 2 through 6 is shown in Fig. 5-7. Here it can be seen that the power in the GEODYN field aligns with that of the JGV20G02 field (labeled "JPL Survey - HAMO2") up to degree 5. The uncertainty in the field is several orders of magnitude higher than the JGV20G02 uncertainty because only data from the Survey phase of the mission were used in the GEODYN solution, whereas the JGV20G02 field made use of data from Survey through the end of the second HAMO phase. At degree 6, it can be seen that the power in the GEODYN field is an order of magnitude lower than the JGV20G02 field. This is likely because the Survey orbit, with an altitude of 2700 km was less sensitive to gravity features of degree and order higher than 5. The field computed by the Dawn Science Team using only the Survey data is also plotted (labeled "JPL Survey"). Comparing the GEODYN field to Dawn Science Team's results which only made use of the Survey data, it can be seen that there is agreement between the two fields to degree 4.

The degree-5 normal gravity field computed using GEODYN is compared with

Degree	Percent Difference in Power
2	0.05%
3	2.57%
4	4.55%
5	27.2%

Table 5.2: The percent difference between power of the GEODYN and JGV20G02 gravitational fields for degrees 2 through 5.

the *a priori* field and the JGV20G02 field in Figure 5-8. The Prime Meridian (PM) chosen for the estimation of the gravitational field and the mapping in Fig.5-8 is 74.57621°, which minimizes the differences between the shape model of Vesta and the computed landmark positions (see Konopliv [97]). This comparison is broken down from degrees 2 through 6 in Fig. 5-9. In Fig. 5-8 it can be seen that the strong J_2 component of the gravity field is represented in all three models, but that there is agreement between the tesseral features of the GEODYN and JGV20G02 fields at this degree and order, specifically, the gravity high at approximately 135°W and 0°W. The breakdown of degree and order in Fig. 5-9 shows the difference between the GEODYN and JGV20G02 fields computed at each degree and order. The differences in power of the gravitational field for each degree are shown in Table 5.2. Degrees 2 through 4 differ from JGV20G02 by less than 5%, and the percent difference at degree 5 is indicative of the Survey orbit's decreased sensitivity to finer resolution gravity features.

5.7 Conclusions

This work has demonstrated the new capability of using image constraints in GEODYN and SOLVE for precise orbit determination and gravity recovery applied to Dawn mission at Vesta. This technique is especially useful at small bodies, in non-uniform gravitational potential fields where non-conservative forces are the dominant source of error. In addition to the estimation of the potential field, this technique will aid in the determination of a reference frame for small bodies, which are be de-

Parameter	*a priori*	JGV20G02	GEODYN First 20 It. Radio Only	GEODYN First 20 It. Rad. + Img.	GEODYN 50 It. Rad. + Img.
R.A. (deg)	301 ± 5	309.03230 $\pm 3 \times 10^{-5}$	300.044 $\pm 5.1 \times 10^{-2}$	309.14 $\pm 5.1 \times 10^{-2}$	309.038 $\pm 5.1 \times 10^{-2}$
DEC. (deg)	41 ± 5	42.22618 $\pm 2 \times 10^{-5}$	45.27 $\pm 5.4 \times 10^{-2}$	42.19 $\pm 5.4 \times 10^{-2}$	42.25 $\pm 5.4 \times 10^{-2}$
L.O.D. (deg/day)	1617.33277 $\pm 7 \times 10^{-5}$	1617.3331235 $\pm 5 \times 10^{-7}$	1617.331 $\pm 3.6 \times 10^{-3}$	1617.335 $\pm 3.6 \times 10^{-3}$	1617.335 $\pm 3.6 \times 10^{-3}$
$GM/10^9$ (km^2/s^2)	17.5 $\pm 1.2 \times 10^{-5}$	17.288245 $\pm 1.2 \times 10^{-5}$	17.33015 $\pm 1.8 \times 10^{3}$	17.288515 $\pm 3.3 \times 10^{4}$	17.288316 $\pm 3.6 \times 10^{-5}$
J_2	-3.8675×10^{-2}	-3.1779×10^{-2} 1.3043×10^{-8}	-3.1802×10^{-2} 1.2×10^{-5}	-2.9502×10^{-2} 1.5×10^{-5}	-3.1796×10^{-2} 1.2×10^{-5}
C_{21}	3.0274×10^{-4}	5.3291×10^{-10} 4.9460×10^{-9}	5.3693×10^{-6} 3.6×10^{-5}	-2.5099×10^{-4} 3.6×10^{-5}	2.9420×10^{-6} 3.6×10^{-5}
C_{22}	-4.2332×10^{-3}	1.0132×10^{-3} 1.3852×10^{-8}	2.3249×10^{-3} 1.4×10^{-4}	-1.0618×10^{-3} 1.3×10^{-4}	1.0055×10^{-3} 1.3×10^{-4}
S_{21}	-1.4137×10^{-3}	-3.3873×10^{-9} 5.0173×10^{-9}	-1.8104×10^{-6} 3.7×10^{-5}	-4.5008×10^{-4} 3.6×10^{-5}	-3.3273×10^{-7} 3.7×10^{-5}
S_{22}	-4.3596×10^{-3}	4.2472×10^{-3} 4.1267×10^{-7}	3.6899×10^{-3} 1.4×10^{-4}	4.0230×10^{-3} 1.3×10^{-4}	4.2519×10^{-3} 1.3×10^{-4}
J_3	3.3660×10^{-3}	3.3106×10^{-3} 1.8895×10^{-8}	3.2295×10^{-3} 1.1×10^{-4}	-4.5491×10^{-3} 1.1×10^{-4}	3.2991×10^{-3} 1.1×10^{-4}
C_{31}	1.0437×10^{-3}	2.0456×10^{-3} 1.4254×10^{-8}	2.1833×10^{-3} 3.1×10^{-4}	4.9530×10^{-3} 2.9×10^{-4}	2.0224×10^{-3} 3.1×10^{-4}
C_{32}	1.0778×10^{-3}	6.5165×10^{-4} 9.0622×10^{-8}	-6.3036×10^{-5} 1.0×10^{-3}	2.8220×10^{-3} 9.7×10^{-4}	6.6611×10^{-4} 1.0×10^{-3}
C_{33}	6.3192×10^{-4}	2.3849×10^{-3} 3.2141×10^{-7}	2.4527×10^{-3} 2.0×10^{-3}	6.2324×10^{-3} 1.9×10^{-3}	2.6692×10^{-3} 2.0×10^{-3}
S_{31}	3.4674×10^{-4}	1.6823×10^{-3} 1.2613×10^{-7}	1.3505×10^{-3} 3.0×10^{-4}	-1.5653×10^{-3} 2.9×10^{-4}	1.5657×10^{-3} 3.0×10^{-4}
S_{32}	7.0699×10^{-4}	-1.2177×10^{-3} 9.5735×10^{-8}	-1.5892×10^{-3} 1.0×10^{-3}	2.9409×10^{-3} 9.6×10^{-4}	-1.4022×10^{-3} 1.0×10^{-3}
S_{33}	-5.0109×10^{-4}	1.5529×10^{-4} 1.0731×10^{-7}	-1.1825×10^{-3} 2.0×10^{-3}	6.9590×10^{-4} 1.9×10^{-3}	2.8994×10^{-5} 2.0×10^{-3}

Table 5.3: Vesta orientation parameters and gravity parameters from degrees 2 through 3 for the *a priori*, JGV20G02 and GEODYN gravity models, reported with 3-σ uncertainties.

Parameter	*a priori*	JGV20G02	GEODYN First 20 It. Radio Only	GEODYN First 20 It. Rad. + Img.	GEODYN 50 It. Rad. + Img.
C_{40}	5.0856×10^{-3}	3.2656×10^{-3} 3.2461×10^{-8}	1.5007×10^{-3} 8.8×10^{-4}	1.0860×10^{-1} 9.2×10^{-4}	3.2856×10^{-3} 8.8×10^{-4}
C_{41}	-1.1395×10^{-3}	-3.5434×10^{-4} 2.9433×10^{-8}	-1.7192×10^{-3} 2.0×10^{-3}	1.6565×10^{-2} 1.9×10^{-3}	-6.2543×10^{-4} 2.0×10^{-3}
C_{42}	5.0513×10^{-4}	-5.4278×10^{-4} 4.4783×10^{-8}	-3.0933×10^{-4} 5.2×10^{-3}	6.3472×10^{-3} 5.1×10^{-3}	-8.8466×10^{-4} 5.2×10^{-3}
C_{43}	2.2052×10^{-4}	-6.7001×10^{-4} 8.3297×10^{-8}	-5.1869×10^{-4} 6.1×10^{-3}	-3.4213×10^{-3} 6.1×10^{-3}	-5.9793×10^{-4} 6.1×10^{-3}
C_{44}	4.4829×10^{-4}	2.1385×10^{-4} 5.8640×10^{-8}	-8.8107×10^{-5} 6.3×10^{-3}	1.3922×10^{-3} 6.3×10^{-3}	-4.2147×10^{-5} 6.3×10^{-3}
S_{41}	1.4387×10^{-4}	-3.7032×10^{-4} 3.7835×10^{-8}	-1.6415×10^{-3} 2.0×10^{-3}	2.4165×10^{-2} 2.0×10^{-3}	-3.0910×10^{-4} 2.0×10^{-3}
S_{42}	-8.7683×10^{-5}	-4.1428×10^{-4} 5.5311×10^{-8}	8.5033×10^{-4} 5.2×10^{-3}	7.7651×10^{-3} 5.1×10^{-3}	8.1423×10^{-4} 5.2×10^{-3}
S_{43}	7.2547×10^{-4}	1.0458×10^{-4} 5.0903×10^{-8}	3.1912×10^{-4} 6.1×10^{-3}	-3.6218×10^{-3} 6.1×10^{-3}	4.3963×10^{-5} 6.1×10^{-3}
S_{44}	-2.5036×10^{-4}	2.2362×10^{-4} 1.9340×10^{-8}	-2.3376×10^{-5} 6.3×10^{-3}	1.2024×10^{-4} 6.3×10^{-3}	-1.6294×10^{-4} 6.3×10^{-3}
C_{50}	-1.8306×10^{-3}	-1.2022×10^{-3} 5.4491×10^{-8}	2.7317×10^{-5} 3.9×10^{-3}	-6.0157×10^{-2} 3.9×10^{-3}	-1.1316×10^{-3} 3.9×10^{-3}
C_{51}	-2.9318×10^{-5}	-7.7509×10^{-4} 5.6380×10^{-8}	-2.9744×10^{-4} 4.1×10^{-3}	-3.8717×10^{-4} 4.1×10^{-3}	-2.5887×10^{-4} 4.1×10^{-3}
C_{52}	-3.4238×10^{-4}	4.8372×10^{-5} 4.2034×10^{-8}	3.7382×10^{-6} 4.2×10^{-3}	-1.4076×10^{-4} 4.2×10^{-3}	5.3826×10^{-5} 4.2×10^{-3}
C_{53}	-3.8960×10^{-4}	-4.3689×10^{-4} 9.5783×10^{-8}	2.9824×10^{-5} 4.2×10^{-3}	3.4842×10^{-4} 4.2×10^{-3}	2.7221×10^{-5} 4.2×10^{-3}
C_{54}	-1.4921×10^{-4}	5.3514×10^{-4} 9.8237×10^{-8}	-1.4495×10^{-5} 4.2×10^{-3}	7.9043×10^{-5} 4.2×10^{-3}	-1.3546×10^{-5} 4.2×10^{-3}
C_{55}	3.3466×10^{-5}	6.8650×10^{-4} 5.7280×10^{-8}	-4.2044×10^{-6} 4.2×10^{-3}	2.5090×10^{-5} 4.2×10^{-3}	-2.1687×10^{-6} 4.2×10^{-3}
S_{51}	-1.0058×10^{-4}	-1.5798×10^{-4} 6.3175×10^{-8}	1.5363×10^{-3} 4.1×10^{-3}	-3.2981×10^{-2} 4.1×10^{-3}	9.3226×10^{-4} 4.1×10^{-3}
S_{52}	2.2764×10^{-4}	2.0682×10^{-4} 4.6134×10^{-8}	-3.1201×10^{-5} 4.2×10^{-3}	2.1065×10^{-3} 4.2×10^{-3}	9.5444×10^{-6} 4.2×10^{-3}
S_{53}	2.2907×10^{-4}	-6.6279×10^{-4} 6.8611×10^{-8}	-1.7721×10^{-5} 4.2×10^{-3}	1.7032×10^{-4} 4.2×10^{-3}	-1.5774×10^{-5} 4.2×10^{-3}
S_{54}	6.6800×10^{-4}	2.8256×10^{-4} 6.1578×10^{-8}	9.0053×10^{-6} 4.2×10^{-3}	4.7449×10^{-5} 4.2×10^{-3}	-7.1418×10^{-8} 4.2×10^{-3}
S_{55}	7.6729×10^{-5}	-1.0085×10^{-4} 1.6264×10^{-7}	-1.6812×10^{-6} 4.2×10^{-3}	1.9127×10^{-5} 4.2×10^{-3}	-4.4777×10^{-6} 4.2×10^{-3}

Table 5.4: Vesta gravity parameters from degrees 4 and 5 for the *a priori*, JGV20G02 and GEODYN gravity models, reported with 3-σ uncertainties.

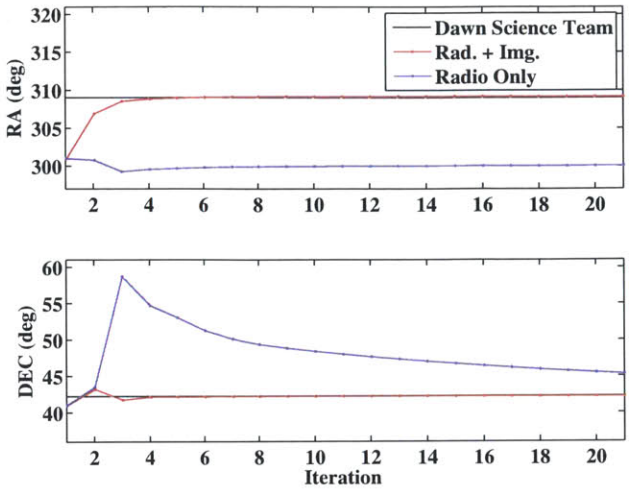

Figure 5-2: Pole convergence with and without image constraints using data from the Survey phase of the mission.

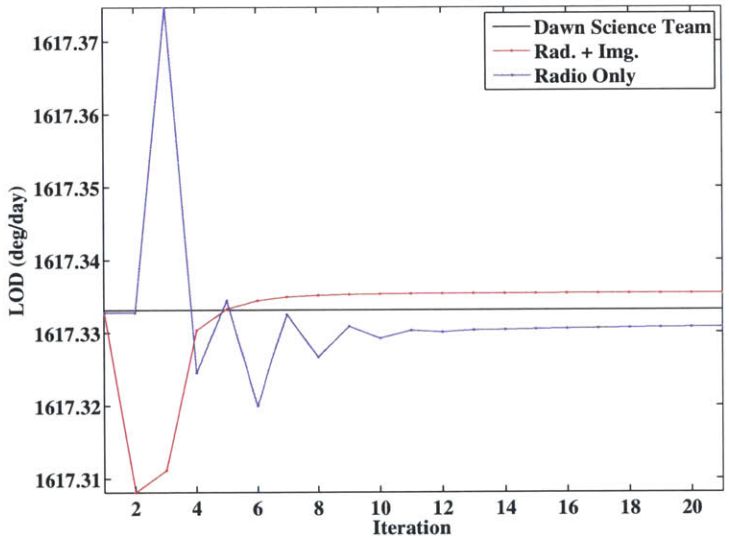

Figure 5-3: Length of day convergence with and without image constraints using data from the Survey phase of the mission.

pendent on the determination of the orientation parameters and moments of inertia of the body.

The application of image constraints improved the observability of the orientation parameters, as well as the GM and J_2 parameters of Vesta. This is because the image constraints reduce orbit uncertainty in the along- and cross-track directions, which are

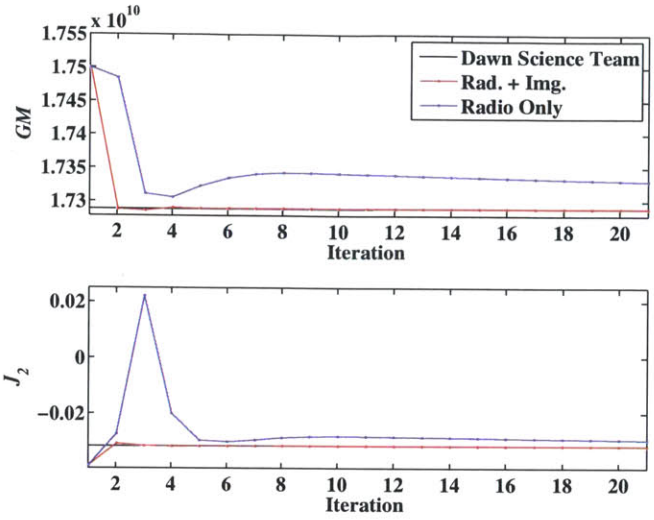

Figure 5-4: GM and J_2 convergence with and without image constraints using data from the Survey phase of the mission.

highly sensitive to the orientation parameters. When only radiometric measurements were used to determine the orientation parameters the pole declination took over 20 iterations to converge, and the right ascension stabilized at a value 9° away from that calculated by the Dawn Science Team, presented in Konopliv et al., [97].

A gravitational field of degree and order 5 was estimated after the initial estimation of the pole orientation, GM and J_2. The power of the final gravity field agreed with that of the Dawn Science Team to 0.05% at degree 2, 2.6% at degree 3, and 4.6% at degree 4. Maps of the GEODYN gravity field generally matched that estimated by the Dawn Science Team in magnitude and spatial distribution. The final pole orientation estimated by GEODYN agreed with that estimated by the Dawn Science Team to 0.1%.

These results serve to corroborate the scientific findings of Ermakov et al., [65], Fu et al., [98], and Park et al., [111]. The GEODYN estimation supports the result of a Vesta core diameter greater than 100 km when density of 7000 kg/m^3 to 8000 kg/m^3 is assumed. The current state of non-hydrostatic equilibrium is corroborated with the 99% agreement between the two models' J_2, C_{22}, and S_{22} coefficients. The degree-5 gravity map allows us to begin to see the signature of features with wavelengths on the

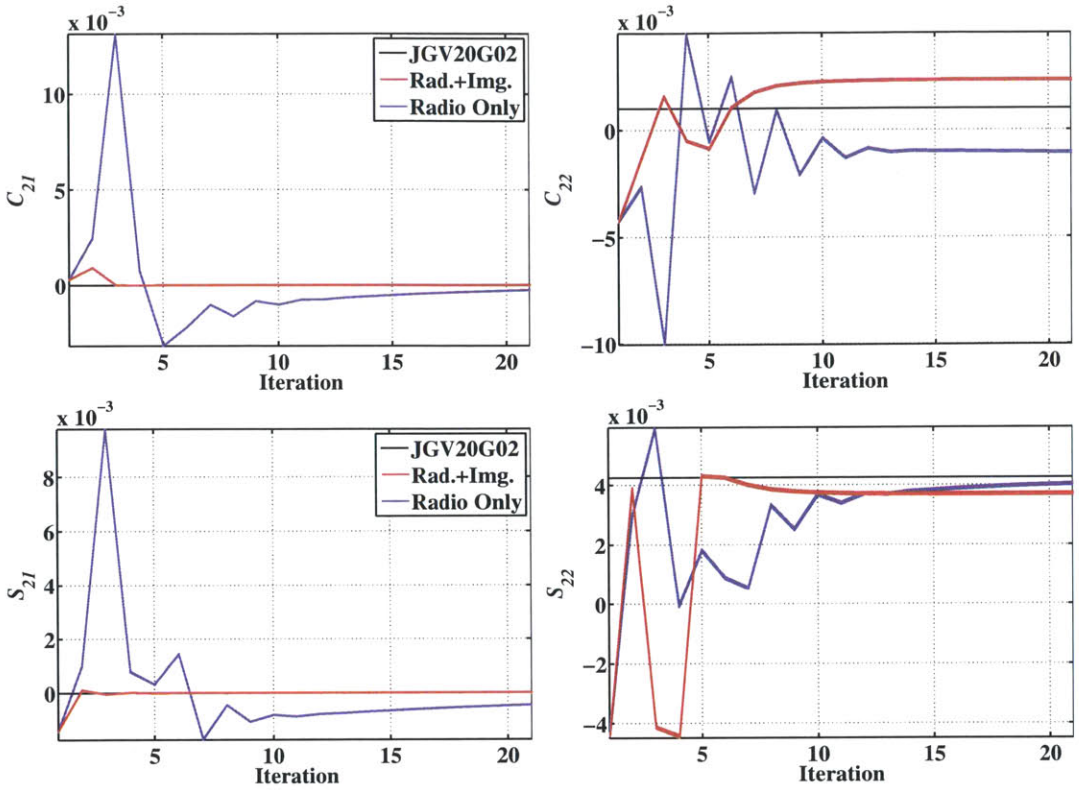

Figure 5-5: Initial convergence of the degree 2 gravity coefficients with and without the use of image constraints.

order of $\lambda \approx 300$ km, which includes Vesta's giant southern impact basins, Veneneia and Rheasilvia. These basins have diameters of 500 km and 400 km, respectively, and rim heights up to 15 km (see Schenk et al., [126]). Also visible in the GEODYN model is the gravity high close in proximity to Vestalia Terra, at approximately 135°W [127]. The investigation of these basins' age and compensation state bears heavily on the shape and gravity field of Vesta [98]. As we progress in incorporating additional data into the gravity recovery, more features will be observable in the potential field. Specifically of interest will be the rims of the giant southern basins and Rheasilvia's 10-km high central peak. Also with lower altitude data, the thickness of the mantle and crust will be observable.

The next destination of the Dawn spacecraft is the asteroid Ceres. This encounter presents an opportunity for the application of this technique at an unexplored world.

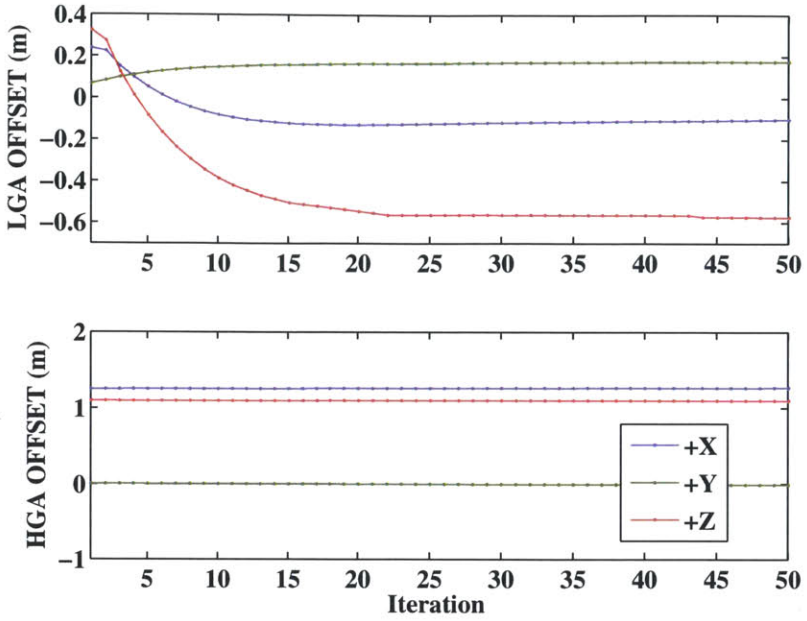

Figure 5-6: Antenna offset estimation with subsequent iterations of GEODYN and SOLVE for iterations in which orbits were allowed to fully converge in GEODYN.

At Ceres, we will use the techniques presented here to compute its pole orientation and constrain its mass. The image constraint capability of GEODYN and SOLVE will be extremely useful in this analysis, since we have no certain samples of Ceres from which to constrain the density of the core, mantle or crust. Thus any additional data types are extremely useful. The gravity recovery at Ceres will aid in constraining the size and density of the core, and the thickness and density of mantle. It will also inform the discussion on the amount of ice and volatiles present. Finally, this new capability for the GEODYN and SOLVE software has applications on several other missions. In addition, the new capability will be applicable to many other missions which use or have used optical data such as NEAR and OSIRIS-REx [11], [84].

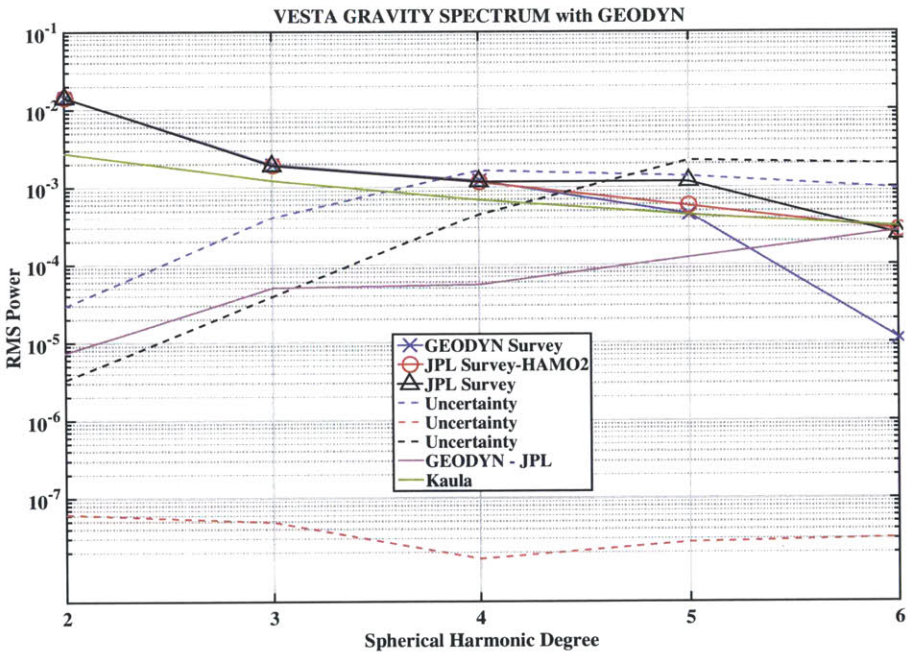

Figure 5-7: Gravity power spectrum calculated with Survey data. The Kaula power law shown is referenced in Eqn. 5.2. Here it can be seen that the power in the GEODYN field aligns with that of the JGV20G02 field (labeled "JPL Survey - HAMO2") up to degree 5. The field computed by the Dawn Science Team using only the Survey data is also plotted (labeled "JPL Survey").

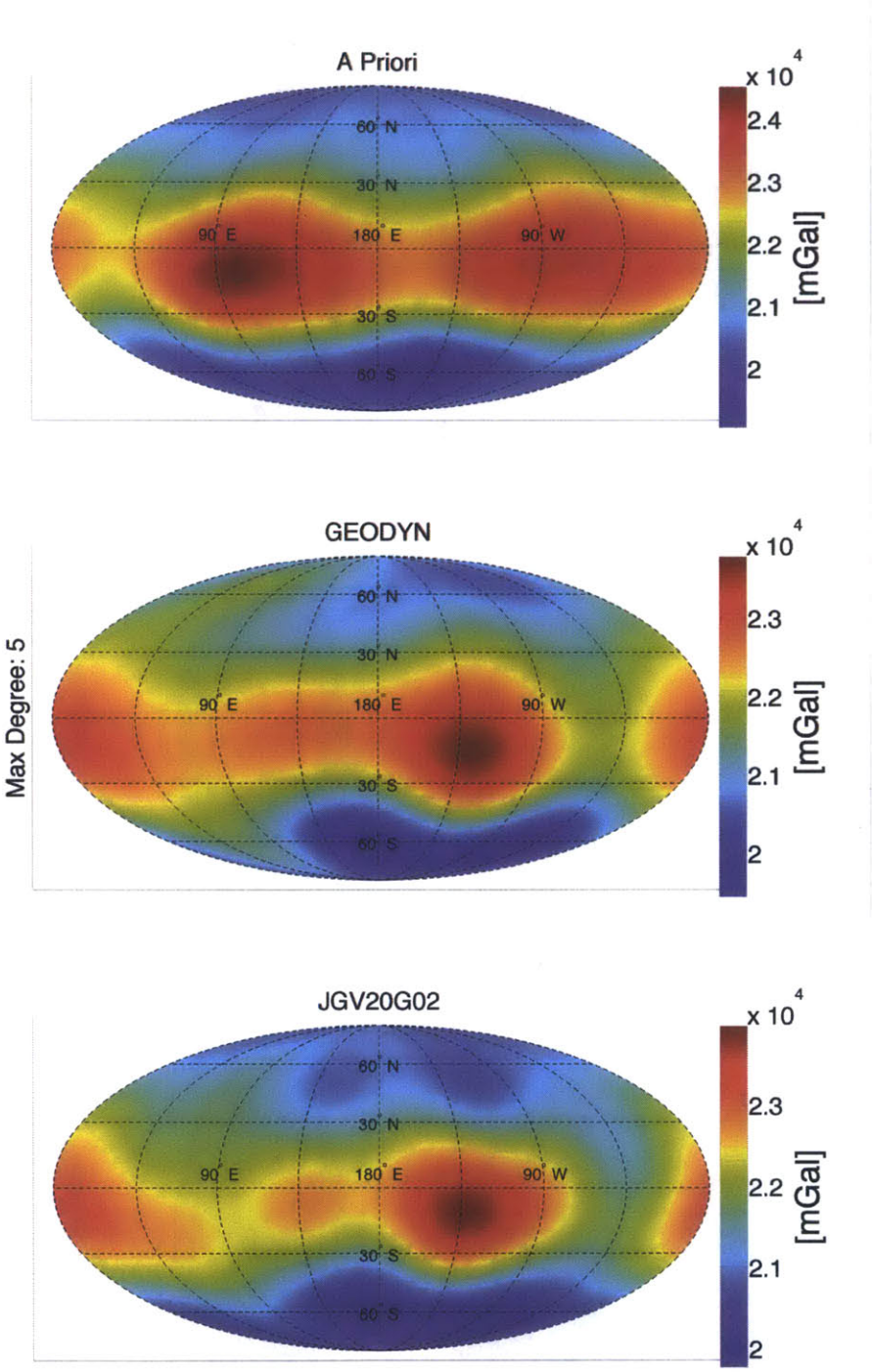

Figure 5-8: Degree and order 5 normal gravitational fields estimated using the Survey data in GEODYN, using Survey-HAMO2 data represented in the JGV20G02 field, and using photometric data from the Hubble Space Telescope in the *a priori* gravity model.

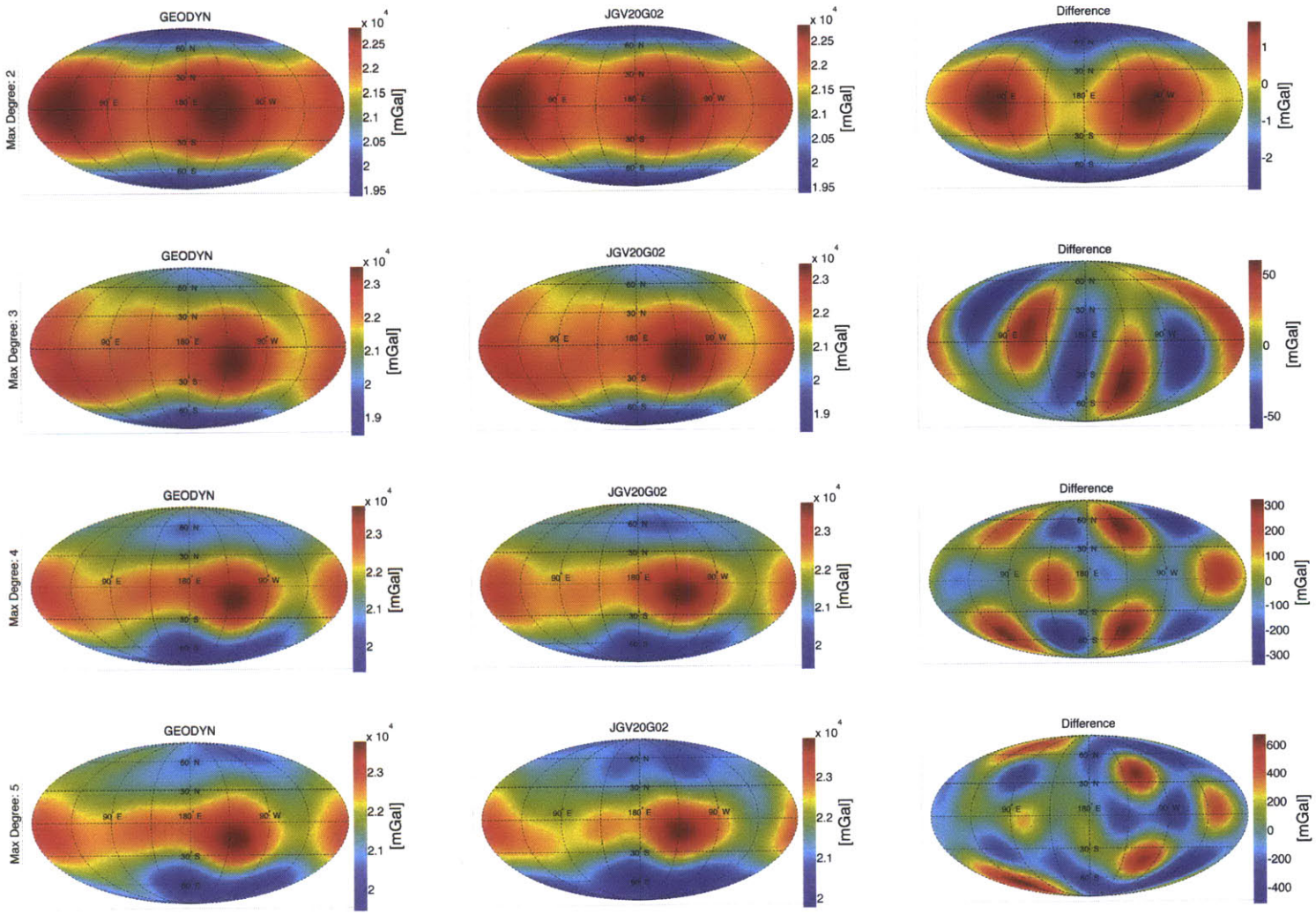

Figure 5-9: Degree and order 2-6 normal gravitational fields estimated using the Survey data, and their difference with the JGV20G02 gravity field.

Chapter 6

Conclusions and Future Endeavors

The work presented in this thesis illustrated two examples of applications of new geodetic techniques in geophysics. Both enhance the geophysical results that can be realized. In addition, because they can both aid in gravimetric surveys and planetary gravity modeling, they can aid other branches of science, since gravity modeling aids in the definition of reference frames to which other datasets are registered.

6.1 GPS Positioning

Applying a smoothed ionospheric model to GPS measurements was shown to decrease the noise in the positions computed. For both the seismological study and the airborne gravimetry investigation presented here, GPS height measurement noise was reduced. For seismology, this means that surface dynamics were more visible in GPS position time histories, generally in the horizontal components, and after the major surface wave arrivals dissipated. Dynamics in the height component were still difficult to observe, but the fact that treating the ionosphere has the greatest effect in the vertical dimension suggests this is a promising avenue of improvement for future studies.

For airborne gravimetry, the reduction in positioning noise resulted in a higher repeatability for subsequently-flown gravity profiles. A 0.6-mGal improvement in repeatability in an RMS sense was observed when filter parameters were chosen judiciously. The dataset studied for this work was a calibration survey carried out for the

NOAA GRAV-D project, which aims to refine the vertical datum for the entire U.S. and its territories. Improvements to the potential field will result in more accurate maps of flood plains, drainages, and coastal areas. Application of this technique on the GRAV-D project is also important because the improved accuracy of the orthometric terrain heights will result in more accurate registration of datasets for which GPS is used.

The ionospheric modeling technique presented here will continue to improve differential GPS uncertainties as we approach solar minimum. As the ionosphere becomes less active, it will be easier to isolate and filter the noise inherent in the GPS phase observables while preserving the effect of this ionosphere.

Further steps to be taken in ionospheric modeling applied to GPS could be the creation of local ionospheric models using estimates of the TEC from GPS line of sight signals. These models could result in improved ambiguity resolution while providing local models of the ionosphere, which would be of interest from a space physics perspective.

As ionospheric modeling improves, GPS positioning will improve. For seismology, this could eventually mean detection and observation of arrivals that have been in the past difficult with GPS techniques, such as the initial P- and S-waves, which have amplitudes approximately an order of magnitude smaller than the surface wave amplitudes. For airborne gravity, it will result in the improved modeling of local gravity anomalies, as well as registration of other datasets.

6.2 Orbit Determination and Gravity Recovery with Image Constraints

Utilizing constraints from spacecraft image data has been shown to improve orbit determination and gravity recovery capabilities. This was the first time image constraints were utilized in NASA/GSFC's GEODYN orbit determination and parameter estimation software. The new data type performed as expected in that GEODYN

was able to estimate a stable orbit and gravity field, while reducing the residual RMS of the image constraints to smaller than the size of the pixel scale of the images.

In terms of orbit determination, this technique can be especially useful for navigation teams who might typically rely on radiometric range and Doppler measurements. The application of this technique has been shown to provide constraints on the orbit in the along- and cross-track directions; it complements the radiometric measurements, which have the majority of their affect on the radial orbit component.

This technique was further employed to estimate the orientation parameters and low-degree gravity field of Vesta. It was shown that without image constraints, and starting with a realistic *a priori* knowledge of the Vesta orientation and gravity field, it was impossible to estimate the orientation parameters of Vesta. When the image constraints were used, the orientation parameters converged to a pole orientation that agrees with that estimated by the Dawn Science Team, who used the same data, but a different orbit and geophysical estimation algorithm. In addition to the refinement of the pole, the gravity field up to degree and order 5, when computed using image data, showed agreement with the gravity model produced by the Dawn Science Team in magnitude and spatial distribution.

This technique has possible application on several current missions and will be useful as NASA plans more missions to small bodies, and challenging space environments. Most apparently, this includes the Dawn mission to Ceres, as the spacecraft will arrive in the spring of 2015. Another potential application of planetary navigation with spacecraft imagery will be on the OSIRIS-REx mission, that aims to collect a sample from the Near Earth Object (NEO) 101955 Bennu in 2019. NASA currently has plans to investigate NEOs with human crews. Any robotic scouts sent to NEOs before the arrival of humans will likely utilize optical techniques to define reference frames and estimate the gravity fields of these bodies. Finally, future missions proposed to the moons of the outer solar system will likely have high-resolution camera payloads and will benefit from optical orbit determination, due to the challenges of using radiometric data from Earth in the dynamic gravity environments in which they will operate.

6.3 Conclusion

The techniques presented in this dissertation were shown to improve scientific capabilities for terrestrial and planetary investigations. There is a great potential for their future application. As new scenarios for the employment of ionospheric modeling and optical spacecraft navigation are encountered, these techniques will be further refined. In this process, they will help maximize the scientific output of GPS-based terrestrial investigations and planetary geophysics.

Bibliography

[1] J. R. Dempsey, W. A. Davis, A. S. C. and Williams, W. C., "Program Management in Design and Development," *Third Annual Aerospace Reliability and Maintainability Conference*, Society of Automotive Engineers, 1964.

[2] Leick, A., *GPS satellite surveying*, John Wiley & Sons, 2004.

[3] Herring, T. A., King, R., and McClusky, S., *GAMIT Reference Manual: GPS Analysis at MIT*, Department of Earth, Atmospheric and Planetary Sciences, Massachusetts Institute of Technology, 10th ed., October 2010.

[4] Bilich, A., Cassidy, J. F., and Larson, K. M., "GPS seismology: application to the 2002 Mw 7.9 Denali fault earthquake," *Bulletin of the Seismological Society of America*, Vol. 98, No. 2, 2008, pp. 593–606.

[5] Bock, Y., Nikolaidis, R. M., Jonge, P. J., and Bevis, M., "Instantaneous geodetic positioning at medium distances with the Global Positioning System," *Journal of Geophysical Research: Solid Earth (1978–2012)*, Vol. 105, No. B12, 2000, pp. 28223–28253.

[6] Wanninger, L., "The performance of virtual reference stations in active geodetic GPS-networks under solar maximum conditions," Vol. 99, 1999, pp. 1419–1427.

[7] Langley, R. B., "The GPS error budget," *GPS world*, Vol. 8, No. 3, 1997, pp. 51–56.

[8] Geng, J., Bock, Y., Melgar, D., Crowell, B. W., and Haase, J. S., "A new seismogeodetic approach applied to GPS and accelerometer observations of the 2012 Brawley seismic swarm: Implications for earthquake early warning," *Geochemistry, Geophysics, Geosystems*, Vol. 14, No. 7, 2013, pp. 2124–2142.

[9] Baumann, H., Klingelé, E. E., and Marson, I., "Absolute airborne gravimetry: a feasibility study," *Geophysical Prospecting*, Vol. 60, No. 2, 2012, pp. 361–372.

[10] Pavlis, D., Poulose, S. G., and McCarthy, J. J., "GEODYN Operations Manuals," Tech. rep., SGT Inc., Contractor Report, Greenbelt, MD, 2006.

[11] Owen, W., Wang, T., Harch, A., Bell, M., and Peterson, C., "NEAR Optical Navigation at Eros," *Advances in the Astronautical Sciences*, Vol. 109, 2001, pp. 1075–1090.

[12] Mazarico, E., "Selenodesy with LRO: Radio Tracking and Altimetric Crossovers to Improve Orbit Knowledge and Gravity Field Estimation," *42nd Lunar and Planetary Science Conference*, 2011.

[13] Gaskell, R. W., Palmer, E. E., Mastrodemos, N., Barnouin, O. S., Jorda, L., and Taylor, A. H., "Mercury and Vesta - Preliminary shape and topography," No. Poster P41A-1576, presented at Fall Meeting, AGU, San Fancisco, CA, December 2011.

[14] Konopliv, S., A., Asmar, S. W., Park, R. S., Bills, B. G., Centinello, F., Chamberlin, A. B., Ermakov, A., Gaskell, R. W., Rambaux, N., Raymond, C. A., Russell, C. T., Smith, D. E., Tricarico, P., and Zuber, M. T., "The Vesta Gravity Field, Spin Pole and Rotation Period, Landmark Positions, and Ephemeris from the Dawn Tracking and Optical Data," *Icarus*, Vol. 0, No. 0, 2013, pp. –.

[15] Cowell, P. and Crommelin, A., "Investigation of the Motion of Halley's Comet from 1759 to 1910," *Greenwich Observations in Astronomy, Magnetism and Meteorology made at the Royal Observatory, Series 2*, Vol. 71, 1911, pp. 1.

[16] Moyer, T. D., "Mathematical Formulation of the Double-Precision Orbit Determination Program (DPODP)," Tech. rep., NASA Jet Propulsion Laboratory, California Institute of Technology, Pasadena, California, 1971.

[17] Chen, J. L. and Wilson, C. R., "Low degree gravitational changes from earth rotation and geophysical models," *Geophysical Research Letters*, Vol. 30, No. 24, 2003, pp. n/a–n/a.

[18] Andrews-Hanna, J. C., Asmar, S. W., Head, J. W., Kiefer, W. S., Konopliv, A. S., Lemoine, F. G., Matsuyama, I., Mazarico, E., McGovern, P. J., and Melosh, H. J., "Ancient igneous intrusions and early expansion of the Moon revealed by GRAIL gravity gradiometry," *Science*, Vol. 339, No. 6120, 2013, pp. 675–678.

[19] Avallone, A., Marzario, M., Cirella, A., Piatanesi, A., Rovelli, A., Di Alessandro, C., D'Anastasio, E., D'Agostino, N., Giuliani, R., and Mattone, M., "Very high rate (10 Hz) GPS seismology for moderate-magnitude earthquakes: The case of the Mw 6.3 L'Aquila (central Italy) event," *Journal of Geophysical Research: Solid Earth*, Vol. 116, No. B2, 2011, pp. B02305.

[20] Zheng, Y., Li, J., Xie, Z., and Ritzwoller, M. H., "5Hz GPS seismology of the El Mayor–Cucapah earthquake: estimating the earthquake focal mechanism," *Geophysical Journal International*, Vol. 190, No. 3, 2012, pp. 1723–1732.

[21] Grewal, M. S., Weill, L. R., and Andrews, A. P., *Global Positioning Systems, Inertial Navigation, and Integration*, John Wiley and Sons, 2007.

[22] Leick, A., *GPS satellite surveying*, Wiley. com, 2004.

[23] Schaer, S., Gurtner, W., and Feltens, J., "IONEX: The ionosphere map exchange format version 1," Vol. 9, 1998.

[24] Hernández-Pajares, M., Juan, J., Sanz, J., Orus, R., Garcia-Rigo, A., Feltens, J., Komjathy, A., Schaer, S., and Krankowski, A., "The IGS VTEC maps: a reliable source of ionospheric information since 1998," *Journal of Geodesy*, Vol. 83, No. 3-4, 2009, pp. 263–275.

[25] Klobuchar, J. A., "Ionospheric time-delay algorithm for single-frequency GPS users," *Aerospace and Electronic Systems, IEEE Transactions on*, , No. 3, 1987, pp. 325–331.

[26] Spencer, P. S., Robertson, D. S., and Mader, G. L., "Ionospheric data assimilation methods for geodetic applications," IEEE, 2004, pp. 510–517.

[27] IS-GPS-200, "Global Positioning Systems Directorate Systems Engineering & Integration Interface Specification," Tech. rep., Navstar GPS Space Segment/Navigation User Interfaces, Navstar GPS Space Segment/Navigation User Interfaces, September 2012.

[28] Herring, T., King, R., and McClusky, S., "GAMIT Reference Manual–Release 10.4.28," *Department of Earth, Atmospheric, and Planetary Sciences Massachussetts Institute of Technology*, 2010.

[29] Dong, D.-N. and Bock, Y., "Global Positioning System Network analysis with phase ambiguity resolution applied to crustal deformation studies in California," *Journal of Geophysical Research: Solid Earth*, Vol. 94, No. B4, 1989, pp. 3949–3966.

[30] Jackson, J. D. and Fox, R. F., "Classical electrodynamics," *American Journal of Physics*, Vol. 67, No. 9, 1999, pp. 841–842.

[31] Bock, Y., Gourevitch, S. A., Counselman III, C. C., King, R. W., and Abbot, R. I., "Interferometric analysis of GPS phase observations," *Manuscripta geodaetica*, Vol. 11, 1986, pp. 282–288.

[32] Crassidis, J. L. and Junkins, J. L., *Optimal estimation of dynamic systems*, Vol. 24, Chapman & Hall, 2011.

[33] Bock, Y., "Continuous monitoring of crustal deformation," *GPS World*, Vol. 2, No. 6, 1991, pp. 40–47, n/a.

[34] Choi, K., Bilich, A., Larson, K. M., and Axelrad, P., "Modified sidereal filtering: Implications for high-rate GPS positioning," *Geophysical research letters*, Vol. 31, No. 22, 2004, pp. L22608.

[35] Wei, S., Fielding, E., Leprince, S., Sladen, A., Avouac, J.-P., Helmberger, D., Hauksson, E., Chu, R., Simons, M., and Hudnut, K., "Superficial simplicity of the 2010 El Mayor-Cucapah earthquake of Baja California in Mexico," *Nature geoscience*, Vol. 4, No. 9, 2011, pp. 615–618.

[36] Oskin, M. E., Arrowsmith, J. R., Corona, A. H., Elliott, A. J., Fletcher, J. M., Fielding, E. J., Gold, P. O., Garcia, J. J. G., Hudnut, K. W., and Liu-Zeng, J., "Near-field deformation from the El Mayor–Cucapah earthquake revealed by differential LIDAR," *Science*, Vol. 335, No. 6069, 2012, pp. 702–705.

[37] Hauksson, E., Stock, J., Hutton, K., Yang, W., Vidal-Villegas, J. A., and Kanamori, H., "The 2010 M w 7.2 El Mayor-Cucapah Earthquake Sequence, Baja California, Mexico and Southernmost California, USA: Active Seismotectonics along the Mexican Pacific Margin," *Pure and Applied Geophysics*, Vol. 168, No. 8-9, 2011, pp. 1255–1277.

[38] Hauksson, E., Small, P., Hafner, K., Busby, R., Clayton, R., Goltz, J., Heaton, T., Hutton, K., Kanamori, H., and Polet, J., "Southern California Seismic Network: Caltech/USGS Element of TriNet 1997-2001," *Seismological Research Letters*, Vol. 72, No. 6, 2001, pp. 690–704.

[39] Crotwell, H. P., Owens, T. J., and Ritsema, J., "The TauP Toolkit: Flexible seismic travel-time and ray-path utilities," *Seismological Research Letters*, Vol. 70, No. 2, 1999, pp. 154–160.

[40] Berger, J., Baker, L., Brune, J., Fletcher, J., Hanks, T., and Vernon, F., "The Anza array: A high-dynamic-range, broadband, digitally radiotelemetered seismic array," *Bulletin of the Seismological Society of America*, Vol. 74, No. 4, 1984, pp. 1469–1481.

[41] Shapiro, N. M., Campillo, M., Stehly, L., and Ritzwoller, M. H., "High-resolution surface-wave tomography from ambient seismic noise," *Science*, Vol. 307, No. 5715, 2005, pp. 1615–1618.

[42] Sabra, K. G., Gerstoft, P., Roux, P., Kuperman, W., and Fehler, M. C., "Surface wave tomography from microseisms in Southern California," *Geophysical Research Letters*, Vol. 32, No. 14, 2005.

[43] Bruton, A., Schwarz, K., Ferguson, S., Kern, M., and Wei, M., "Deriving Acceleration from DGPS: Toward Higher Resolution Applications of Airborne Gravimetry," *GPS Solutions*, Vol. 5, No. 3, 2002, pp. 1–14.

[44] Damiani, T. and Youngman, M., *GRAV-D General Airborne Gravity Data User Manual*, NOAA/National Geodetic Survey, 2013.

[45] Bruton, A. M., *Improving the accuracy and resolution of SINS/DGPS airborne gravimetry*, University of Calgary Calgary, Alberta, 2000.

[46] Anthes, R. A., Ector, D., Hunt, D., Kuo, Y., Rocken, C., Schreiner, W., Sokolovskiy, S., Syndergaard, S., Wee, T., and Zeng, Z., "The COSMIC/FORMOSAT-3 mission: Early results," *Bulletin of the American Meteorological Society*, Vol. 89, No. 3, 2008, pp. 313–333.

[47] Bilitza, D., "International Reference Ionosphere 2000," *Radio Science*, Vol. 36, No. 2, 2001, pp. 261–275.

[48] Hysell, D., "Inverting ionospheric radio occultation measurements using maximum entropy," *Radio Science*, Vol. 42, No. 4, 2007.

[49] Grewal, M., Weill, L., and Andrews, A., *Global Positioning Systems, Inertial Navigation, and Integration*, John Wiley & Sons, Inc., New York, New York, 2001.

[50] Damiani, T., Bilich, A., and Mader, G., "Aircraft Positioning for Airborne Gravimetry: GRAV-D's' Kinematic GPS Processing Challenge'," Vol. 1, 2013, p. 08.

[51] "GRACE: Gravity Recovery and Climate Experiment," Center for Space Research, University of Texas at Austin, `http://www.csr.utexas.edu/grace/`, August 2011.

[52] Pavlis, N. K., Holmes, S. A., Kenyon, S. C., and Factor, J. K., "The development and evaluation of the Earth Gravitational Model 2008 (EGM2008)," *Journal of Geophysical Research: Solid Earth (1978–2012)*, Vol. 117, No. B4, 2012.

[53] Peters, M. and Brozena, J., "Methods to improve existing shipboard gravimeters for airborne gravimetry," Vol. 4, 1995, pp. 39–45.

[54] Micro-g LaCoste, 1401 Horizon Ave., Lafayette, CO 80026, *TAGS Air II Gravity Meter*.

[55] Damiani, T. M., *GRAV-D General Airborne Gravity Data User Manual*, NOAA/National Geodetic Survey, 1315 East-West Highway, Silver Spring, MD, August 2011.

[56] g LaCoste, M., "TAGS Turnkey Airborne Gravity System AIRIII Hardware and Operations Manual," 2010.

[57] Mostafa, M., Hutton, J., and Reid, B., "GPS/IMU products-the Applanix approach," Vol. 1, 2001, pp. 63–83.

[58] Damiani, T., "Gravity Disturbances at Altitude and at the Surface," Vol. 1, 2013, p. 0908.

[59] Preaux, S. and Damiani, T., "Quantification of Computational Error in Various Calculation Methods of Gravity Disturbances at Altitude and the Surface using EGM2008 Grids," Vol. 1, 2013, p. 0907.

[60] Heiskanen, W. A. and Moritz, H., "Physical geodesy," *Bulletin Géodésique (1946-1975)*, Vol. 86, No. 1, 1967, pp. 491–492.

[61] Hackney, R. and Featherstone, W., "Geodetic versus geophysical perspectives of the 'gravity anomaly'," *Geophysical Journal International*, Vol. 154, No. 1, 2003, pp. 35–43.

[62] Harlan, R. B., "Eotvos corrections for airborne gravimetry," *Journal of Geophysical Research*, Vol. 73, No. 14, 1968, pp. 4675–4679.

[63] Childers, V. A., Bell, R. E., and Brozena, J. M., "Airborne gravimetry: An investigation of filtering," *Geophysics*, Vol. 64, No. 1, 1999, pp. 61–69.

[64] Brozena, J., Mader, G., and Peters, M., "Interferometric Global Positioning System: Threedimensional positioning source for airborne gravimetry," *Journal of Geophysical Research: Solid Earth (1978–2012)*, Vol. 94, No. B9, 1989, pp. 12153–12162.

[65] Ermakov, A. I., Zuber, M. T., Smith, D. E., Raymond, C. A., Balmino, G., Fu, R. R., and Ivanov, B. A., "Constraints on Vesta's interior structure using gravity and shape models from the Dawn mission," *Icarus*, Vol. 240, No. 0, 9 2014, pp. 146–160.

[66] Mazarico, E., Rowlands, D., Neumann, G., Torrence, M., Smith, D., and Zuber, M., "Selenodesy with LRO: Radio Tracking and Altimetric Crossovers to Improve Orbit Knowledge and Gravity Field Estimation: Radio Tracking and Altimetric Crossovers to Improve Orbit Knowledge and Gravity Field Estimation," Vol. 42, March 2011, p. 2215.

[67] Mazarico, E., Rowlands, D. D., Neumann, G. A., Smith, D. E., Torrence, M. H., Lemoine, F. G., and Zuber, M. T., "Orbit Determination of the Lunar Reconnaissance Orbiter," *Journal of Geodesy*, Vol. 86, No. 3, 2012, pp. 193–207.

[68] Rowlands, D., Lemoine, F., Chinn, D., and Luthcke, S., "A Simulation Study of Multi-Beam Altimetry for Lunar Reconnaissance Orbiter and Other Planetary Missions," *Journal of Geodesy*, Vol. 83, No. 8, 2009, pp. 709–721.

[69] Lemoine, F. G., Smith, D. E., Rowlands, D. D., Zuber, M. T., Neumann, G. A., Chinn, D. S., and Pavlis, D. E., "An Improved Solution of the Gravity Field of Mars (Gmm-2b) from Mars Global Surveyor," *Journal of Geophysical Research: Planets*, Vol. 106, No. E10, 2001, pp. 23359–23376.

[70] Tapley, B. D., Bettadpur, S., Watkins, M., and Reigber, C., "The Gravity Recovery and Climate Experiment: Mission Overview and Early Results," *Geophysical Research Letters*, Vol. 31, No. 9, 2004, pp. L09607.

[71] Goossens, S., Matsumoto, K., Rowlands, D., Lemoine, F., Noda, H., and Araki, H., "Orbit determination of the SELENE satellites using multi-satellite data types and evaluation of SELENE gravity field models," *Journal of Geodesy*, Vol. 85, No. 8, 2011, pp. 487–504.

[72] Zuber, M. T., Smith, D. E., Watkins, M. M., Asmar, S. W., Konopliv, A. S., Lemoine, F. G., Melosh, H. J., Neumann, G. A., Phillips, R. J., and Solomon, S. C., "Gravity field of the Moon from the Gravity Recovery and Interior Laboratory (GRAIL) mission," *Science*, Vol. 339, No. 6120, 2013, pp. 668–671.

[73] Bloch, J. and Rast, R., "Space Surveillance One Photon at a Time," *Advanced Maui Optical and Space Surveillance Technologies Conference*, Provided by the SAO/NASA Astrophysics Data System, Maui, HI., 2007.

[74] DeMars, K. J. and Jah, M. K., "Probabilistic Initial Orbit Determination Using Gaussian Mixture Models," *Journal of Guidance, Control, and Dynamics*, Vol. 36, No. 5, 2014/02/03 2013, pp. 1324–1335.

[75] Bianco, G., Chersich, M., Devoti, R., Luceri, V., and Selden, M., "Measurement of LAGEOS-2 Rotation by Satellite Laser Ranging Observations," *Geophysical Research Letters*, Vol. 28, No. 10, 2001, pp. 2113–2116.

[76] Zuber, M. T., Smith, D. E., Zellar, R. S., Neumann, G. A., Sun, X., Katz, R. B., Kleyner, I., Matuszeski, A., McGarry, J. F., and Ott, M. N., "The Lunar Reconnaissance Orbiter Laser Ranging Investigation," *Space science reviews*, Vol. 150, No. 1-4, 2010, pp. 63–80.

[77] Konopliv, A. S., Miller, J. K., Owen, W. M., Yeomans, D. K., Giorgini, J. D., Garmier, R., and Barriot, J.-P., "A Global Solution for the Gravity Field, Rotation, Landmarks, and Ephemeris of Eros," *Icarus*, Vol. 160, No. 2, 2002, pp. 289–299.

[78] Gaskell, R., Barnouin-Jha, O., Scheeres, D., Konopliv, A., Mukai, T., Abe, S., Saito, J., Ishiguro, M., Kubota, T., and Hashimoto, T., "Characterizing and Navigating Small Bodies with Imaging Data," *Meteoritics & Planetary Science*, Vol. 43, No. 6, 2008, pp. 1049–1061.

[79] Raymond, C., Jaumann, R., Nathues, A., Sierks, H., Roatsch, T., Preusker, F., Scholten, F., Gaskell, R., Jorda, L., and Keller, H.-U., *The Dawn Topography Investigation*, Springer, 2012, pp. 487–510.

[80] Konopliv, A., Asmar, S., Bills, B., Mastrodemos, N., Park, R., Raymond, C., Smith, D., and Zuber, M., *The Dawn Gravity Investigation at Vesta and Ceres*, Springer, 2012, pp. 461–486.

[81] Thomas, V. C., Makowski, J. M., Brown, G. M., McCarthy, J. F., Bruno, D., Cardoso, J. C., Chiville, W. M., Meyer, T. F., Nelson, K. E., and Pavri, B. E., *The Dawn Spacecraft*, Springer, 2012, pp. 175–249.

[82] Kirk, R. L., Howington-Kraus, E., Rosiek, M. R., Anderson, J. A., Archinal, B. A., Becker, K. J., Cook, D. A., Galuszka, D. M., Geissler, P. E., Hare, T. M., Holmberg, I. M., Keszthelyi, L. P., Redding, B. L., Delamere, W. A., Gallagher, D., Chapel, J. D., Eliason, E. M., King, R., and McEwen, A. S.,

"Ultrahigh Resolution Topographic Mapping of Mars with Mro Hirise Stereo Images: Meter-Scale Slopes of Candidate Phoenix Landing Sites," *Journal of Geophysical Research: Planets*, Vol. 113, No. E3, 2008, pp. n/a–n/a.

[83] Robinson, M. S., Brylow, S. M., Tschimmel, M., Humm, D., Lawrence, S. J., Thomas, P. C., Denevi, B. W., Bowman-Cisneros, E., Zerr, J., Ravine, M. A., Caplinger, M. A., Ghaemi, F. T., Schaffner, J. A., Malin, M. C., Mahanti, P., Bartels, A., Anderson, J., Tran, T. N., Eliason, E. M., McEwen, A. S., Turtle, E., Jolliff, B. L., and Hiesinger, H., "Lunar Reconnaissance Orbiter Camera (LROC) Instrument Overview," Vol. 150, No. 1-4, 2010, pp. 81–124.

[84] Smith, P., Rizk, B., Kinney-Spano, E., Fellows, C., d'Aubigny, C., and Merrill, C., "The OSIRIS-REx Camera Suite (OCAMS))," *LPI Contributions*, Vol. 1719, 2013, pp. 1690.

[85] Gaskell, R., Barnouin-Jha, O., Scheeres, D., Mukai, T., Hirata, N., Abe, S., Saito, J., Ishiguro, M., Kubota, T., Hashimoto, T., Kawaguchi, J., Yoshikawa, M., Shirakawa, K., and Kominato, T., *Landmark Navigation Studies and Target Characterization in the Hayabusa Encounter with Itokawa*, American Institute of Aeronautics and Astronautics, April 2006.

[86] Brouwer, D. and Clemence, G. M., *Numerical Integration of Orbits*, Academic Press, New York, NY, 1961, pp. 167–187.

[87] Moyer, T. D., "Transformation from proper time on Earth to coordinate time in solar system barycentric space-time frame of reference," *Celestial Mechanics*, Vol. 23, No. 1, 1981, pp. 33–56.

[88] Moyer, T. D., *Formulation for Observed and Computed Values of Deep Space Network Data Types for Navigation*, Vol. 3, John Wiley & Sons, 2005.

[89] Lemoine, F. G., Goossens, S., Sabaka, T. J., Nicholas, J. B., Mazarico, E., Rowlands, D. D., Loomis, B. D., Chinn, D. S., Caprette, D. S., and Neumann, G. A., "Highdegree Gravity Models from Grail Primary Mission Data," *Journal of Geophysical Research: Planets*, Vol. 118, No. 8, 2013, pp. 1676–1698.

[90] Zuber, M. T., Lemoine, F. G., Smith, D. E., Konopliv, A. S., Smrekar, S. E., and Asmar, S. W., "Mars Reconnaissance Orbiter Radio Science Gravity Investigation," *Journal of Geophysical Research: Planets*, Vol. 112, No. E5, 2007, pp. n/a–n/a.

[91] Mazarico, E., Genova, A., Goossens, S., Lemoine, F., Smith, D., Zuber, M., Neumann, G., and Solomon, S., "The gravity field of Mercury from MESSENGER," Vol. 45, 2014, p. 1863.

[92] Gaskell, R. W., "SPC shape and topography of Vesta from DAWN imaging data," Vol. 44, 2012.

[93] Owen Jr, W. M., "Methods of Optical Navigation," 21st AAS/AIAA Space Flight Mechanics Meeting, AAS Paper 11-215, New Orleans, LA, 2011.

[94] McMahon, S. K., "Overview of the Planetary Data System," *Planetary and Space Science*, Vol. 44, No. 1, 1996, pp. 3–12.

[95] Acton Jr, C. H., "Ancillary Data Services of Nasa's Navigation and Ancillary Information Facility," *Planetary and Space Science*, Vol. 44, No. 1, 1996, pp. 65–70.

[96] Sierks, H., Keller, H., Jaumann, R., Michalik, H., Behnke, T., Bubenhagen, F., Büttner, I., Carsenty, U., Christensen, U., and Enge, R., "The Dawn Framing Camera," *Space Science Reviews*, Vol. 163, No. 1-4, 2011, pp. 263–327.

[97] Konopliv, A., Asmar, S., Park, R., Bills, B., Centinello, F., Chamberlin, A., Ermakov, A., Gaskell, R., Rambaux, N., and Raymond, C., "The Vesta Gravity Field, Spin Pole and Rotation Period, Landmark Positions, and Ephemeris from the Dawn Tracking and Optical Data," *Icarus*, 2013.

[98] Fu, R. R., Hager, B. H., Ermakov, A. I., and Zuber, M. T., "Efficient early global relaxation of asteroid Vesta," *Icarus*, 2014.

[99] Russell, C., Capaccioni, F., Coradini, A., De Sanctis, M., Feldman, W., Jaumann, R., Keller, H., McCord, T., McFadden, L., and Mottola, S., "Dawn Mission to Vesta and Ceres," *Earth, Moon, and Planets*, Vol. 101, No. 1-2, 2007, pp. 65–91.

[100] Bottke, W. F., *Asteroids III*, University of Arizona Press, 2002.

[101] De Pater, I. and Lissauer, J. J., *Planetary sciences*, Cambridge University Press, 2010.

[102] Gradie, J. and Tedesco, E., "Compositional structure of the asteroid belt," *Science*, Vol. 216, No. 4553, 1982, pp. 1405–1407.

[103] Chambers, J. E., "Planetary accretion in the inner Solar System," *Earth and Planetary Science Letters*, Vol. 223, No. 3, 2004, pp. 241–252.

[104] McCord, T. B., McFadden, L. A., Russell, C. T., Sotin, C., and Thomas, P. C., "Ceres, Vesta, and Pallas: protoplanets, not asteroids," *Eos, Transactions American Geophysical Union*, Vol. 87, No. 10, 2006, pp. 105–109.

[105] Thomas, P., Parker, J. W., McFadden, L., Russell, C. T., Stern, S., Sykes, M., and Young, E., "Differentiation of the asteroid Ceres as revealed by its shape," *Nature*, Vol. 437, No. 7056, 2005, pp. 224–226.

[106] Halliday, A. N. and Kleine, T., "Meteorites and the timing, mechanisms, and conditions of terrestrial planet accretion and early differentiation," *Meteorites and the early solar system II*, Vol. 1, 2006, pp. 775–801.

[107] Lecar, M., Podolak, M., Sasselov, D., and Chiang, E., "On the location of the snow line in a protoplanetary disk," *The Astrophysical Journal*, Vol. 640, No. 2, 2006, pp. 1115.

[108] Chyba, C. F., "Impact delivery and erosion of planetary oceans in the early inner solar system," 1990.

[109] Fu, R. R., Weiss, B. P., Shuster, D. L., Gattacceca, J., Grove, T. L., Suavet, C., Lima, E. A., Li, L., and Kuan, A. T., "An ancient core dynamo in asteroid Vesta," *Science*, Vol. 338, No. 6104, 2012, pp. 238–241.

[110] Bills, B. G., Asmar, S. W., Konopliv, A. S., Park, R. S., and Raymond, C. A., "Harmonic and statistical analyses of the gravity and topography of Vesta," *Icarus*, Vol. 240, 2014, pp. 161–173.

[111] Park, R., Konopliv, A., Asmar, S., Bills, B., Gaskell, R., Raymond, C., Smith, D., Toplis, M., and Zuber, M., "Gravity field expansion in ellipsoidal harmonic and polyhedral internal representations applied to Vesta," *Icarus*, 2013.

[112] McCord, T. B., Adams, J. B., and Johnson, T. V., "Asteroid Vesta: Spectral reflectivity and compositional implications," *Science*, Vol. 168, No. 3938, 1970, pp. 1445–1447.

[113] McCord, T. B., Castillo-Rogez, J., and Rivkin, A., *Ceres: its origin, evolution and structure and Dawn's potential contribution*, Springer, 2012, pp. 63–76.

[114] Rivkin, A. S., Li, J.-Y., Milliken, R. E., Lim, L. F., Lovell, A. J., Schmidt, B. E., McFadden, L. A., and Cohen, B. A., *The surface composition of Ceres*, Springer, 2012, pp. 95–116.

[115] Bland, M. T., "Predicted crater morphologies on Ceres: Probing internal structure and evolution," *Icarus*, Vol. 226, No. 1, 2013, pp. 510–521.

[116] Zolotov, M. Y., "On the composition and differentiation of Ceres," *Icarus*, Vol. 204, No. 1, 2009, pp. 183–193.

[117] Mazarico, E., Rowlands, D. D., Neumann, G. A., Smith, D. E., Torrence, M. H., Lemoine, F. G., and Zuber, M. T., "Orbit Determination of the Lunar Reconnaissance Orbiter," *Journal of Geodesy*, Vol. 86, No. 3, 2012, pp. 193–207.

[118] Miller, J., Konopliv, A., Antreasian, P., Bordi, J., Chesley, S., Helfrich, C., Owen, W., Wang, T., Williams, B., and Yeomans, D., "Determination of Shape, Gravity, and Rotational State of Asteroid 433 Eros," *Icarus*, Vol. 155, No. 1, 2002, pp. 3–17.

[119] Gaskell, R., Barnouin-Jha, O., Scheeres, D., Mukai, T., Hirata, N., Abe, S., Saito, J., Ishiguro, M., Kubota, T., Hashimoto, T., Kawaguchi, J., Yoshikawa, M., Shirakawa, K., and Kominato, T., *Landmark Navigation Studies and Target Characterization in the Hayabusa Encounter with Itokawa*, American Institute of Aeronautics and Astronautics, April 2006.

[120] Tricarico, P. and Sykes, M. V., "The dynamical environment of Dawn at Vesta," *Planetary and Space Science*, Vol. 58, No. 12, 2010, pp. 1516–1525.

[121] Delsate, N., "Analytical and numerical study of the ground-track resonances of Dawn orbiting Vesta," *Planetary and Space Science*, Vol. 59, No. 13, 2011, pp. 1372–1383.

[122] Brophy, J. R., Marcucci, M. G., Ganapathi, G. B., Garner, C. E., Henry, M. D., Nakazono, B., and Noon, D., "The ion propulsion system for Dawn," *AIAA Paper*, Vol. 4542, 2003.

[123] Kaula, W. M., "Theory of satellite geodesy," 1966.

[124] Thomas, P. C., Binzel, R. P., Gaffey, M. J., Zellner, B. H., Storrs, A. D., and Wells, E., "Vesta: Spin pole, size, and shape from HST images," *Icarus*, Vol. 128, No. 1, 1997, pp. 88–94.

[125] Kaula, W. M., "The investigation of the gravitational fields of the moon and planets with artificial satellites," *Advan. Space Sci. Technol*, Vol. 5, 1963, pp. 210–226.

[126] Schenk, P., O'Brien, D. P., Marchi, S., Gaskell, R., Preusker, F., Roatsch, T., Jaumann, R., Buczkowski, D., McCord, T., and McSween, H. Y., "The geologically recent giant impact basins at Vesta's south pole," *Science*, Vol. 336, No. 6082, 2012, pp. 694–697.

[127] Raymond, C., Park, R., Asmar, S., Konopliv, A., Buczkowski, D., De Sanctis, M., McSween, H., Russell, C., Jaumann, R., and Preusker, F., "Vestalia Terra: An ancient mascon in the southern hemisphere of Vesta," Vol. 44, 2013, p. 2882.